Locomotory control algorithms and their neuronal implementation in *Drosophila melanogaster*

Thesis by
Emily Hope Palmer

In Partial Fulfillment of the Requirements for the
Degree of
Doctor of Philosophy

CALIFORNIA INSTITUTE OF TECHNOLOGY
Pasadena, California

2023
Defended April 6, 2023

Emily Hope Palmer
ORCID: 0009-0006-8370-4709

ACKNOWLEDGEMENTS

I am deeply grateful to the array of mentors, collaborators, and friends who have made this work possible. First, I would like to thank my formal mentors and teachers, starting with my advisor, Michael Dickinson, whose guidance and encyclopedic knowledge were critical at every stage of my time at Caltech. I would also like to thank my committee members, Richard Murray, John Dabiri, and Morteza Gharib, for their time and thoughtful feedback over the years.

I have been incredibly fortunate to benefit from the culture of mentorship so established in the Dickinson lab, which has afforded me a number of wonderful informal mentors. To Román Corfas and Jaison Omoto, thank you both for sharing your rich and deep scientific insights, which have formed my own perspective as a researcher, and for supporting and guiding me as I learned to navigate life in the lab and at Caltech generally. To my many other mentors and friends in the lab, especially Tarun Sharma, Amir Behbahani, and Ivo Ros, thank you for your wisdom and patience through many hours spent discussing and troubleshooting. And to the rest of the Dickinson lab, I have been very lucky to have had the opportunity to work with you, learn from you, and spend many hours at Red Door and Ginger with you—you have made my time at Caltech both productive and enjoyable.

To my friends, in and out of the Dickinson lab, and family, thank you for your seemingly limitless support. To my sister, Lindsey—I've said it before and I'll say it again, you're the best sister in the world and I don't deserve you. I am so lucky to have been so near you during my time at Caltech, and the worst part of graduating is moving away from you. To my partner and, now, fiancé, Peter, the best part of graduating is that I get to do it with you.

And finally, thank you to my dogs, Margot and Charles, the real heroes of this work. Coming home every day to you two (and Peter) has been the greatest joy I have ever known, and I can't wait for our next adventure.

ABSTRACT

Scientists and engineers alike have long looked to animals in their pursuit of understanding the natural world and how best to interact with it. While researchers have looked across diverse classes, insects have been extensively studied for their rich diversity of life histories and abilities to perform at spatial and temporal scales difficult for engineered systems. Within insects, the fruit fly, *Drosophila melanogaster*, is a particularly well-studied organism because of its experimental tractability and status as a genetic model organism, providing both detailed descriptions of a broad suite of behaviors and access to and control over specific sets of tissue. In this work, we make use of these tools to study two behaviors in *Drosophila*, local search, the behavior in which walking flies will search the area around a food site in search of other food sources nearby, and the optomotor response, wherein they will stabilize in response to visual motion during flight. In these studies, we will use modern techniques from both biology and engineering, to exhaustively characterize and describe the observed behaviors and attempt to untangle the underlying algorithms and their neuronal implementation.

First, we explore the algorithmic structure of local search in fruit flies. When flies encounter a piece of food, they will often perform walking searches nearby; as food tends to be patchy in natural settings, searches may allow flies to locate other food sites in the area. We induce local search using optogenetic stimulation of sugar-sensing neurons and constrain the flies to a dark, annular arena. These experimental details result in a simplified behavior, as the fly has access to a limited sensory environment, so that the search can be interpreted as an example of idiothetic path integration, and the search itself is one-dimensionalized and therefore more easily analyzed. Our experiments, in tandem with complementary modeling using a state transition diagram formalization of the behaviors, generate two principle findings. First, flies can integrate their location in two dimensions—after the optogenetic activation is disabled and the flies can no longer receive the food stimulus, they will continue to search over the former food site even after completing a full revolution of the annular arena. Second, when multiple food sites are present, they search over a center of the food sites, rather than over one distinct food site. These results both provide insights into the algorithmic structure of local search and an experimental and descriptive paradigm for further inquiries into the behavior.

Second, we investigate the role of a population of neurons, the DNg02s, in the optomotor response. In response to visual patterns of wide-field motion, such that the entire world is moving in the fly-centric reference frame, the animal will attempt to steer to cancel the visual motion, as the most parsimonious explanation of the motion is that the fly itself is moving in the global reference frame. We demonstrate that the DNg02 neurons are a required component in the neural circuitry underlying the optomotor response, but that they are insufficient to induce steering behaviors. We conclude with a set of models that fully recapitulate the collected dataset. With current techniques, distinguishing between the two possible models of the downstream connectivity from the DNg02s to the motor neurons associated with wing motor output is not possible. However, as new datasets become available, particularly complete connectomes of the *Drosophila* nervous system, the neuronal pathways from the DNg02s to the motor systems may be elucidated.

PUBLISHED CONTENT AND CONTRIBUTIONS

[1] Amir H. Behbahani*, Emily H. Palmer*, Román A. Corfas, and Michael H. Dickinson. *Drosophila* re-zero their path integrator at the center of a fictive food patch. *Current Biology*, 31(20), 2021. doi: https://doi.org/10.1016/j.cub.2021.08.006.

*These authors contributed equally.

A.H.B. conducted all experiments under the supervision of M.H.D. E.H.P. developed the state-based models of behavior. A.H.B., E.H.P., and R.A.C. analyzed data and prepared all figures. A.H.B., E. H. P., R.A.C., and M.H.D. wrote the paper.

[2] Emily H. Palmer, Jaison J. Omoto, and Michael H. Dickinson. The role of a population of descending neurons in the optomotor response in flying *Drosophila*. *bioRxiv*, 2022. doi: https://doi.org/10.1101/2022.12.05.519224.

E.H.P. and J.J.O performed all experiments under the supervision of M.H.D. E.H.P. developed the computational models. E.H.P. and J.J.O. analyzed data and prepared all figures. E.H.P., J.J.O., and M.H.D. wrote the paper.

TABLE OF CONTENTS

LIST OF ILLUSTRATIONS

LIST OF TABLES

Chapter 1

INTRODUCTION

For centuries, if not millennia, engineers and scientists alike have turned to animals in the hopes of advancing our understanding of the laws and mechanisms governing our world and of applying that understanding to better interact with and manipulate the world. This keen and sustaining passion has been shared by generations of researchers across diverse fields, from the biohybrid robotics in development today [33, 37], to the development of Velcro in the 1950s based on burrs clinging to a dog's fur [52], to Leonardo da Vinci's observations of bird flight while designing his ornithopter in the fifteenth century [18, 46]. And even further back, we can turn to legend to find examples of early efforts to take inspiration from biology for engineered locomotion, with Icarus and Daedalus constructing wings from feathers and beeswax before taking flight in the ancient Greek myth [8].

Today, many researchers from diverse disciplines continue in this tradition to great effect. While there has been exciting and novel work across plants and animals, vertebrates and invertebrates, in the present work we focus on insects, and particularly on the fruit fly, *Drosophila melanogaster*. Insects generally and the fruit fly in particular offer unique set of opportunities and challenges, distinct from other classes. Insects operate at a spatial and temporal scales difficult for engineered systems; whereas microdrones like the DelFly Micro, with a mass of $O(0.1\,\mathrm{g})$, can only sustain flights for tens of seconds [17], migratory insects like the globe skimmer dragonfly (*Pantala flavescens*, mass $O(0.1\,\mathrm{g})$) have been demonstrated to fly 150–400 km over the sea [13], with energetic models suggesting they may have the capacity stay aloft for 230–286 hours [21]. Furthermore, among animals with centralized nervous systems (i.e., arthropods, cephalopods, and vertebrates), insects have relatively small brains; whereas the human brain consists of around 100 billion neurons, the fruit fly brain is composed of only around 100,000 neurons. This is a distinct advantage in studying the control systems underlying animal behavior, as identification of relevant neurons is commensurately easier in insect species. Finally, insects represent one of the most successful taxonomic classes in terms of the enormous diversity of life histories observed, with over half of all identified eukaryotic species classified as insects [50].

Among insects, the fruit fly is a convenient model organism in a diverse suite of scholarly pursuits, both for its status as genetic model organism and its experimental tractability, and also for the rich array of behaviors it exhibits. As a genetic model organism, we are afforded extensive access to and control over tissue, as described below in Genetic tools in *Drosophila*. These tools, developed for the study of developmental and cellular biology, now enable research into biomechanics and neurobiology. *Drosophila* are also well-adapted for behavioral studies in the lab; they fly well while tethered and require only small spaces for behavioral experiments, and as crepuscular animals, they are adapted for the relatively low-light conditions of laboratories.

Neuroscientist and physiologist David Marr's Tri-level hypothesis provides a convenient scaffold for the studies presented in this work, positing that three complementary levels of analysis enable understanding of information processing systems [35, 44]

- Computational level: What does the system do? Why does it do these things? (In this work, what behaviors are the fly performing? Why does it perform those behaviors?)
- Algorithmic level: How does the system do what it does? (Here, what are the algorithms underlying the fly's behaviors?)
- Implementation or physical level: How are the algorithms physically realized? (What are the neuronal circuits or biomechanical structures underlying the algorithms?)

In this thesis, we describe the algorithmic basis of locomotory behaviors in *Drosophila* and efforts to elucidate the neural implementation of those algorithms—the algorithmic and implementation levels. Our efforts to untangle the algorithms and implementations underlying behaviors are again aided by our choice in experimental organism; decades of psychophysics experiments provide clear descriptions of the behaviors we will focus on in the present work and, at least with respect to flight behaviors in Chapters III and IV, the algorithms underlying these behaviors. We endeavor to marry modern techniques from both neuroscience and engineering in our attempt to elucidate the algorithms and neuronal pathways underlying our behaviors of interest. To that end, in this chapter I will briefly discuss the genetic tools and an overview of the sensory systems that are relevant to the studies described in this thesis and therefore necessary background for the further chapters. Descriptions of

the relevant motor systems and the tools we draw from control theory and aerodynamics to formally describe *Drosophila* behavior and flight follow in Chapters II, III, and IV as necessary. I will conclude this chapter with a summary of the work presented in this thesis.

1.1 Genetic toolkit in *Drosophila*

The ability to introduce engineered segments of DNA to the *Drosophila* genome has made fruit flies one of the most powerful model organisms in use today through the ability to express genes of interest in the experimental animals [11]. Multiple targeted gene expression systems enable the separation of gene expression into two complementary problems: first, which genes to express, and second, in what tissue to express those genes [12]. This separation allows experimenters to take particular effects in particular sets of tissue with great specificity and versatility, as any of an array of effects can be taken in diverse sets of any tissue. In this section, I will focus on the GAL4/upstream activating sequence (UAS) system, though there are multiple targeted gene expression systems available in *Drosophila* that may be used in tandem.

In the GAL4/UAS system, a transgenetic animal will be engineered through biochemical processes with either the GAL4 gene under the control of a driver gene or a reporter gene under the control of the UAS gene [12]. The driver gene only is active in certain tissue (e.g., only in the muscles, only in certain neurons, etc.); when it is active, the GAL4 gene is expressed, leading to the generation of the Gal4 protein. In turn, the Gal4 protein binds to the UAS region and induces the expression of the reporter gene, which specifies some effect [12, 16]. Geneticists have created vast libraries of transgenetic variants on wild-type flies (i.e., flies you may find in nature, without engineered genetic material) with either the driver gene-GAL4 gene pair (GAL4 lines, Figure 1.1A) or UAS gene-reporter gene pair (UAS lines, Figure 1.1B). By mating animals from a GAL4 line to animals from a UAS line, the offspring will have both pairs, and the effect specified by the reporter will take place in the tissue specified by the driver (Figure 1.1C).

In this work, we will primarily make use of three general classes of effectors enabling experimental access to or control over neurons of interest: neuronal activation (exciting the neurons), silencing (inhibiting neuronal function), or functional imaging (indirectly imaging neuronal activity). These tools have many uses and can provide complementary insights into neuronal function; in Chapters III and IV, for example, we use silencing as a test for necessity (whether the neurons necessary for a given

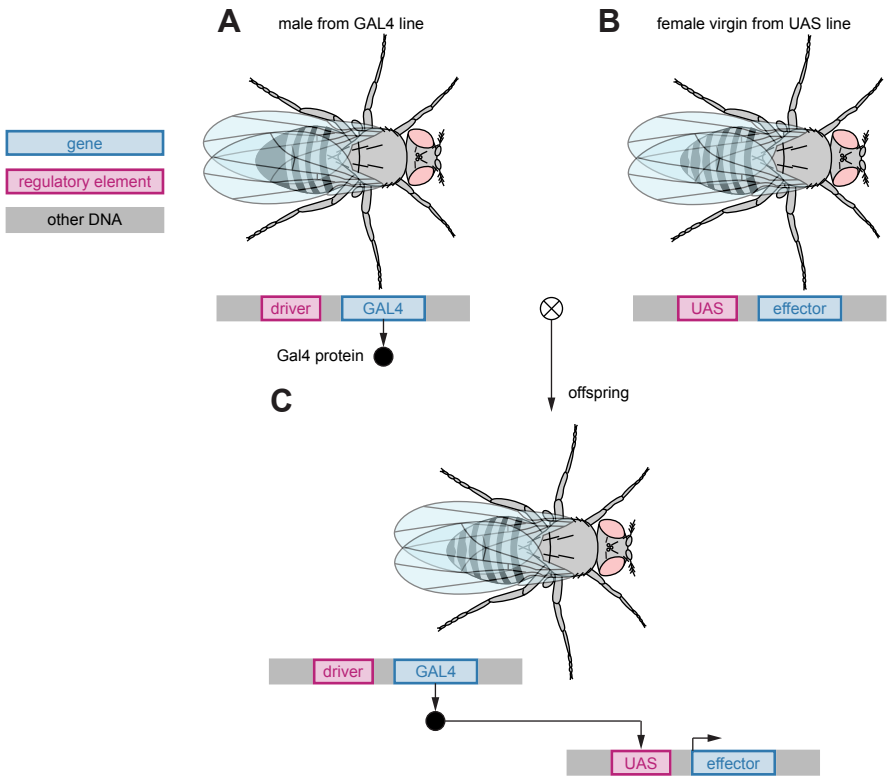

Figure 1.1: GAL4/UAS system enables expression of genes in tissue of interest.
(A) Male parental fly from GAL4 line has GAL4 gene under the control of a driver gene. The GAL4 gene is only expressed in tissue specified by the driver, such that the Gal4 protein is only generated in that tissue.
(B) Female virgin parental fly from UAS line has some effector gene under the control of a UAS gene. The UAS gene is expressed only when the Gal4 protein is present; in this fly, no Gal4 proteins exist, so the effector gene is not expressed.
(C) Offspring fly from mating flies from (A) and (B). In this fly, the Gal4 protein is generated in tissue specified by the driver gene. In that tissue, the Gal4 protein binds to the UAS gene, leading to the expression of the effector gene. Thus, in the tissue specified by the driver gene, the effect specified by the effector gene takes place.

behavior) and activation as a test for sufficiency (whether the neurons alone are able to induce the behavior). Here, I will briefly summarize these three classes and the basics of their operation.

Optogenetic activation

Since their introduction in the late nineties, optogenetic techniques have become one of the critical tools available to systems neuroscientists for the manipulation of neuronal activity [38]. Broadly, optogenetic techniques enable control over neurons through the expression of light-sensitive proteins. Channelrhodopsins are a ubiquitous and diverse class of light-gated ion channels, which can respond to various wavelengths of light to either inhibit or excite the neurons in which they are expressed [10, 32, 39]. These channels occur naturally in algal cells which are able to move to find areas with suitable light levels; they enable the light-sensitivity which

is critical for this navigational behavior [32]. We make particular use of the light-sensitive channel CsChrimson, a variant on the general class of channelrhodopsins. When the channel CsChrimson is excited by light, the channel opens, leading to a depolarization of the membrane and excitation of the neuron.

Neuronal inhibition

Multiple genetic tools exist for neuronal inhibition, including the optogenetic techniques noted previously. We make particular use of the inwardly rectifying potassium channel Kir2.1, expression of which chronically hyperpolarizes cells and thereby reduces the probability of the neuron firing action potentials or releasing neurotransmitter both spontaneously and in response to neuronal input [3, 26]. This mechanism is distinct from genes that promote cell death (e.g., *reaper*, *grim*; [7, 57]) as the cells remain alive. As opposed to mechanisms utilizing cell death, techniques which enable chronic hyperpolarization can sometimes have less intense effects on the health of the animal as all neurons are still alive. However, with sufficiently strong neuronal input, action potentials may still be fired and neurotransmitter may still be released, so neuronal silencing can sometimes elicit a weaker behavioral effect than complete neuronal ablation. Chronic silencing is also distinct from the optogenetic tools mentioned previously or similar thermogenetic tools (which makes use of thermosensitive channels [6, 29]), as these channels are activated with temporal specificity.

Functional imaging

When neurons fire action potentials, calcium ions enter the cells; calcium sensors therefore act as convenient proxies for neuronal activity. These sensors often come in one of two forms: genetically encoded calcium indicators (GECIs) and calcium sensitive dyes. Of the two, we focus on GECIs, as they are chronic (i.e., always present in the cells) and noninvasive [2]. In particular, we make use of GCaMP, a GECI commonly used in *Drosophila*, not only for imaging neuronal activity, but also activity in the muscles (which is also associated with increased calcium levels). There are multiple variants of GCaMP sensors, and new variants continue to be developed by researchers, in the hopes of improving the sensitivity and temporal dynamics of the sensors (e.g., [2, 23, 54]). In this work, we use both GCaMP7 and GCaMP8; a discussion of the relative performances can be found in Chapter 3.

I will briefly describe the biophysical mechanisms underlying the operation of GCaMP imaging, with a schematic representation shown in Figure 1.2. When a

neuron becomes active, the membrane potential increases and voltage-gated calcium ions open, at which point Ca^{2+} ions flood into the cell. The GCaMP protein can bind to the Ca^{2+} ions; when bound, it undergoes a conformal change [1]. In the bound state, the protein may be excited by 480 nm photons; when the molecule returns to the ground state from the excited state, it emits a 510 nm photon [4]. Thus, if we excite a neuron with GCaMP proteins at 480 nm and image at 510 nm photons, we are able to record the level of Ca^{2+}-saturated GCaMP proteins in the cell, which is itself a proxy for cellular activity.

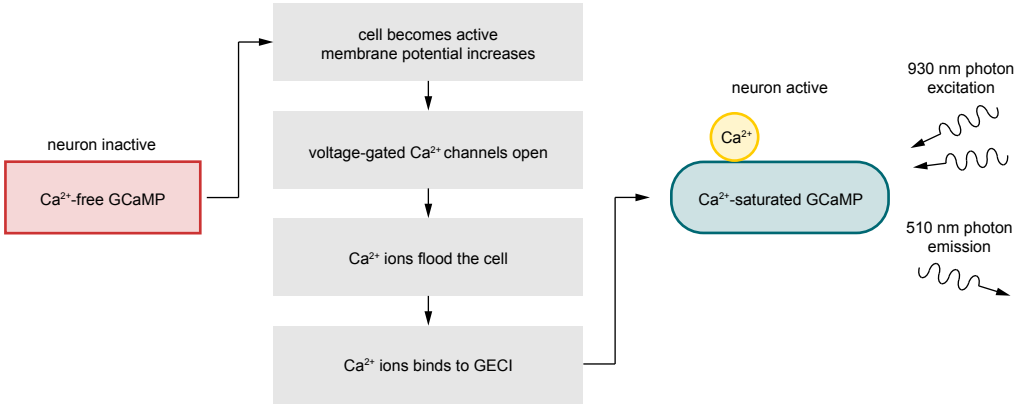

Figure 1.2: Genetically encoded calcium indicators enable imaging neuronal activity. Two-photon excitation shown, though one-photon excitation at a shorter wavelength is also possible. Unbound GCaMP protein is showed by red rectangle. After binding to a calcium ion (indicated by yellow circle), GCaMP protein undergoes a conformal change (teal rounded rectangle).

Excitation with a single 480 nm photon is referred to as one-photon functional imaging; in Chapter 3, we make use of two-photon functional imaging, a variation in which we excite with two 930 nm photons arriving simultaneously at the tissue sample. Two-photon imaging has a number of advantages over one-photon imaging. First, excitation with a longer wavelength allows us to penetrate deeper into the brain with minimal scattering of the light, so we are able to image cells that may otherwise be inaccessible due to prohibitive scattering or dissection [53]. Second, two-photon imaging enables excitation in a thinner plane than one-photon imaging and we are therefore afforded better spatial resolution [53]. However, two-photon imaging is also associated with a number of technical limitations, the most significant of which is the requirement that two exciting photons arrive at the GCaMP protein simultaneously; we therefore use a femtosecond pulsed laser for the functional imaging experiments in this work.

1.2 Sensing self-motion: Sensorimotor pathways in walking and flight

Fruit flies, like most motile animals and engineered systems, integrate wide array of sensory input to control their locomotory behaviors. Sensory structures across an insects body collect rich information about the environment—the insect antennae alone contain diverse sensory neurons that have been shown to be responsive to wind, gravity, sound, chemicals, temperature, and humidity [47]. Anatomical and behavioral experimentation have provided insights into the organization of sensorimotor processing in the *Drosophila* nervous system. Sensory information, collected by the antenna and other sensory structures including the eyes and a diverse array of mechanosensors, is passed to the brain and ventral nerve cord (VNC), a structure located in the thorax which is the rough equivalent of the spinal cord in humans (Figure 1.3). The brain and VNC pass information to each other through the neck connective via descending neurons (DNs, brain to VNC) and ascending neurons (ANs, VNC to brain). The brain and the VNC then send commands to motor systems via motor neurons.

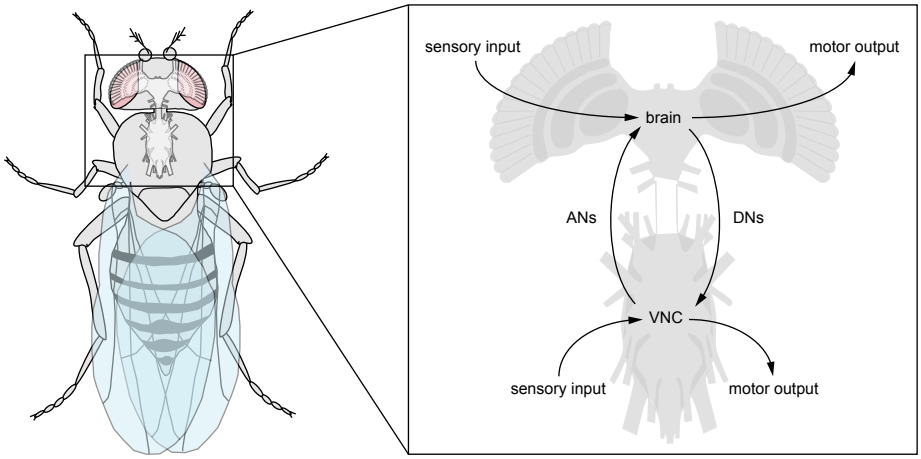

Figure 1.3: Organization of *Drosophila* nervous system. Brain and VNC collect and process sensory information. Ascending neurons transmit information from VNC to brain; descending neurons transmit information from brain to VNC. Brain and VNC send commands to motor neurons.

It is often convenient to attempt to limit an experimental animal's access to sensory stimuli to specific sensory modalities; for example, in Chapter II we perform our walking experiments in the dark, such that the flies did not have access to visual stimuli, and in Chapters III and IV we perform our flight experiments with tethered animals, such that they did not receive angular velocity stimuli from body rotations to the halteres or external flow stimuli to the antenna. In this section, I will provide brief overviews of the sensory stimuli most relevant to the work presented in this dissertation. The motor systems are discussed at some length in later chapters.

Proprioception

Proprioception refers to the ability to sense one's own body position and movement. Under classical definitions, mechanosensory proprioceptive neurons tend to be localized in muscles, joints, and tendons, and can be divided in insects and mammals into three populations [55]. Here, we briefly describe the proprioceptors found in insects, but analogs for each have been described in mammals as well.

- Position and velocity encoders: a class of stretch receptors known as chordotonal organs have been found in different biomechanical structures in insects, including the legs, wings, halteres, and antennae [15, 27]. Chordotonal organs in the legs have been shown to respond to the position and relative velocity of different leg segments. However, not all chordotonal organs are proprioceptive; the Johnston's organ in the *Drosophila* antenna, for example, has been shown to have different populations of sensory neurons responsive to the sensation of sound, wind, and gravity [27].

- Strain sensors: campaniform sensilla, small dome-like structures, are sensitive to strains in the cuticle and tend to be clustered near joints [45, 56]. Campaniform sensilla tend to respond only when motion is resisted—when a joint is moved passively or is at rest, the campaniform sensilla may be silent [56].

- Threshold detectors: tightly-packed arrays of sensory hairs known as hair plates are positioned in the cuticle such that they are deflected when a joint is in a particular position [45, 56]. The position tends to be at the extremes of the joint's range, suggesting that they function as limit detectors. Alternatively, they have been proposed to act to anticipate changes in locomotory phase; for example, in walking, hair plates may provide the feedback to transition between the swing and stance phase of the gait [55].

Proprioceptors project to the central nervous system, and particularly the VNC in the case of leg and wing proprioceptors [55]. A critical function of proprioception is to ensure stability, though this sensory feedback is likely also relevant to more complex movement sequences; for example, proprioception has been hypothesized as one mechanism for navigation in visually featureless environments [55]. Proprioceptive feedback has also been shown to alter responses to visual stimuli during flight [5].

Visual processing

Fruit flies sense light stimuli through two primary structures, the compound eyes and the ocelli, a set of three simple eyes located on the dorsal-most part of the head. In many behaviors, the functions of these two structures have not been disambiguated, though the anatomy provides some helpful clues. Axons of the interneurons from the ocelli (L-neurons) have notably large diameters and therefore transmit information more quickly than neurons with smaller diameters [30, 42, 43]. These interneurons project to the posterior slope in the brain, where they synapse directly onto descending neurons transmitting information to the VNC [42, 51]. These descending neurons then connect to motor systems associated with wing, head, and leg motor control. Together, these anatomical hints indicate that the ocelli are likely involved in quick stabilization reflexes [30]. This anatomical evidence is complemented by behavioral experiments demonstrating the involvement of the ocelli in simple behavioral responses like the dorsal light response, wherein flies align their heads to bright lights [48], as well as more functions; the ocelli of locusts, for example, have been reported to act as high-pass temporal and low-pass spatial filters, implying they would be sensitive to the sudden movements of the entire visual world that occur when the animal experiences flight instabilities [58].

The compound eyes are comparatively complex structures, with each compound eye consisting of around 700 ommatidia, the structures in which photoreceptors in the eyes are localized [22]. The photoreceptors project to lamina cells, which in turn provide input to the T4 and T5 neurons, the first cells in the visual processing pathway to display directional sensitivity [19, 25]. T4 and T5 cells respond to increments and decrements in light intensity, respectively, in a preferred direction [34]. For example, a given T4 cell may only respond to increments in light intensity from left to right, right to left, up to down, or down to up. The eight kinds of T4 and T5 neurons (one T4 and one T4 neurons representing each of the four preferred directions) tile all visual space. The T4 and T5 cells provide input to a wide array of visual neurons, including neurons which process the visual features of individual objects and, most relevant to the work presented in Chapters III and IV, the lobula plate tangential cells (LPTCs), which process self-motion [49].

The LPTCs are sensitive to patterns of wide-field motion, the visual stimulus an animal experiences as it moves and perceives the relative motion of the world around it [20]. Early efforts identified two classes of LPTCs, the vertical system (VS) and horizontal system (HS) cells, though many more classes have since been identified. The HS and VS cells were initially named for the characteristic orientations of their

dendritic arbors in the lobula plate; the dendrites of VS cells run vertically across the lobula plate and the dendrites of the HS cells run horizontally [20, 24]. These names remained apt as further experiments indicated that the VS cells are responsive to patterns of vertical optic flow and HS cells to patterns of horizontal optic flow [20, 31]. Indeed, it is precisely the orientation of their arbors that enable the HS and VS cells to respond to their preferred patterns of optic flow; their response is the integration of spatially localized information from T4 and T5 cells along a particular axis in the retinotopically organized lobula plate [36]. The LPTCs project to a number of regions in the central brain, including the posterior slope. As with the L-neurons, the LPTCs likely provide input to descending neurons in the posterior slope which send outputs to motor centers in the VNC [40].

Efference copy

Whereas proprioceptive and visual feedback arises when sensory neurons sense the movement or position of the body, efference copy refers to an internally generated signal produced by motor commands. Efference copy allows the animal's nervous system to construct an estimate of the effects of its own actions and thereby distinguish between sensory stimuli generated from self-motion and that generated by the environment [9]. For example, the input to the fly's visual system from the photoreceptors is a composite of the motion of objects in the world (e.g., predators, conspecifics, etc.), voluntary or evoked self-motion (i.e., motion generated by the animal's behavioral output), and involuntary motion (e.g., during flight, motion induced by an unexpected gust). Efference copy can provide an estimate for the likely voluntary or evoked self-motion, since this is the motion generated by the animal's motor systems [14, 28]. By subtracting the efference copy signal from the visual input, an animal can determine the motion of objects in the world and any involuntary self-motion (Figure 1.4).

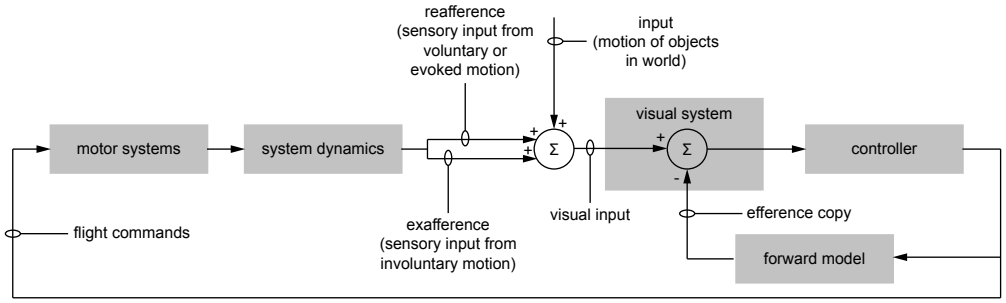

Figure 1.4: Efference copy in the *Drosophila* visual system. The visual input to the visual system is a composite of the motion of objects in the world, voluntary and evoked self-motion (reafference), and involuntary self-motion (exafference). Efference copy can suppress reafferent signals.

Research has provided evidence for efference copy in the *Drosophila* visual system during flight. For example, visual neurons receive motor-related input during quick voluntary turns (saccades) which are similar in magnitude but opposite in sign to the expected reafferent visual input [28]. As the efference copy signal is similar in magnitude but opposite in sign, it acts to suppress the visual input induced by this voluntary turn. This suppression allows the fly to perform voluntary turns without evoking a stabilizing response; without suppression, a reflex known as the optomotor response (discussed in depth in Chapters III and IV) would cause the fly to attempt to turn in the opposite direction as the voluntary turn to stabilize their flight trajectory.

1.3 Summary of work

In this dissertation, I will present results from two projects combining psychophysics experimentation in *Drosophila melanogaster* and behavioral modeling.

Algorithmic models of path integration

Chapter II details our investigation into the algorithms governing local search in fruit flies, the behavior in which, upon encountering a patch of food, the animal will make short excursions away from the food site in search of other nearby food patches. Flies perform this behavior in the absence of external sensory cues by which they may navigate (e.g., flies will perform the search in the dark, and therefore without visual cues), indicating that they are using idiothetic (i.e., self motion) cues to navigate. In this chapter, we induced local search in flies confined to an annular arena and compared the resulting behavior to a set of computational models. The behavioral experiments were performed with optogenetic activation of sugar receptors, such that we were able to control the timing and location of the food stimuli. The experiments indicated that *Drosophila melanogaster* are able to integrate in two-dimensions—in our constrained, annular arena, flies were able to continue searching over a former food site even after fully circling the arena. We further tested the algorithms underlying local search, specifically when more than one food sites are present, by constructing predictive models. The first model posited that flies search around a specific food site, and that even when multiple food locations have been discovered, they will continue to center their search over one specific food site. Alternatively, the second model hypothesized that when multiple food sites are present, flies will search over the center of the patch. There are multiple potential mechanisms for computing the central location; we use a simple

center-of-mass model, where the central location is simply the average of all known locations. Alternative computations could involve temporal decay, with food zones more recently encountered more heavily weighted in calculating the center location. Regardless, our models generated testable predictions with respect to how real flies would behave when multiple food sites have been encountered. By testing these distinguishable hypotheses, we showed that flies appear to center their searches over a central location, rather than one distinct food site.

Descending neuronal pathways mediating steady-state flight control

In Chapters III and IV, I present our efforts to elucidate some of the neuronal pathways involved in flight stabilization in *Drosophila*. We focus on the optomotor response, a well-characterized behavior in which animals will attempt to steer to compensate for patterns of wide-field optic flow—patterns of visual motion where the entire world appears to be moving around the animal. The yaw optomotor response is robust in fruit flies and easily quantifiable with a single camera imaging the wings during tethered flight; in response to yaw optic flow to the right in front of the fly, for example, the most parsimonious explanation is that the fly itself is turning to the left, and so it will attempt to steer to the right to compensate by increasing the wingbeat amplitude of the left wing and decreasing that of the right wing. Recent work from Namiki and colleagues [41] identified a population of descending neurons (DNs) that appear to be involved in visually-mediated flight behaviors. DNs, which convey information from the brain to the ventral nerve cord (VNC) through the neck connective, represent an informational bottleneck (since the brain has on the order of 100,000 neurons, the VNC 15,000, and the DNs only around 400), and therefore offer an opportunity to gain purchase over the neuronal mechanisms underlying flight control. In their recent paper, Namiki and colleagues demonstrated that optogenetic activation of these neurons, the DNg02s, resulted in increases in wingbeat amplitude, and showed through anatomical investigation that they receive input in the brain in regions associated with visual processing, including the posterior slope [41].

In Chapter III, we show that the DNg02 neurons are a required pathway for the optomotor response; when DNg02 neurons are silenced, the magnitude of the optomotor response is diminished in proportion to the number of cells silenced. Using two-photon functional imaging, we then thoroughly characterize the neuronal responses to a wide-array of visual stimuli, with these result indicating that morphological variation within the population does not appear to correlate with functional vari-

ation with respect to the tested visual stimuli, and that DNg02 activity is more closely related to motor output than to visual input. In particular, we observed strong correlations between DNg02 activity and contralateral wingbeat amplitude, and asymmetries in DNg02 activity across the midline (i.e., DNg02 activity often increased on one side of the body and decreased on the other).

We continue our investigation in Chapter IV by specifically probing the downstream effects of the DNg02s on the motor system. The previously reported activation results [41] indicated that these cells likely provide input to the power muscles, the set of flight muscles generating the power necessary to beat the wing back and forth during flight. We probe this hypothesis by estimating the changes in power production that result from silencing DNg02 neurons and by unilaterally activating DNg02 neurons. Unilateral activation resulted in bilaterally symmetric motor responses. In contrast to the functional imaging results, which indicated correlations between DNg02 activity and contralateral wingbeat amplitude, these results implied that the DNg02 neurons had symmetric effects on the motor system. Furthermore, the results suggested that other neuronal pathways were involved in the optomotor response, since unilateral DNg02 activation was insufficient to generate turning behaviors. We conclude by proposing two distinct hypotheses with respect to the symmetry of the DNg02 connectivity to the motor system, both of which can fully recapitulate the observed dataset. While distinguishing between these models is infeasible with current experimental methods, future work may reveal the connectivity structure downstream of the DNg02 neurons as new neuroscientific tools become available.

Bibliography

[1] Jasper Akerboom, Jonathan D. Vélez Rivera, María M. Rodríguez Guilbe, Elisa C. Alfaro Malavé, Hector H. Hernandez, Lin Tian, S. Andrew Hires, Jonathan S. Marvin, Loren L. Looger, and Eric R. Schreiter. Crystal structures of the gcamp calcium sensor reveal the mechanism of fluorescence signal change and aid rational design. *Journal of Biological Chemistry*, 284(10): 6455–6464, 2009.

[2] Jasper Akerboom, Tsai-Wen Chen, Trevor J. Wardill, Lin Tian, Jonathan S. Marvin, Sevinç Mutlu, Nicole Carreras Calderón, Federico Esposti, Bart G. Borghuis, Xiaonan Richard Sun, et al. Optimization of a gcamp calcium indicator for neural activity imaging. *Journal of Neuroscience*, 32(40):13819–13840, 2012.

[3] Richard A. Baines, Jay P. Uhler, Annemarie Thompson, Sean T. Sweeney, and Michael Bate. Altered electrical properties in drosophilaneurons developing without synaptic transmission. *Journal of Neuroscience*, 21(5):1523–1531, 2001.

[4] Lauren M. Barnett, Thomas E. Hughes, and Mikhail Drobizhev. Deciphering the molecular mechanism responsible for gcamp6m's ca2+-dependent change in fluorescence. *PloS One*, 12(2):e0170934, 2017.

[5] Jan Bartussek and Fritz-Olaf Lehmann. Proprioceptive feedback determines visuomotor gain in Drosophila. *Royal Society Open Science*, 3(1):150562, 2016.

[6] Jacob G. Bernstein, Paul A. Garrity, and Edward S. Boyden. Optogenetics and thermogenetics: technologies for controlling the activity of targeted cells within intact neural circuits. *Current Opinion in Neurobiology*, 22(1):61–71, 2012.

[7] Po Chen, William Nordstrom, Bridget Gish, and John M. Abrams. Grim, a novel cell death gene in Drosophila. *Genes & Development*, 10(14):1773–1782, 1996.

[8] Simon Cookson. An Important Failure: Lessons from Daedalus and Icarus. In *Advances in Human Aspects of Transportation: Proceedings of the AHFE 2016 International Conference on Human Factors in Transportation, July 27-31, 2016, Walt Disney World®, Florida, USA*, pages 863–872. Springer, 2017.

[9] Trinity B. Crapse and Marc A. Sommer. Corollary discharge across the animal kingdom. *Nature Reviews Neuroscience*, 9(8):587–600, 2008.

[10] Karl Deisseroth and Peter Hegemann. The form and function of channelrhodopsin. *Science*, 357(6356):eaan5544, 2017.

[11] Alberto del Valle Rodríguez, Dominic Didiano, and Claude Desplan. Power tools for gene expression and clonal analysis in drosophila. *Nature Methods*, 9 (1):47–55, 2012.

[12] Joseph B. Duffy. Gal4 system in Drosophila: A fly geneticist's Swiss army knife. *Genesis*, 34(1-2):1–15, 2002.

[13] Hong-Qiang Feng, Kong-Ming Wu, Yun-Xia Ni, Deng-Fa Cheng, and Yu-Yuan Guo. Nocturnal migration of dragonflies over the Bohai Sea in northern China. *Ecological Entomology*, 31(5):511–520, 2006.

[14] Lisa M. Fenk, Anmo J. Kim, and Gaby Maimon. Suppression of motion vision during course-changing, but not course-stabilizing, navigational turns. *Current Biology*, 31(20):4608–4619, 2021.

[15] Laurence H. Field and Thomas Matheson. Chordotonal organs of insects. In *Advances in insect physiology*, volume 27, pages 1–228. Elsevier, 1998.

[16] Janice A. Fischer, Edward Giniger, Tom Maniatis, and Mark Ptashne. Gal4 activates transcription in Drosophila. *Nature*, 332(6167):853–856, 1988.

[17] Dario Floreano and Robert J. Wood. Science, technology and the future of small autonomous drones. *Nature*, 521(7553):460–466, 2015.

[18] Benjamin J. Goodheart. Tracing the history of the ornithopter: Past, present, and future. *Journal of Aviation/Aerospace Education & Research*, 21(1):31–44, 2011.

[19] Eyal Gruntman, Sandro Romani, and Michael B. Reiser. Simple integration of fast excitation and offset, delayed inhibition computes directional selectivity in drosophila. *Nature Neuroscience*, 21(2):250–257, 2018.

[20] Klaus Hausen. The lobula-complex of the fly: Structure, function and significance in visual behaviour. *Photoreception and Vision in Invertebrates*, pages 523–559, 1984.

[21] Johanna S.U. Hedlund, Hua Lv, Philipp Lehmann, Gao Hu, R. Charles Anderson, and Jason W. Chapman. Unraveling the world's longest non-stop migration: The indian ocean crossing of the globe skimmer dragonfly. *Frontiers in Ecology and Evolution*, 9:525, 2021.

[22] Martin Heisenberg and Reinhard Wolf. *Vision in Drosophila: Genetics of microbehavior*. Springer-Verlag, 1984.

[23] Nordine Helassa, Borbala Podor, Alan Fine, and Katalin Török. Design and mechanistic insight into ultrafast calcium indicators for monitoring intracellular calcium dynamics. *Scientific Reports*, 6(1):1–14, 2016.

[24] R. Hengstenberg, K. Hausen, and B. Hengstenberg. The number and structure of giant vertical cells (VS) in the lobula plate of the blowfly Calliphora erythrocephala. *Journal of Comparative Physiology A*, 149(2):163–177, 1982.

[25] Maximilian Joesch, Bettina Schnell, Shamprasad Varija Raghu, Dierk F Reiff, and Alexander Borst. On and off pathways in drosophila motion vision. *Nature*, 468(7321):300–304, 2010.

[26] David C. Johns, Ruth Marx, Richard E. Mains, Brian O'Rourke, and Eduardo Marbán. Inducible genetic suppression of neuronal excitability. *Journal of Neuroscience*, 19(5):1691–1697, 1999.

[27] Ryan G. Kavlie and Jörg T. Albert. Chordotonal organs. *Current Biology*, 23 (9):R334–R335, 2013.

[28] Anmo J. Kim, Jamie K. Fitzgerald, and Gaby Maimon. Cellular evidence for efference copy in drosophila visuomotor processing. *Nature Neuroscience*, 18 (9):1247–1255, 2015.

[29] Toshihiro Kitamoto. Conditional modification of behavior in drosophila by targeted expression of a temperature-sensitive shibire allele in defined neurons. *Journal of Neurobiology*, 47(2):81–92, 2001.

[30] Holger G. Krapp. Ocelli. *Current Biology*, 19(11):R435–R437, 2009.

[31] Holger G. Krapp, Barbel Hengstenberg, and Roland Hengstenberg. Dendritic structure and receptive-field organization of optic flow processing interneurons in the fly. *Journal of Neurophysiology*, 79(4):1902–1917, 1998.

[32] John Y. Lin. A user's guide to channelrhodopsin variants: Features, limitations and future developments. *Experimental Physiology*, 96(1):19–25, 2011.

[33] Zening Lin, Tao Jiang, and Jianzhong Shang. The emerging technology of biohybrid micro-robots: A review. *Bio-Design and Manufacturing*, pages 1–26, 2022.

[34] Matthew S. Maisak, Juergen Haag, Georg Ammer, Etienne Serbe, Matthias Meier, Aljoscha Leonhardt, Tabea Schilling, Armin Bahl, Gerald M. Rubin, Aljoscha Nern, et al. A directional tuning map of drosophila elementary motion detectors. *Nature*, 500(7461):212–216, 2013.

[35] David Marr. *Vision: A computational investigation into the human representation and processing of visual information*. MIT press, 2010.

[36] Alex S. Mauss, Katarina Pankova, Alexander Arenz, Aljoscha Nern, Gerald M. Rubin, and Alexander Borst. Neural circuit to integrate opposing motions in the visual field. *Cell*, 162(2):351–362, 2015.

[37] Barbara Mazzolai and Cecilia Laschi. A vision for future bioinspired and biohybrid robots. *Science Robotics*, 5(38):eaba6893, 2020.

[38] Gero Miesenböck. The optogenetic catechism. *Science*, 326(5951):395–399, 2009.

[39] Farhan Mohammad, James C. Stewart, Stanislav Ott, Katarina Chlebikova, Jia Yi Chua, Tong-Wey Koh, Joses Ho, and Adam Claridge-Chang. Optogenetic inhibition of behavior with anion channelrhodopsins. *Nature Methods*, 14(3):271–274, 2017.

[40] Shigehiro Namiki, Michael H. Dickinson, Allan M. Wong, Wyatt Korff, and Gwyneth M. Card. The functional organization of descending sensory-motor pathways in Drosophila. *Elife*, 7:e34272, 2018.

[41] Shigehiro Namiki, Ivo G. Ros, Carmen Morrow, William J. Rowell, Gwyneth M. Card, Wyatt Korff, and Michael H. Dickinson. A population of descending neurons that regulates the flight motor of Drosophila. *Current Biology*, 32(5):1189–1196, 2022.

[42] Dick R. Nässel and Mariana Hagberg. Ocellar interneurones in the blowfly calliphora erythrocephala: Morphology and central projections. *Cell and Tissue Research*, 242:417–426, 1985.

[43] Matthew M. Parsons, Holger G. Krapp, and Simon B. Laughlin. Sensor fusion in identified visual interneurons. *Current Biology*, 20(7):624–628, 2010.

[44] David Peebles and Richard P. Cooper. Thirty years after Marr's vision: Levels of analysis in cognitive science, 2015.

[45] J.W.S. Pringle. Proprioception in insects. *Journal of Experimental Biology*, 15:101–103, 1938.

[46] Philip L. Richardson. Leonardo da Vinci's discovery of the dynamic soaring by birds in wind shear. *Notes and Records: the Royal Society Journal of the History of Science*, 73(3):285–301, 2019.

[47] Dietrich Schneider. Insect antennae. *Annual Review of Entomology*, 9(1): 103–122, 1964.

[48] H. Schuppe and Roland Hengstenberg. Optical properties of the ocelli of calliphora erythrocephala and their role in the dorsal light response. *Journal of Comparative Physiology A*, 173:143–149, 1993.

[49] Kazunori Shinomiya, Aljoscha Nern, Ian A. Meinertzhagen, Stephen M. Plaza, and Michael B. Reiser. Neuronal circuits integrating visual motion information in drosophila melanogaster. *Current Biology*, 32(16):3529–3544, 2022.

[50] Nigel E. Stork, James McBroom, Claire Gely, and Andrew J. Hamilton. New approaches narrow global species estimates for beetles, insects, and terrestrial arthropods. *Proceedings of the National Academy of Sciences*, 112(24):7519–7523, 2015.

[51] Nicholas J. Strausfeld and U.K. Bassemir. Lobula plate and ocellar interneurons converge onto a cluster of descending neurons leading to neck and leg motor neuropil in calliphora erythrocephala. *Cell and Tissue Research*, 240:617–640, 1985.

[52] Claire Suddath. A brief history of: Velcro. *Time*, 2010.

[53] Karel Svoboda and Ryohei Yasuda. Principles of two-photon excitation microscopy and its applications to neuroscience. *Neuron*, 50(6):823–839, 2006.

[54] Lin Tian, S. Andrew Hires, Tianyi Mao, Daniel Huber, M. Eugenia Chiappe, Sreekanth H. Chalasani, Leopoldo Petreanu, Jasper Akerboom, Sean A. McKinney, Eric R. Schreiter, et al. Imaging neural activity in worms, flies and mice with improved gcamp calcium indicators. *Nature Methods*, 6(12):875–881, 2009.

[55] John C. Tuthill and Eiman Azim. Proprioception. *Current Biology*, 28(5): R194–R203, 2018.

[56] John C. Tuthill and Rachel I. Wilson. Mechanosensation and adaptive motor control in insects. *Current Biology*, 26(20):R1022–R1038, 2016.

[57] Kristin White, Megan E. Grether, John M. Abrams, Lynn Young, Kim Farrell, and Hermann Steller. Genetic control of programmed cell death in Drosophila. *Science*, 264(5159):677–683, 1994.

[58] Martin Wilson. The functional organisation of locust ocelli. *Journal of Comparative Physiology*, 124:297–316, 1978.

Chapter 2

DROSOPHILA RE-ZERO THEIR PATH INTEGRATOR AT THE CENTER OF A FICTIVE FOOD PATCH

Amir H. Behbahani*, Emily H. Palmer*, Román Corfas, and Michael H. Dickinson. *Drosophila* re-zero their path integrator at the center of a fictive food patch. *Current Biology*, 31(20), 2021. doi: https://doi.org/10.1016/j.cub.2021.08.006.
*These authors contributed equally.
A.H.B. conducted all experiments under the supervision of M.H.D. E.H.P. developed the state-based models of behavior. A.H.B., E.H.P., and R.A.C. analyzed data and prepared all figures. A.H.B., E. H. P., R.A.C., and M.H.D. wrote the paper.

2.1 Abstract

The ability to keep track of one's location in space is a critical behavior for animals navigating to and from a salient location, and its computational basis is now beginning to be unraveled. Here, we tracked flies in a ring-shaped channel as they executed bouts of search triggered by optogenetic activation of sugar receptors. Unlike experiments in open field arenas, which produce highly tortuous search trajectories, our geometrically constrained paradigm enabled us to monitor flies' decisions to move toward or away from the fictive food. Our results suggest that flies use path integration to remember the location of a food site even after it has disappeared, and flies can remember the location of a former food site even after walking around the arena one or more times. To determine the behavioral algorithms underlying *Drosophila* search, we developed multiple state transition models and found that flies likely accomplish path integration by combining odometry and compass navigation to keep track of their position relative to the fictive food. Our results indicate that whereas flies re-zero their path integrator at food when only one feeding site is present, they adjust their path integrator to a central location between sites when experiencing food at two or more locations. Together, this work provides a simple experimental paradigm and theoretical framework to advance investigations of the neural basis of path integration.

2.2 Introduction

For many animals, including humans, the ability to return to a specific location, such as a nest or food resource, is essential for survival [29]. One strategy for revisiting a specific location is to use external cues such as chemical signals or visual landmarks [37, 42, 45]. Another strategy that works in visually poor landscapes or featureless environments [5, 23] is to perform path integration, that is, to cumulatively integrate along a path, using a measure of distance traveled (odometry) and body orientation in the direction of travel (heading), thus making it possible to calculate a direct path between any current position and a starting point. Since Darwin first suggested that animals might perform path integration to navigate between food and their nests [11], ample evidence has emerged that many animals employ this strategy. The behavior has been best characterized in ants and bees [9, 17, 30], but has been identified in many species including mantis shrimps [27], bats [2], dogs [32], and rats [41]. Whereas the entire process of path integration is difficult to observe directly, it is often manifest in the act of homing, when an animal executes a straight path (a so-called "home run") back to its nest after completing a tortuous excursion in search of food [25, 35, 38, 43]. Animals can also walk directly from their nest to a food site after their first visit to that location [8, 31, 46]. In all these classic cases with virtuosic path integrators such as ants and honeybees, animals reset their path integrator to zero at their nest or hive location. However, animals without a nest or hive may instead zero their path integrator at a food site or at the center of a cluster of food sites.

Path integration can operate on the scale of hundreds of meters, as exemplified by desert ants [25], or many kilometers, as in bees [9]; however, it can also occur over much smaller spatial scales. In ants, for example, homing is often accompanied by a local search when the forager arrives near the nest, but not near enough to immediately find it [7, 39, 43, 44]. Although seemingly random, these local searches are structured and centered, suggesting the animal is keeping track of its best estimate of the nest's location. Such local searches are not restricted to central place foragers such as ants and bees; for example, hungry blowflies execute local searches in the vicinity of small food items they have sampled, a behavior that Vincent Dethier described as a "dance" [12]. *Drosophila melanogaster* also exhibit these local searches near small spots of food [4, 19]. Optogenetic activation of sugar receptors can substitute for the presence of actual food in initiating this behavior [10, 19]. Fruit flies can perform this food-centered search in the absence of external stimuli or landmarks, indicating that they can rely on idiothetic (internal)

information to keep track of their location [19]. These local searches consist of highly tortuous trajectories in which it is difficult to classify instances when the fly is walking either directly away or toward the food site (e.g., executing a so-called home run), making analysis of the behavior quite challenging.

In this study, we deliberately constrained the two-dimensional motion of flies by confining them to an annular channel. In this constrained arena, local searches consist of back-and-forth runs centered around arbitrarily defined food zones where the flies receive or have recently received optogenetic activation of sugar receptors. Due to its geometric simplicity, our arena allowed us to address several key questions that are difficult to test in an open field arena. By analyzing the flies' behavior after they walked in one or more complete circles around the arena, we provide strong evidence that *Drosophila melanogaster* are capable of two-dimensional, idiothetic path integration to search in the vicinity of a previously exploited food site. In addition, we were able to examine how an animal centers its search excursions when offered a cluster of locations. Our results suggest that rather than using the location of the most recently visited food location to zero their path integrator, flies are able to center their search at a single location within a patch of food.

2.3 Results

Flies remember the position of a single food site

To investigate the behavioral algorithms underlying path integration, we tracked individual flies as they performed local search in an annular arena in which the flies were constrained to walking within a circular channel (Figure 2.1A). Using an automated closed-loop system, we optogenetically activated sugar-sensing neurons whenever the flies (*Gr5a-GAL4>UAS-CsChrimson*) occupied a designated, feature-less food zone. The 1-s optogenetic light pulse triggered by residence in the food zone was followed by a 15-s refractory period during which time the stimulus was kept off, regardless of the fly's position. Aside from these brief optogenetic pulses, all experiments were conducted in complete darkness. For convenience, we sometimes refer to optogenetic food zones as "food" and optogenetic activation events as "food stimuli," although in no cases did the animals experience actual food.

Examples of local searches are plotted in Figure 2.1B, Figure 2.1C, and Figure 2.2. To simplify the display and analysis of the data, we have transformed the curved trajectories of the flies in the circular channel into one-dimensional paths. All experiments began with a baseline period, during which the optogenetic protocol was not operational. This baseline period was followed by an activation period (AP),

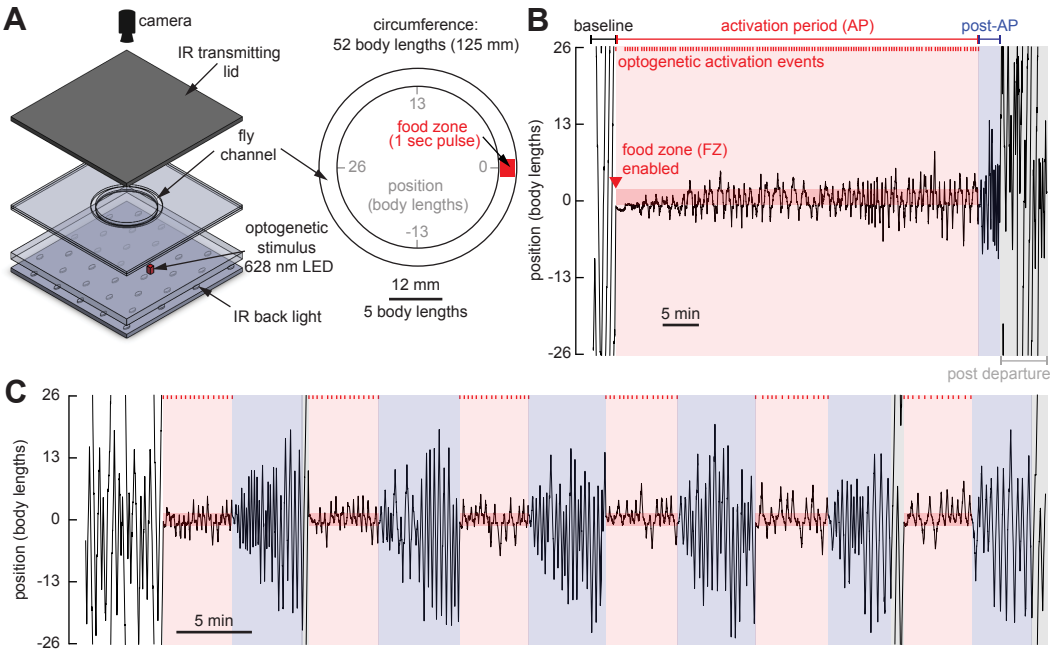

Figure 2.1: Flies perform local search around a fictive food location.
(A) Schematic of the experimental setup (left) and annular arena (right). An overhead camera tracks the position of an individual *Gr5a-GAL4>UAS-CsChrimson* female fly, in real-time, as it explores a 4 mm-wide circular channel, ~52 body lengths (BL) in circumference. Whenever the fly occupies the featureless food zone, it receives a 1-s pulse of optogenetic activation of sugar-sensing neurons via a 628 nm LED positioned beneath the channel, followed by a 15-s refractory period during which the fly cannot receive activation. An infrared (IR) backlight and IR-transmitting lid enable behavioral tracking while otherwise maintaining complete darkness for the fly aside from the brief optogenetic pulses.
(B) Example fly trajectory. To simplify the display and analysis of the data, we transformed the curved trajectories of the flies in the circular channel into a wrapped one-dimensional path. This experiment begins with a baseline period, during which the fly does not receive optogenetic activation, followed by a 40-min activation period (AP, red) during which the optogenetic protocol is operational, followed by a post-activation-period (post-AP, blue) during which the optogenetic protocol is switched off. The post-AP is defined as ending when the fly executes its first run straying more than 26 body lengths (i.e., $1/2$ the arena perimeter) from the food zone, hereafter termed the "departure run." The remaining trajectory is referred to as post-departure (gray). Optogenetic stimulation events during the AP are indicated as red tick-marks (top). See also Figure 2.2A.
(C) As in (B), for an experiment with six serial trials each consisting of a 5-min AP followed by a 5-min post-AP. See also Figure 2.2B.

during which the optogenetic protocol was in effect, i.e., the fly received the 1-s food stimulus followed by the 15-s refractory period whenever it occupied the food zone. Each AP was followed by a post-activation period (post-AP) during which the optogenetic protocol was suspended such that flies did not receive food stimuli. Some experiments consisted of a 40-min AP, followed by a single 10-min post-AP (Figure 2.1B). Other experiments used a repeating trial structure, in which each trial consisted of a 5-min AP followed by a 5-min post-AP (Figure 2.1C).

In the annular arena, flies can either walk clockwise, walk counterclockwise, pause, or reverse direction. We defined the distance between two consecutive reversals as a "run length," r (Figure 2.3A. During the baseline period, flies continuously ex-

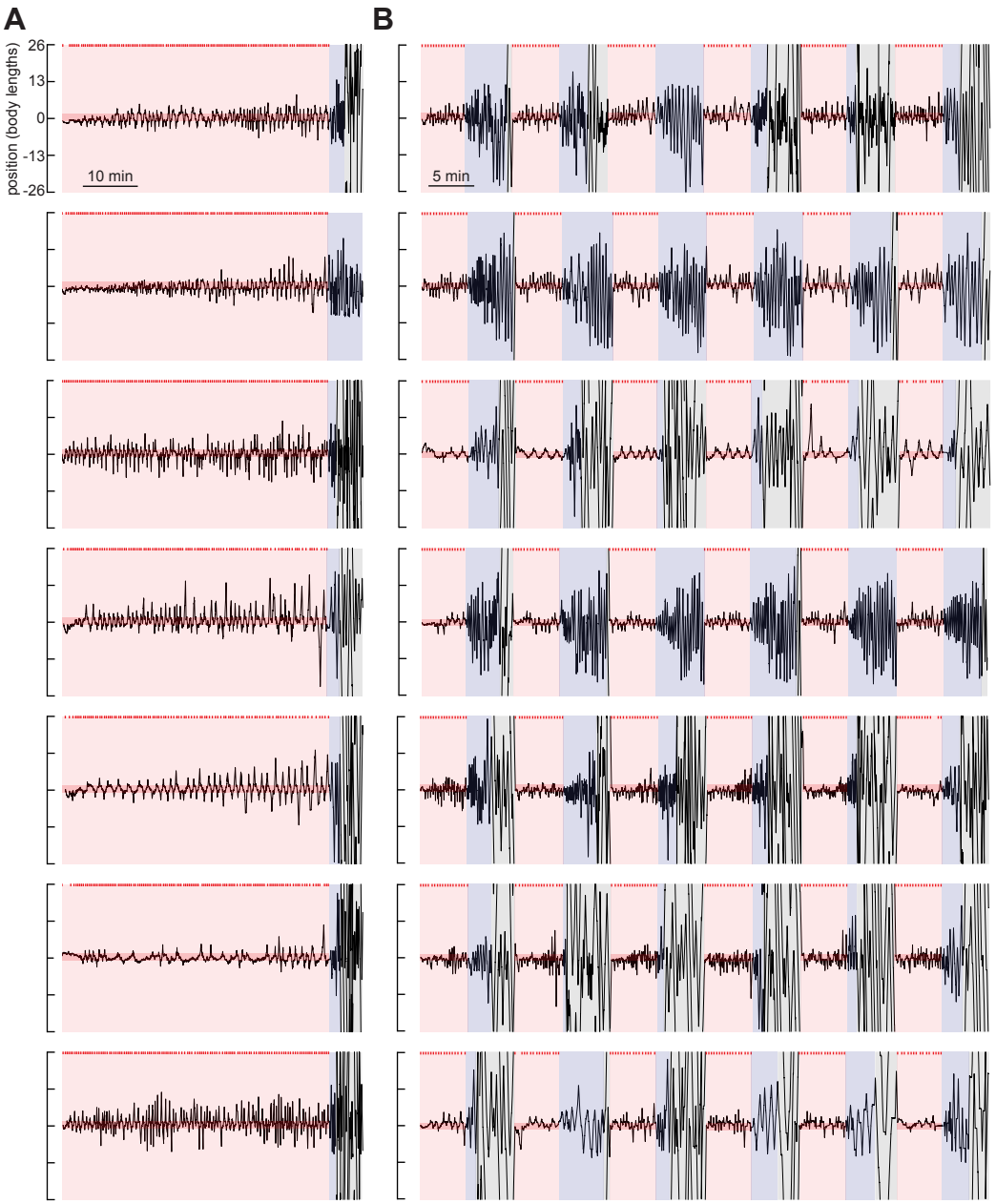

Figure 2.2: Sample trajectories of local search around one fictive food site.
(A) Seven representative example trajectories for the AP and post-AP from single food 40-min AP experiments. Plotting conventions are the same as Figure 2.1B.
(B) Seven representative example trajectories for the AP and post-AP from single food trial-based experiments. Plotting conventions are the same as Figure 2.1C.

plored the entire arena, generally performing long runs interspersed with occasional reversals. During the AP, food stimuli consistently triggered local search excursions typically characterized by a stereotyped sequence of behaviors: upon activation of sugar-receptors, the flies briefly paused, continued to walk a few body lengths away from the food, performed a reversal, returned to the food zone, experienced another food stimulus, and then executed a similar excursion in the opposite direction. This process repeated, producing a persistent zig-zagging search pattern during which the flies explored the channel near the food site, while never straying far in either direction. The excursions were reasonably stereotyped, being ~5 body lengths in size (Figure 2.3B), and did not vary substantially during the AP (Figure 2.3C). We interpret this behavior to be a one-dimensional version of the two-dimensional local searches that were the subject of studies in *Drosophila* [4, 10, 19] in open field arenas, as well as those originally identified by Vincent Dethier in the blowfly, *Phormia* [12]. The relative consistency of these excursion distances in our apparatus was noteworthy, given that there was no external sensory stimulus associated with the termination of each outward run. This suggests that flies' nervous systems intrinsically produce a motor pattern that generates excursions of a particular spatial scale in response to the optogenetic activation that we provided.

The most informative data regarding whether the flies retain a spatial memory of the food location came from the post-AP, when the optogenetic protocol was suspended. Despite no longer receiving food stimuli, flies continued to zig-zag back and forth around the disabled food zone (Figures 2.1B and 2.1C). These post-AP excursions were, however, longer than the AP excursions (mean = 15.1 body lengths) (Figure 2.3D), and tended to increase in length over time toward a plateau by the fifth post-AP run (Figure 2.3E). The length of the first post-AP run (r_1) tended to correlate strongly with the final excursion distance on a trial-by-trial basis (Figure 2.3F). In other words, in our experiments consisting of six successive trials (Figure 2.1C), the length of the final excursion from the food was strongly correlated with the length of the first run past the former food site. This strong positive correlation was observed in nearly every fly tested (Figure 2.3F).

We also observed that most flies eventually abandoned their post-AP search after some time. To specifically analyze trajectories during which the fly was performing local search, we defined the post-AP as starting at the conclusion of the AP and ending with the execution of what we classified as a "departure run." The departure run was defined as the first run after the conclusion of the AP during which the fly strayed 26 or more body lengths away from the food zone, thus reaching or

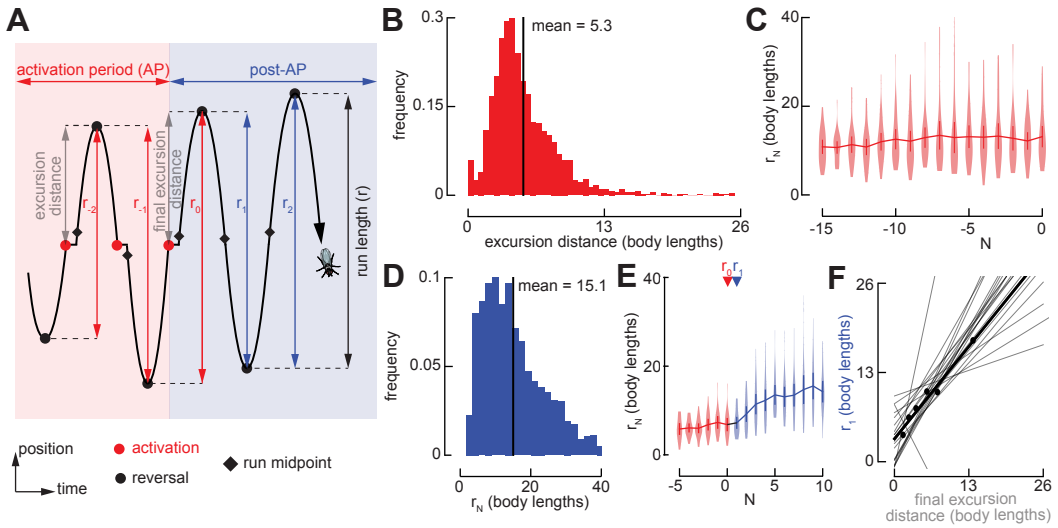

Figure 2.3: Repeated back-and-forth excursions constitute a local search around a fictive food location.
(A) Schematic, showing features of local search. After encountering a food stimulus during the AP, flies walk a given excursion distance (gray), reverse direction, and perform a run back toward the food. The distance between two consecutive reversals is a run length (r), where r_0 is the run length between the final reversal of the AP and the first reversal of the post-AP, and all other runs are numbered with respect to r_0. The run midpoint is defined as the halfway point between two consecutive reversals.
(B) Distribution of all excursion distances from the 40-min AP experiments as in Figure 2.1B (n = 29 flies, 2,494 food excursions).
(C) Run lengths for the final 16 runs of the AP, including r_0, averaged over trials from the 40-min AP experiments. Data from trials with fewer than 16 AP runs are included (N = 29 flies). Throughout the chapter, error bars depict 95% confidence intervals and violin plots indicate full data distributions.
(D) Mean distribution of the run lengths of the post-AP from the trial-based experiments as in (C) (n = 22 flies, 110 trials).
(E) Run lengths for the final 6 runs of the AP, including r_0, and the first 10 runs of the post-AP, averaged over trials from the trial-based experiments as in 2.1C (n = 22 flies, 110 trials). Labels indicate the final run of the AP (r_0) and the first run of the post-AP (r_1).
(F) Relationship between the final excursion distance during the AP and the first run of the post-AP (r_1). Black dots indicate r_1 versus last excursion for 6 trials from the fly in Figure 2.1C, and the black line indicates the linear regression for this fly. Grey lines indicate linear regressions for all remaining flies with data from at least 3 trials (N = 20 flies).

passing the opposite side of the arena. The total duration of the post-AP trajectory varied—some flies abandoned the food after 1–2 min, whereas others continued searching for the full 5 min of the post-AP (Figure 2.4A). Regardless of the duration of the post-AP search, the departure run was almost always considerably longer than all the preceding runs (Figures 2.4B and 2.4C). In other words, rather than slowly expanding or drifting away from the food site, flies typically terminated the post-AP search by performing an exceptionally long run, perhaps reflecting a change in the fly's behavioral state.

To derive an estimate of the flies' spatial memory within the arena, we developed a method by which we measured the midpoint of each run and then convolved each of these locations with a narrow von Mises distribution ($\kappa = 200$), the sum of which generated a kernel density estimate (KDE) of where in the arena the fly was focusing

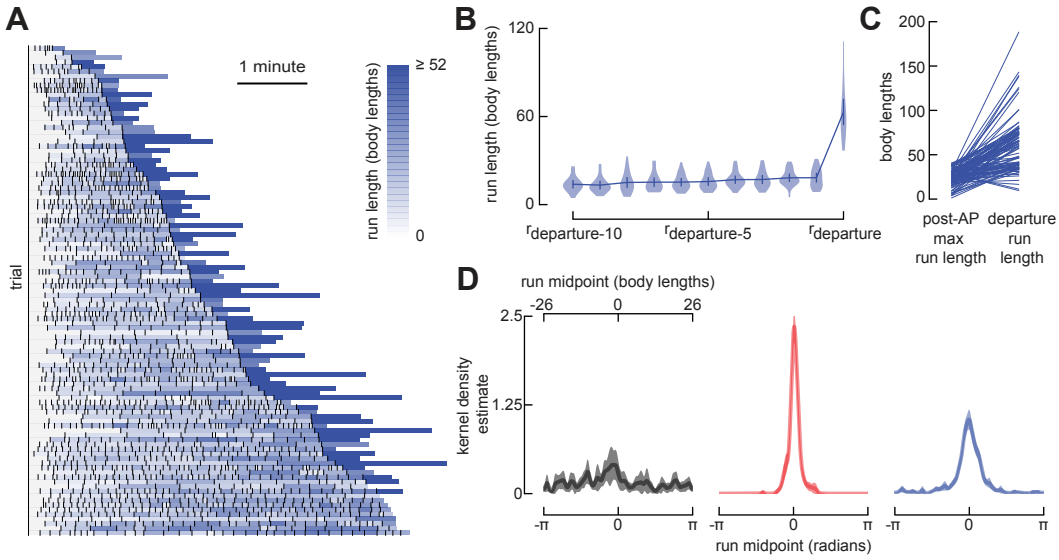

Figure 2.4: Flies terminate their post-AP search with a particularly long run.
(A) Sequences of post-AP runs and their associated departure run, sorted by the duration of the post-AP. Each row corresponds to a single trial from experiments as in 2.1C, where the length of each box corresponds to the duration of each run, and the color of each box indicates run length (n = 22 flies, 110 trials). Note that in 11 trials at the bottom of the panel, the flies did not execute a departure run before the next AP began.
(B) Run lengths for the final 10 runs of the post-AP, as well as the departure run, averaged over trials from data in (A). Data from trials with fewer than 10 post-AP runs are included. Error bars depict 95% confidence intervals and violin plots indicate full data distributions.
(C) Length comparison of the longest post-AP run and corresponding departure run for each trial, from data in (A). The 11 trials without a departure run were not included in this analysis.
(D) Normalized kernel density estimate (KDE) of the run midpoint in baseline (left), AP (middle), and post-AP (right) (n = 22 flies). Throughout the chapter, shaded regions indicate 95% confidence interval. Throughout the chapter, the KDE is calculated for each fly for k = 200 and then the mean and 95% confidence interval is calculated for the individual fly's KDE. For post-AP comparison with simple models, with run lengths randomly drawn from either the empirically derived data shown in (A) (excluding the departure runs), or a Lévy distribution fit to the same data, see Figure 2.6.

its search. The KDE for the baseline (pre-AP) data was flat and noisy, indicating that the flies' runs were not centered on any particular location within the arena (Figure 2.4D, left panel). In sharp contrast, the KDEs from the AP and post-AP data were unimodal with a clear peak at the location of the food (Figure 2.4D, center and right panels). The food-centered peak is expected for the AP, but its existence for the post-AP data is indicative of the flies' memory of the food site. We will make use of run midpoint KDEs throughout the chapter as a means of assessing the flies' spatial memory under different conditions.

Flies recognize a former food site after walking completely around the arena

Our analysis of the flies' search behavior prior to the departure run suggests that they can remember the location of the food, a task they could accomplish using one-dimensional odometry (e.g., by simply counting the number of steps taken away from and back toward the food). However, the fact that some flies traveled all the

way around the arena after the departure run allowed us to test whether the flies could perform full two-dimensional path integration, a task that would require integrating odometry with their internal compass sense. To test this hypothesis, we conducted experiments in a smaller (~26 body length circumference) circular channel (Figure 2.5A) to increase the probability that the flies would walk one or more times around the arena during the post-AP. We exposed flies to six 5-min APs separated by 5-min post-APs, in which each pair of APs and post-APs constitutes a single trial. To ensure that flies could not use their own chemical signals or other external features to recognize the food site, we switched the food zone between two locations, spaced 180° apart, for each AP—i.e., during the 1st trial, the food zone was on the right side of the arena, during the 2nd trial, the food zone was on the left side of the arena, etc (Figure 2.5A). We classified a post-return period, starting when the fly reached 1 full revolution (26 body lengths) away from the food site. After seeming to abandon their local search during the post-AP, many flies reinitiated search at the former food site, after completing one or more full revolutions around the arena (Figure 2.5B-2.5E). The flies' performance was quite variable in this task, with some flies exhibiting much stronger search behavior after circling the arena than others. Nevertheless, the transit probability averaged across all flies during the post-return period shows clear peaks at the location of the former food zone at integer values of full revolutions within the arena (Figure 2.5C-2.5E), and the average KDE of the run midpoint distribution exhibited a peak at the former food location (Figure 2.5F). As described above, these experiments were conducted by changing the position of the food site from one side of the arena to the other in alternate trials, to control for the possibility that flies were simply depositing some chemical cue when they encountered food, which they subsequently used to relocate that position. If this were the case, we would expect that the KDEs would show two peaks, one at each of the alternating food locations. This is not what we found; instead, flies showed no preference for searching at the position of the food zone from the immediately preceding trial (Figure 2.5G), suggesting that they are not remembering the food site via chemical cues deposited there.

An agent-based model recapitulates Drosophila local search behavior

To investigate possible algorithms underlying local search, we constructed different agent-based models of the flies' behavior. The output of each model—a time series of the fly's position—is generated by a sequence of simulated runs and reversals. First, we tested whether simple models, with run lengths randomly drawn from either

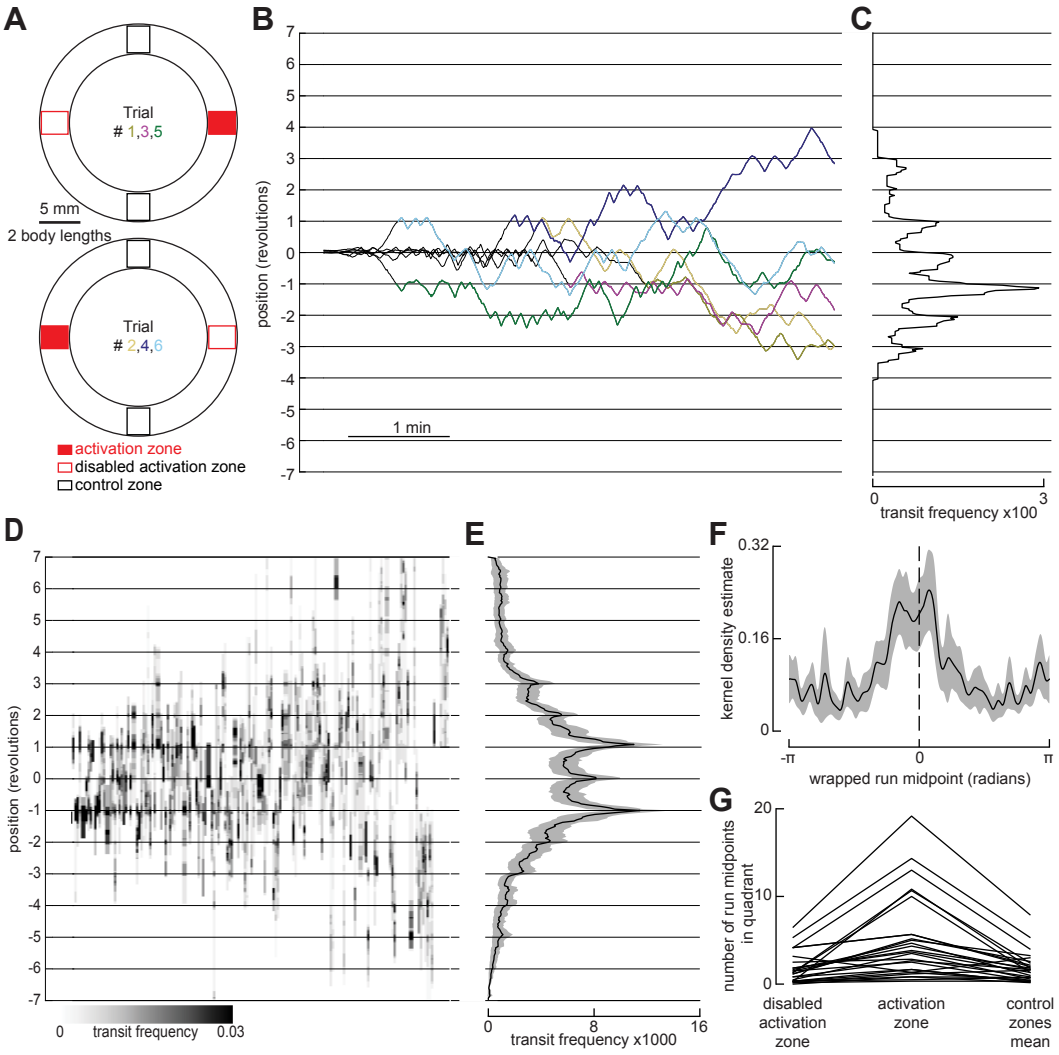

Figure 2.5: Flies reinitiate a local search at a former fictive food site after circling the arena.
(A) Schematic of the smaller annular arena (~26 body lengths), indicating the location of the food zone for each trial, as well as control zones used for analysis. Experiments were done as in Figure 2.1C, but each food zone was 1.3 body lengths, and the food zone location was alternated from trial to trial.
(B) Example pre-return (before the fly has circled the arena at least once during the post-AP, gray) and post-return (colored) trajectories from a single experiment where each line corresponds to a single trial and shows the unwrapped trajectory, with gridlines indicating full revolutions around the arena. To align data for analysis, trajectories from even-numbered trials were shifted such that the location of the food zone is always at 0. For the model recapitulating fly reinitiation of local search at a former fictive food site after circling the arena, see Figure 2.15.
(C) Mean distribution of fly transits for post-return trajectories in (B). Transits were calculated using bins 2 BL wide and counted when a fly entered a bin from one side and exited the bin from the other side.
(D) Heatmap indicating distribution of transits during post-return trajectories, calculated using 4 bins per revolution (dividing the arena into quadrants centered on the food zone, disabled food zone, and each control zone). Each column represents a single trial, with columns sorted by frequency of transits at the 1 or -1 revolution position (n = 28 flies, 168 trials).
(E) Mean transit distribution for data in (D). Shaded region indicates 95% confidence interval.
(F) Normalized kernel density estimate (KDE) of the wrapped run midpoint in the post-return period (n = 28 flies). Shaded region indicates 95% confidence interval.
(G) Number of run midpoints in each arena quadrant during post-return trajectories (n = 28 flies). Each line shows the values for a single fly, where data from both control quadrants were averaged together.

the empirically derived data shown in Figure 2.4A (excluding the departure runs) or a Lévy distribution fit to the same data, could recapitulate the flies' behavior during the post-AP. In both of these cases, the models failed to produce a sustained, centered local search; the simulated flies quickly strayed from the trajectory origin (Figure 2.6. These results suggest that real flies must somehow remember the location of the former food site, and that the centeredness of the post-AP search is not simply a result of starting at the former food location.

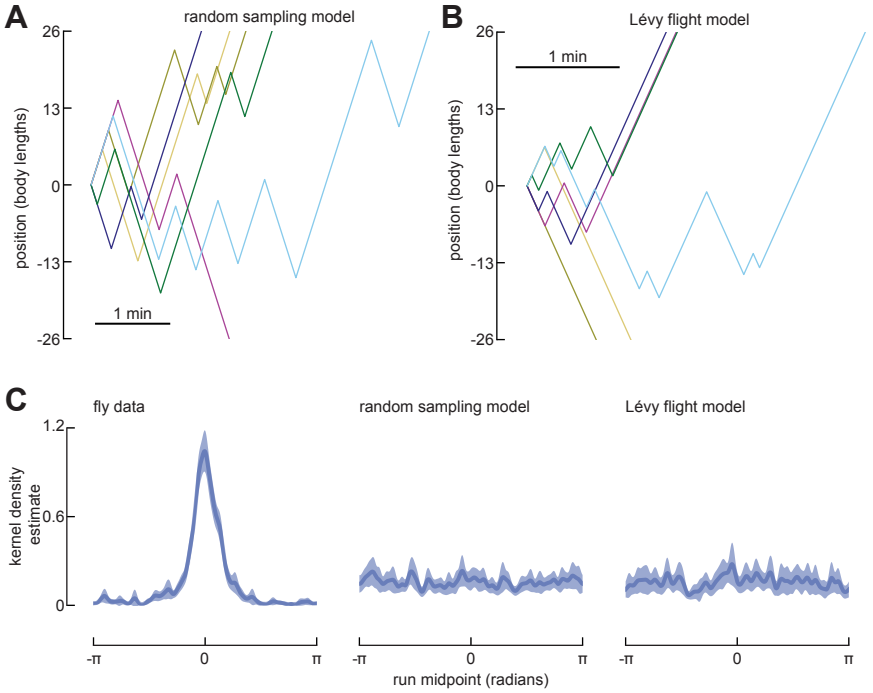

Figure 2.6: Memory-less models cannot recapitulate *Drosophila* local search.
(A) Six representative example trajectories from simulations for which run lengths were randomly drawn from the distribution of run lengths in Figure 2.4A (excluding the departure runs). Trajectories begin at the 0 position and are terminated when the simulated fly reaches 26 body lengths from the point of origin.
(B) As in (A) from simulations for which run lengths were drawn from a Lévy distribution fit to the distribution of run lengths in Figure 2.4A (excluding the departure runs).
(C) Normalized kernel density estimate (KDE) of the wrapped run midpoint in the post-AP period for fly data (re-plotted from the right panel in Figure 2.4D), random sampling model (n = 300), and Lévy flight model (n = 300).

To account for the flies' ability to remember the location of the food, we developed an agent-based, state-transition model (hereafter, food-to-reversal or FR model) that posits the flies' ability to integrate the distance between the food site and the point at which they reverse direction at the end of each excursion. Figure 2.7A shows a simple state transition depiction of this model, with a more formal presentation provided in Figure 2.8. State-transition diagrams are commonly used in computer science to model systems—self-driving cars, for example [3, 16, 28]—where an agent can assume finite states regulated by stochastic or deterministic transitions. In

the FR model, flies are initialized in a global search mode and enter a local search mode when they encounter a food stimulus. When in local search mode, simulated flies use odometry to keep track of their distance walked, and when they have completed their target run length, they perform a reversal and select a new target run length as a function of the prior run length. The output of the model—a time series of the fly's position—captures salient features of the behavior of real flies during both the AP and post-AP periods (Figures 2.7B-2.7D). To account for the flies' ability to remember the location of the food site after walking completely around the arena (during the post-return period), the FR model incorporates two orthogonal path integrators and can thus keep track of the food site in two dimensions (Figures 2.7E-2.7H). This is, in essence, a path integration model, wherein the integrators are set equal to zero upon experience with a food stimulus and a run length is selected. When the fly has deviated a distance from the food site equal to the run length, as measured by the Euclidean norm of the integrators, the fly executes a reversal, zeros its integrators, and selects a new run length as a function of the previous distance walked. The integrators are noiseless, such that the simulated fly has perfect knowledge of its location relative to the food site. We emphasize, however, that this is a purely algorithmic model and we are not asserting whether or not it might be implemented in a neurally plausible manner. The salient feature of the model, however, is that its path integrator is zeroed at the location of the food site and accumulates distance until the fly reverses direction.

Flies expand and recenter their search area to span multiple food sites

We next tested how flies perform local searches within arenas that contain multiple food sites. We modified our annular arena to feature two food zones, separated by 9 body lengths (60°) within the channel. As expected, flies began searching around the first food site they encountered. However, on occasions where the fly encountered the second food site during the course of the search, they often expanded their search area to span both food sites (Figures 2.9A and 2.10A). We also repeated the two-food experiments with a configuration in which the food was separated by 13 body lengths (90°). Although the results were generally consistent with the data collected with a shorter food separation distance (Figures 2.9A and 2.10), it often took the fly longer to find the second food site at the start of the experiment. These experiments with a large separation between food zones underscore the salient phenomenon that the flies' inward excursions toward the other food zone were substantially longer than their typical outward excursions—an observation that again suggests that their

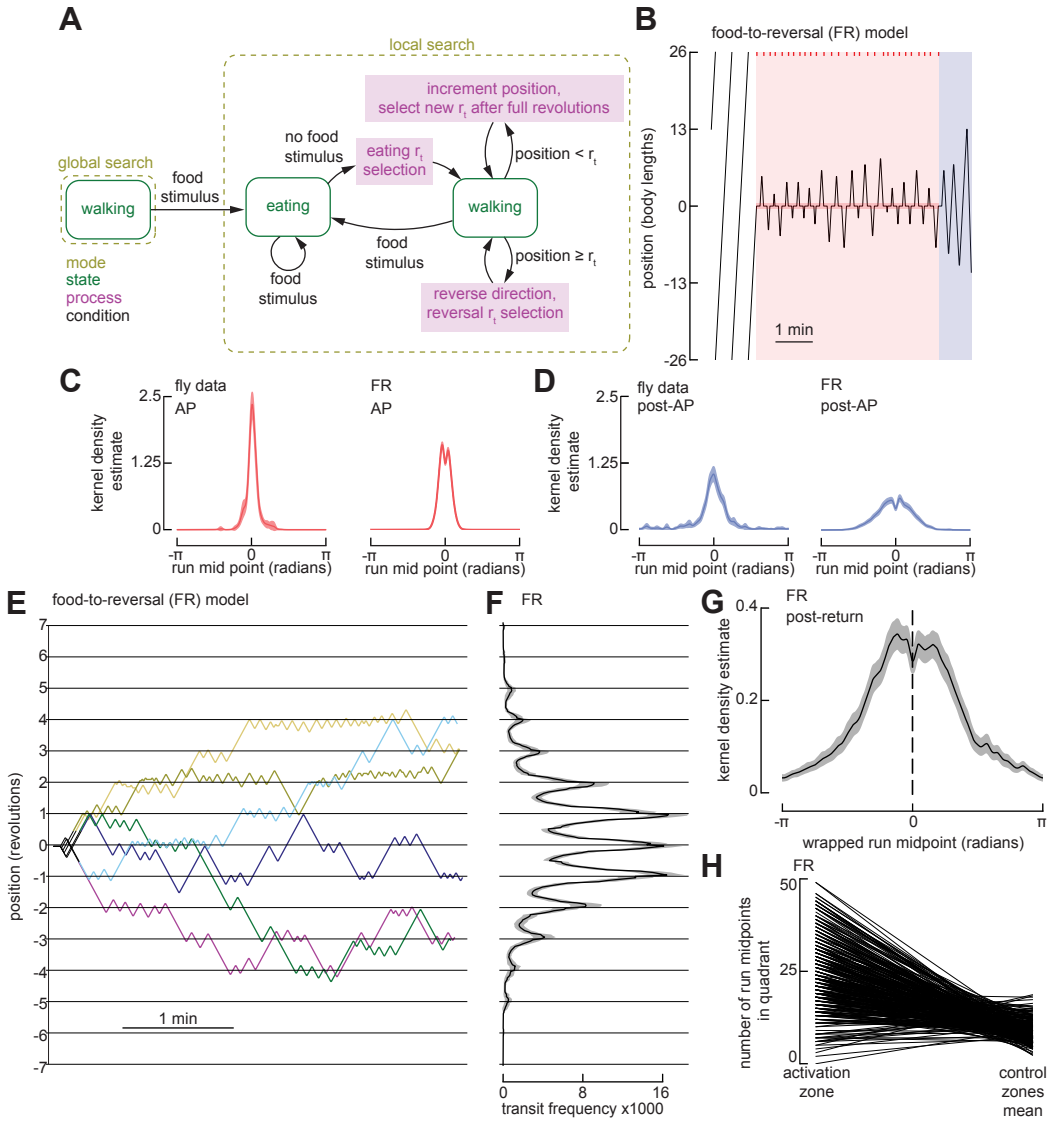

Figure 2.7: An agent-based model using iterative odometric integration recapitulates Drosophila local search around a single fictive food site.
(A) Schematic of the state-transition diagram for an agent-based model. Arrows indicate transitions—governed by conditions—between search modes, behavioral states, and computational processes. For detailed state transition diagrams, including that of the simulated environment, see Figure 2.8.
(B) Example trajectory of FR model simulation in a circular arena with a 52-body length circumference, showing baseline, AP, and post-AP. Plotting conventions as in Figure 2.1B.
(C) Normalized kernel density estimate (KDE) of the run midpoint in during AP for flies (left, n = 22 flies) and FR model (right, n = 300 simulations). Data for the fly are re-plotted from Figure 2.4D. Shaded regions indicates 95% confidence intervals.
(D) Normalized kernel density estimate (KDE) of the run midpoint during the post-AP for flies (left, n = 22 flies) and FR model (right, n = 300 simulations). Data for the fly are re-plotted from Figure 2.4D. Shaded regions indicates 95% confidence intervals.
(E) Six representative example trajectories of FR model simulation in a small circular arena with a 26-body length circumference (same as experiments in Figure 2.5). Plotting conventions as in Figure 2.5B.
(F) Mean transit distribution for FR simulations in small arena (n = 300). Plotting conventions as in Figure 2.5E. Shaded region indicates 95% confidence interval.
(G) Normalized kernel density estimate (KDE) of the wrapped run midpoint in the post-return period for FR simulations in small arena (n = 300). Plotting conventions as in Figure 2.5F. Shaded region: 95% CI.
(H) Number of run midpoints in the food quadrant compared to the other three quadrants during post-return trajectories for FR simulations in small arena (n = 300). Each line shows the values for a single simulation, where data from all three control quadrants were averaged together.

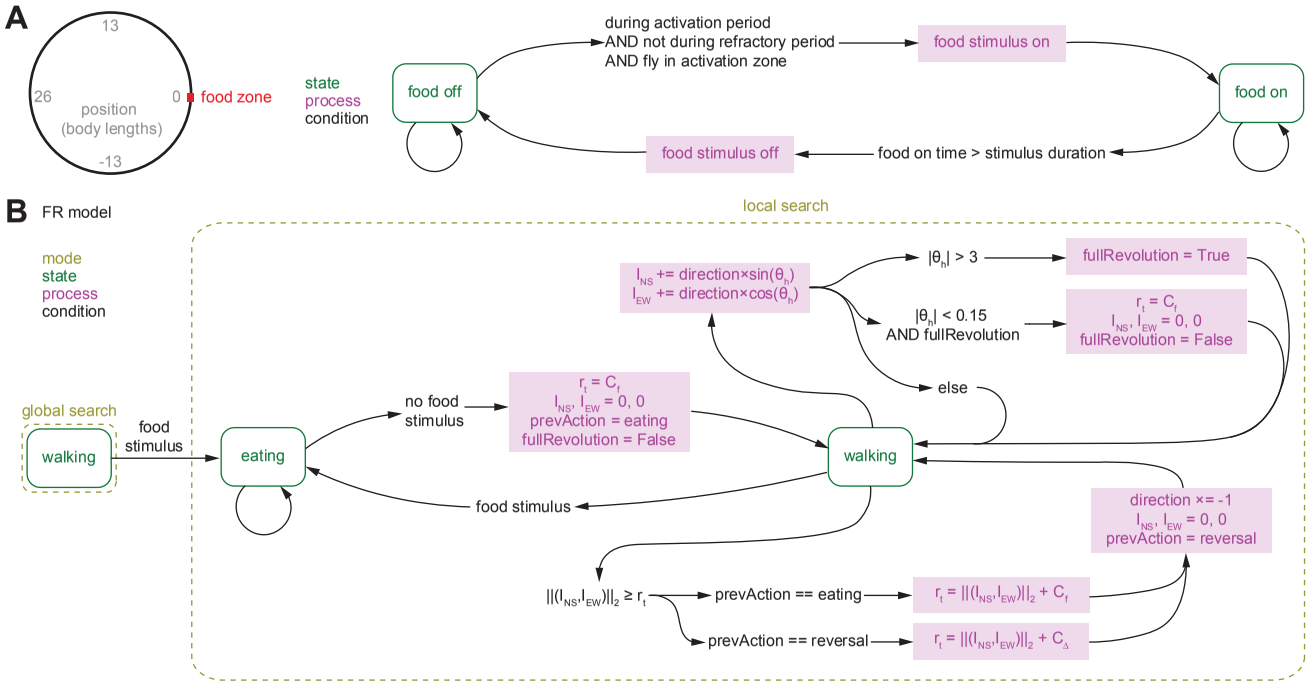

Figure 2.8: State-transition diagrams describing agent-based odometric integration models of *Drosophila* local search.
(A)Simulated environment. Left: Schematic of the simulated environment. The example shown here is for a simulated environment with a single food zone. Right: State transition diagram for the simulated environment. The simulated environment is in either the food on or off state. Transitions between these states, via processes, are determined by the conditions at each timestep of the simulation. See methods for details.
(B)State transition diagrams for the FR model. The simulated fly can either be in an eating or walking state, within either a global or local search mode. Transitions between these states and modes, sometimes via processes, are determined by the conditions at each timestep of the simulation. (r_t = target run length, BL = body lengths, I = Integrator, N = North, S = South, E = East, W = West, θ_h = heading angle, prevAction = previous action, firstRev = first reversal). The variables C_f, C_Δ, $C_{\Delta,\text{AP}}$, and $C_{\Delta,\text{post-AP}}$, represent a value drawn from the corresponding distribution. See methods for details.

behavior involves some sort of odometric memory that allows them to keep track of the location of two food sites.

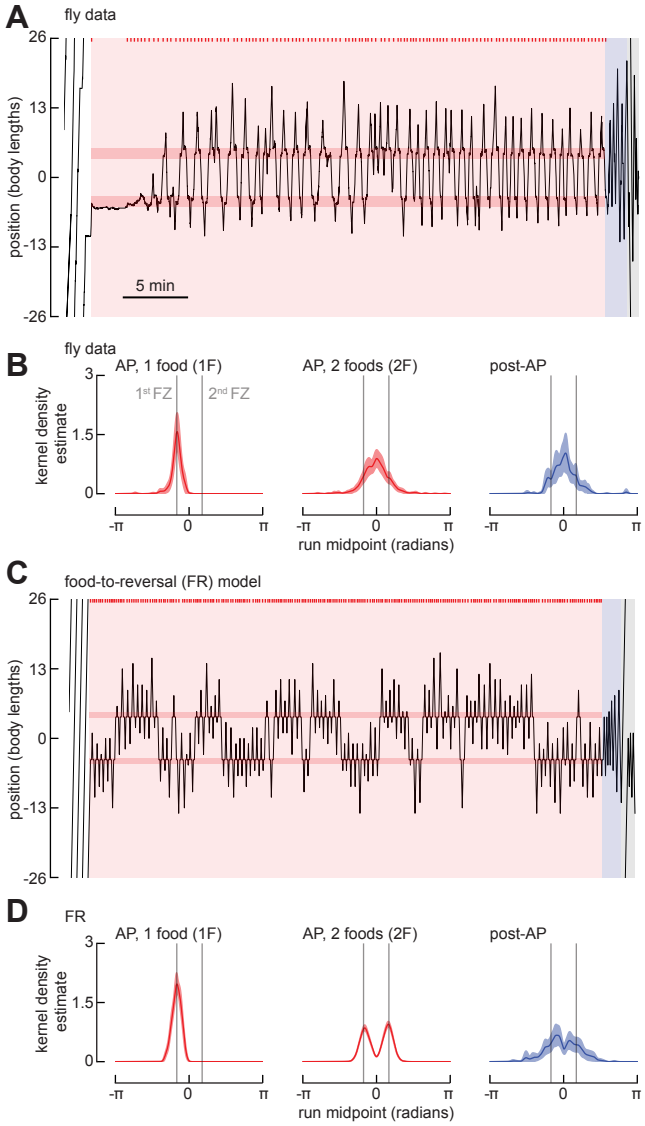

Figure 2.9: The FR model fails to predict Drosophila search behavior around multiple fictive food sites.
(A) Example trajectory of a fly exploring an annular arena with two food zones, spaced 9 body lengths (BL) apart. The experiment consists of a baseline period, AP, and post-AP. Plotting conventions as in Figure 2.1B. See also Figure 2.10A. For trajectories of flies exploring an annular arena with two food zones, spaced 13 body lengths (BL) apart, see Figure 2.10B.
(B) Normalized KDE of the run midpoint for one-food search (1F, left), the two-food search (trajectory after the fly has encountered the 2nd food zone, 2F, middle), and the post-AP (right). To align data for analysis for 1F, trajectories for flies that found the food located at +4.5 BL first were shifted such that the first food for all flies is ~4.5 BL (n = 29 flies). Shaded regions indicate 95% confidence intervals.
(C) As in (A) for a simulation using the FR model.
(D) As in (B) for the FR model. The first 300 simulations in which the virtual fly found both food sites are included (n = 300). Shaded regions indicate 95% confidence intervals.

To assess the flies' behavior during the AP, we segmented the data into the initial segments before they found the second food site and the remaining segment after

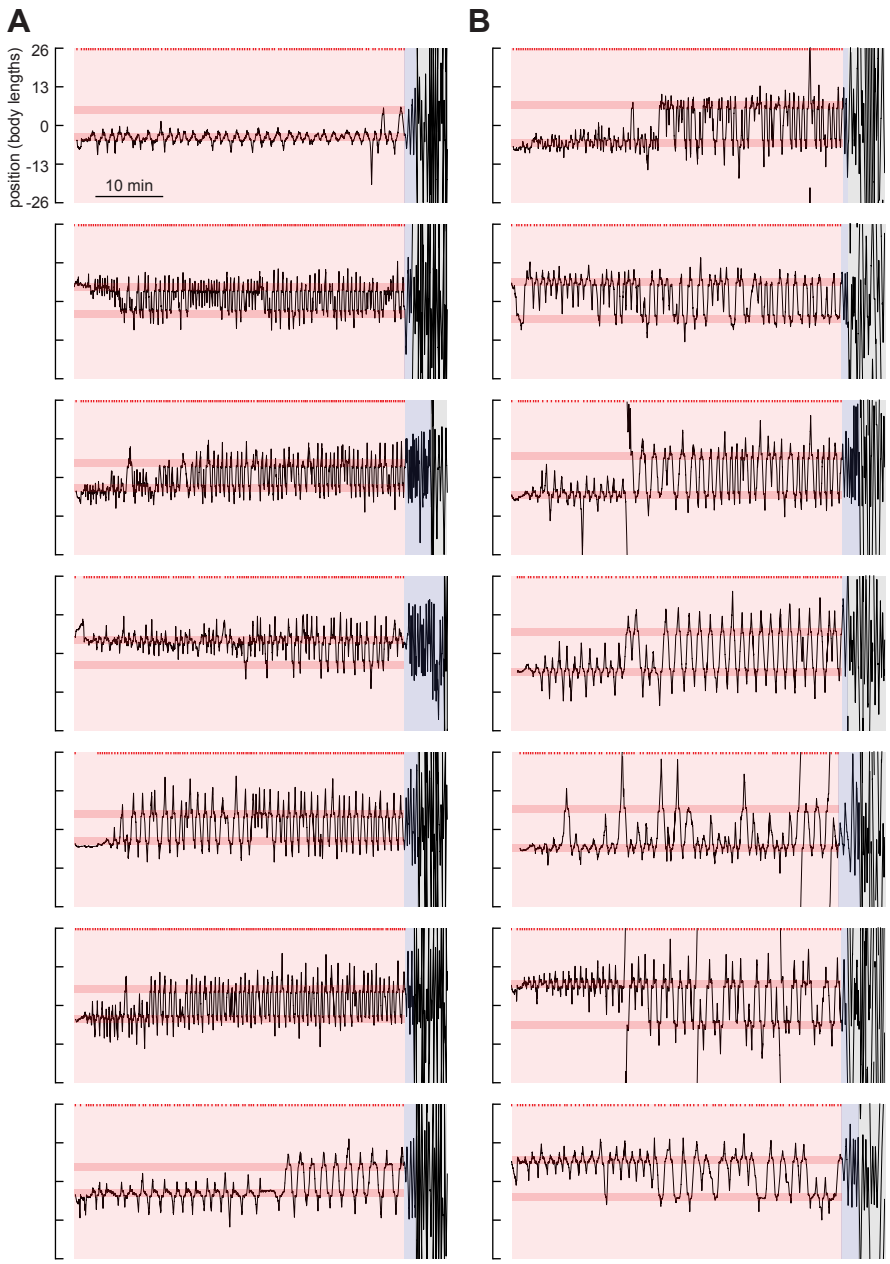

Figure 2.10: Sample trajectories of local search around two fictive food sites.
(A) Seven representative example trajectories for the AP and post-AP from two-food 40-min AP experiments. The two food zones are spaced 9 body lengths (BL) apart. Plotting conventions are the same as Figures 2.1B and 2.9A. (D) Seven representative example trajectories for the AP and post-AP from two-food 40-min AP experiments. The two food zones are spaced 13 body lengths (BL) apart. Plotting conventions are the same as Figures 2.1B and 2.9A.

they first encountered the second food. We also inverted roughly half of the traces so that all the flies start the AP by foraging around the lower food position (as plotted in 2.9A). As expected, the run midpoint KDE generated from all the initial segments were centered around the lower food position; however, the KDE generated from the data following discovery of the second food was centered at a location roughly midway between the two food sites, as was the KDE generated from runs during the post-AP (2.9B), suggesting that the fly remembers a position midway between the two food sites. We ran our FR model on the same experimental conditions and analyzed the trajectories in the same manner (Figures 2.9C and 2.9D); however, the results failed to replicate the flies' behavior. During the AP, the simulated flies tended to transition back and forth between local searches around one food site or the other—rarely generating a stable oscillation across the two—and the KDE distribution in the post AP exhibited two peaks (Figure 2.9D). Thus, while capturing the salient features of flies' behavior when searching in the vicinity of one food site (Figure 2.7), the FR model failed to recapitulate the behavior of real flies when searching around two sites (Figure 2.9).

Based on the failure of the FR model, we developed two distinct models that might explain the flies' behavior when foraging amid two feeding sites; these are depicted diagrammatically in Figures 2.11B and 2.11C and more formally in Figures 2.12 and 2.13. In the FR model, experience with any active food zone zeroes all path integrators; the fly therefore integrates from the food site most recently encountered (Figure 2.11A). At a reversal, the next run length is calculated as the sum of a randomly distributed variable and the integrated value. Because the integrated value is only the distance to the nearest food, the search is always centered over one food site rather than the entire food patch (Figure 2.9C). The first of the two new models, which we call FR', differs from the simpler FR model most notably in what triggers the zeroing of the path integrators. Whereas the FR model is always zeroed when food is encountered, the FR' model only zeroes its integrators at the first encounter with a food following a reversal; if a fly experiences a second food site before changing direction, the integrators continue to accumulate (Figure 2.11B). Thus, when the next run length is calculated at a reversal, the integrated value will take the fly fully back across the entire food patch to the first food site encountered, and the random variable value will ensure the fly continues past that point a short distance. This feature of the FR' model is able to generate more realistic trajectories in which the simulated fly often zig-zags back and forth across the two food zones (Figure 2.11D). The FR' model does not require the fly to zero its path integrators at

a location that is not directly associated with a sensory stimulus (e.g., food sensation) or motor action (e.g., run reversal). Further, the FR' model is intrinsically reflexive and does not require that the fly somehow keep track of the number of food sites visited.

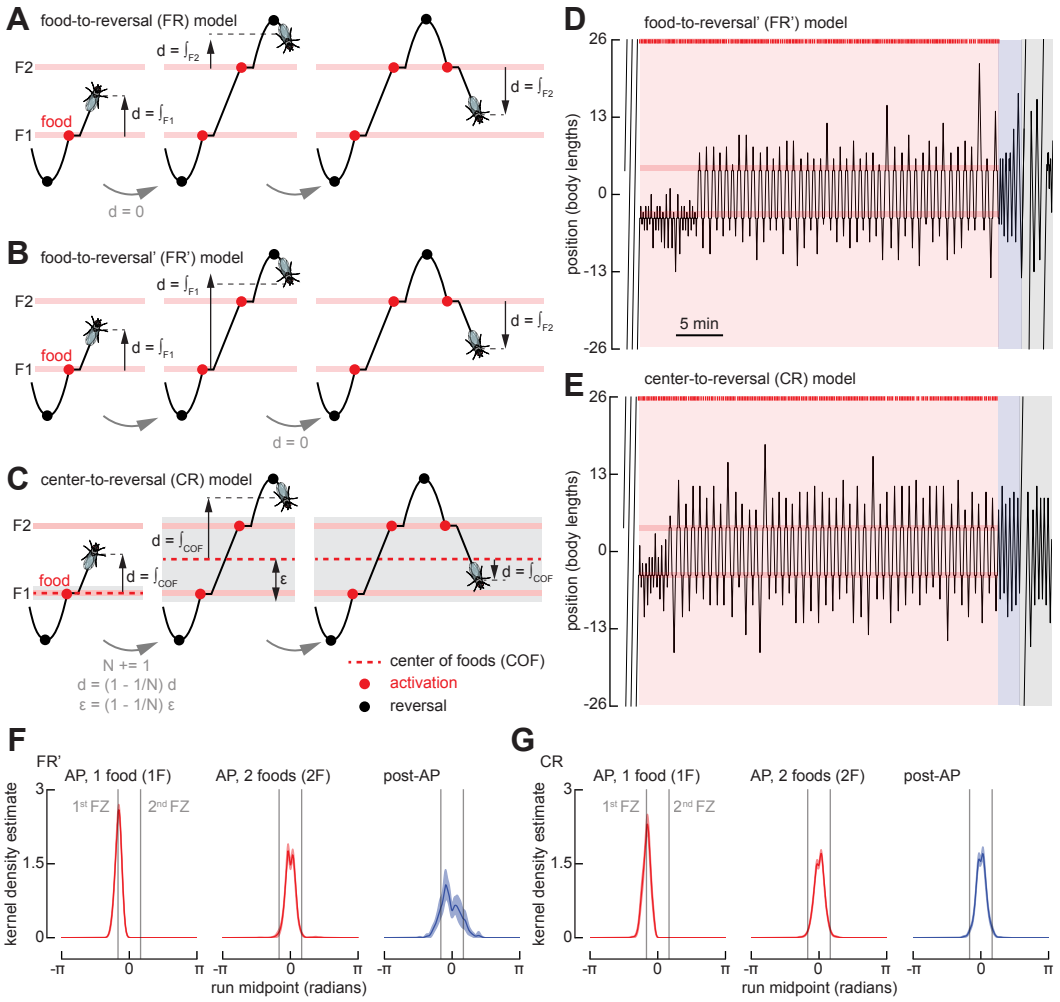

Figure 2.11: Two modified versions of the FR model recapitulate Drosophila search behavior around multiple fictive food sites.
(A) Schematic showing features of food-to-reversal (FR) model. The virtual fly resets its integrator at each new food that it encounters.
(B) As in (A) for food-to-reversal0 (FR') model. The virtual fly resets its integrator at the first food encountered after each reversal.
(C) As in (A) for center-to-reversal (CR) model. The virtual fly resets its integrator at the center of all the food locations it encounters during a run. (D) As in Figure 2.9A, for a simulation using the FR' model.
(E) As in Figure 2.9A, for a simulation using the CR model.
(F) As in Figure 2.9B, for simulations using the FR' model. The first 300 simulations in which the virtual fly found both food sites are included (n = 300). Shaded regions indicate 95% confidence intervals.
(G) As in Figure 2.9B, for simulations using the CR model. The first 300 simulations in which the virtual fly found both food sites are included (n = 300). Shaded regions indicate 95% confidence intervals.

An alternate, the center-to-reversal (CR) model (Figure 2.11C), is based on the notion that the fly can compute and store the coordinates of a location that is at the

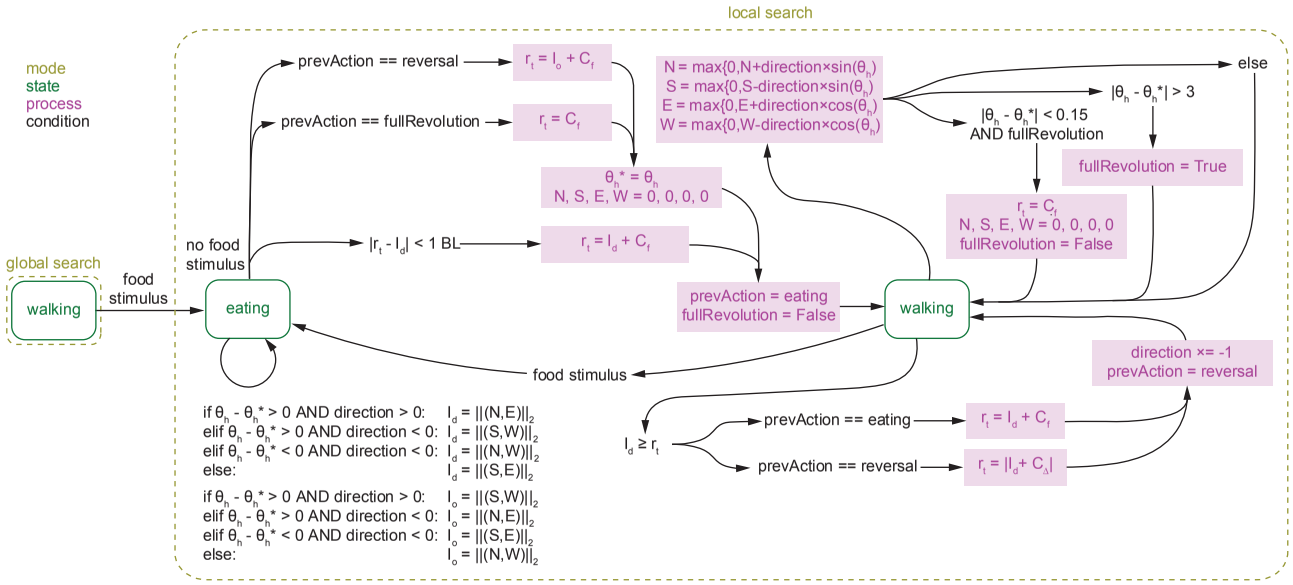

Figure 2.12: State transition diagrams for the FR' model. The simulated fly can either be in an eating or walking state, within either a global or local search mode. Transitions between these states and modes, sometimes via processes, are determined by the conditions at each timestep of the simulation. (r_t = target run length, BL = body lengths, I = Integrator, N = North, S = South, E = East, W = West, θ_h = heading angle, prevAction = previous action, firstRev = first reversal). The variables C_f, C_Δ, $C_{\Delta,\text{AP}}$, and $C_{\Delta,\text{post-AP}}$, represent a value drawn from the corresponding distribution. See methods for details.

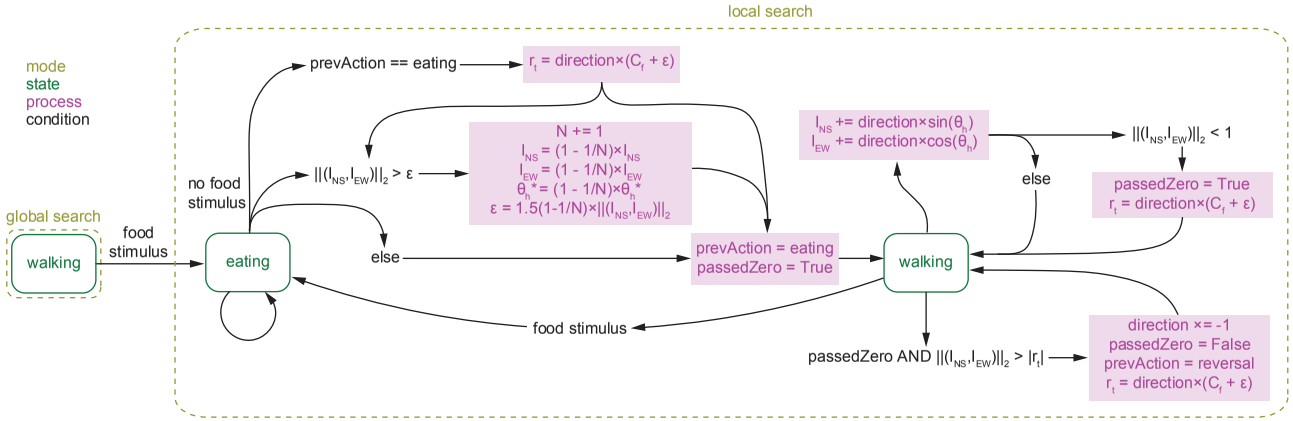

Figure 2.13: State transition diagrams for the CR model. The simulated fly can either be in an eating or walking state, within either a global or local search mode. Transitions between these states and modes, sometimes via processes, are determined by the conditions at each timestep of the simulation. (r_t = target run length, BL = body lengths, I = Integrator, N = North, S = South, E = East, W = West, θ_h = heading angle, prevAction = previous action, firstRev = first reversal). The variables C_f, C_Δ, $C_{\Delta,\text{AP}}$, and $C_{\Delta,\text{post-AP}}$, represent a value drawn from the corresponding distribution. See methods for details.

center of a cluster of food sites—the center of foods (COF); it is at this location where the path integrators begin to accumulate. When only one food site is present, the COF coincides with the food site and the model integrates from that location, as in the FR and FR' models. However, when the fly encounters a second food site, it shifts the origin of its search to a location between the two food sites. To distinguish new food sites from previously encountered sites, the simulated fly also calculates the rough size of the food patch, ε. If the fly encounters a food site when its integrator exceeds ε, both the integrators and ε are updated such that the origin is always at the COF. The model implements a simple algorithm to place the COF at the center of mass of all known food sites and to calculate ε as the distance from the COF to the outermost food site. We are not inferring that this is a biologically plausible mechanism by which such calculations might be implemented—indeed, many simple mechanisms are possible to maintain an estimate for the center of the food patch. The important distinction is that, in the CR model, the fly can estimate the center of the food sites it has encountered and this calculation requires some short-term memory; its behavior cannot be explained by a reflexive action to the last food site visited. Despite the fact that the model parameters were determined via a grid search on the one food configuration dataset, both the FR' and CR models do a reasonable job of recapitulating the flies' behavior in a two-food geometry, in that KDEs of the run midpoint distributions are unimodal during both the AP and post-AP periods (Figures 2.11F and 2.11G).

To test between the FR' and CR models, we modified the arena to feature three food zones, spaced 4.5 body lengths apart (Figure 2.14A). We changed our optogenetic protocol such that, at the end of the AP, we disabled all but one of the food zones, which remained active for just one single additional visit (Figure 2.14B). The FR' and CR models make very different predictions under these conditions. In the FR' model, the position of the expected run midpoint during the post-AP is strongly dependent upon the position of the last food site encountered, whereas this is not the case with the CR model. As shown in Figure 2.14, the run midpoint KDEs measured from real flies are indistinguishable in the three experimental conditions (final food at top, middle, or bottom position), and were centered at a point corresponding to the middle food site, which matches the prediction of the CR model. These results support the basic assumptions of the CR model, which is that the fly can somehow retain and update a memory of the center of the food patch over time as it zig-zags back and forth across the individual food sites, and this memory is not dependent on the location of the last active food site it encountered. The CR model also

successfully recapitulates flies' behavior in reinitiating the search after completing one or more circles around the arena (Figure 2.15).

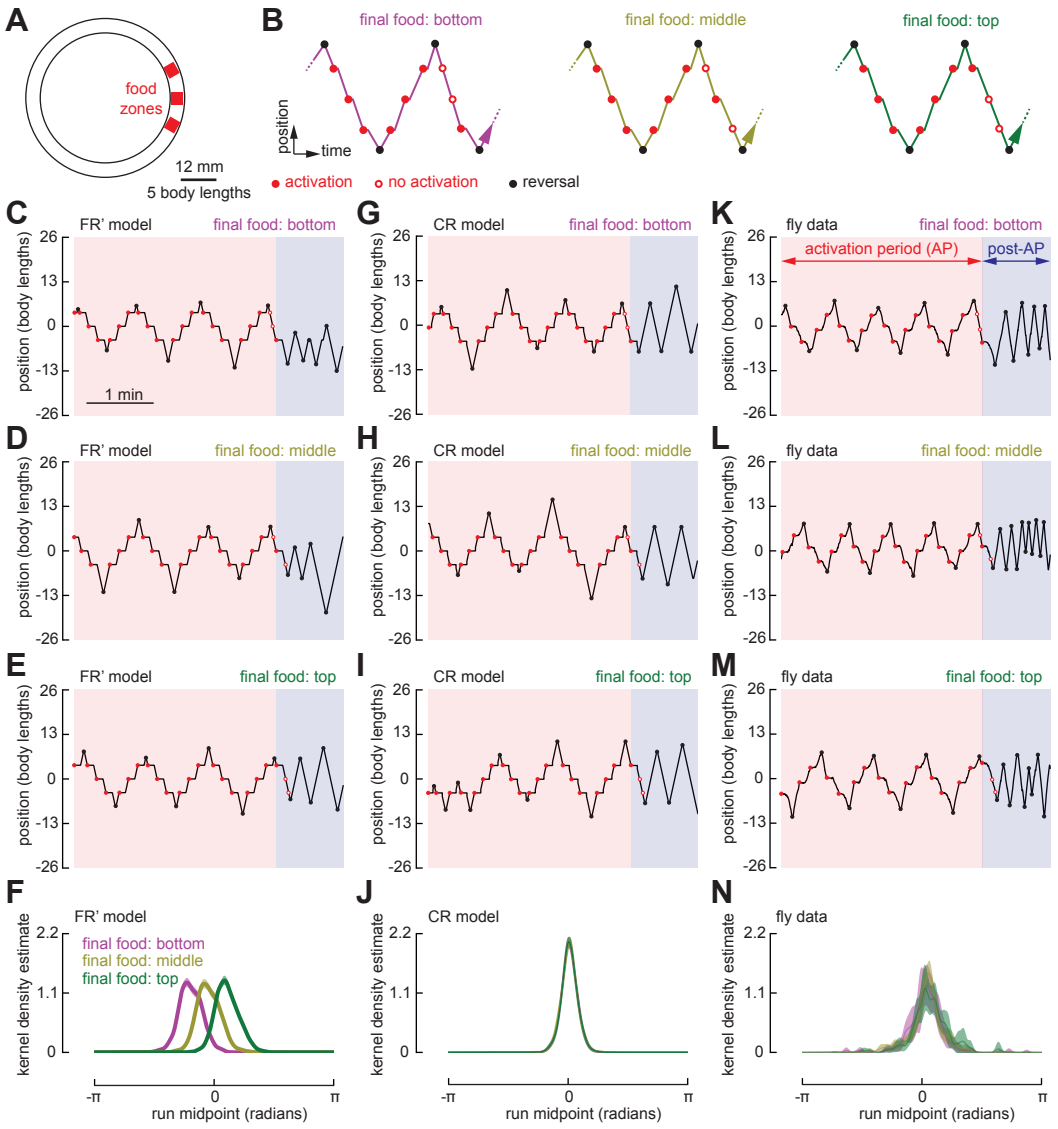

Figure 2.14: Flies reset their path integrator at the center of a cluster of fictive food sites.
(A) Schematic of the annular arena with three food zones, spaced 4.5 body lengths apart.
(B) Schematic of the experimental paradigm. At the conclusion of the AP, two of the food zones were disabled while one food zone remained capable of providing an additional single optogenetic pulse. For each trial, the final operational food zone was designated to be either the bottom, middle, or top. For trials where the final 3 or more runs during the AP spanned all three food zones, we calculated the KDE of the run midpoint during the post-AP.
(C–E) Example trajectories of the FR0 model fly searching across three food zones in which the final food stimulus is in either the bottom (C), middle (D), or top (E) position.
(F) Normalized KDE of the run midpoint in the post-AP period for FR0 model (n = 300 simulations). Shaded regions indicate 95% confidence intervals.
(G–J) As in (C)–(F), for simulations using the CR model (n = 300).
(K–N) As in (C)–(F), for fly data (N = 45 flies, n = 166 trials).

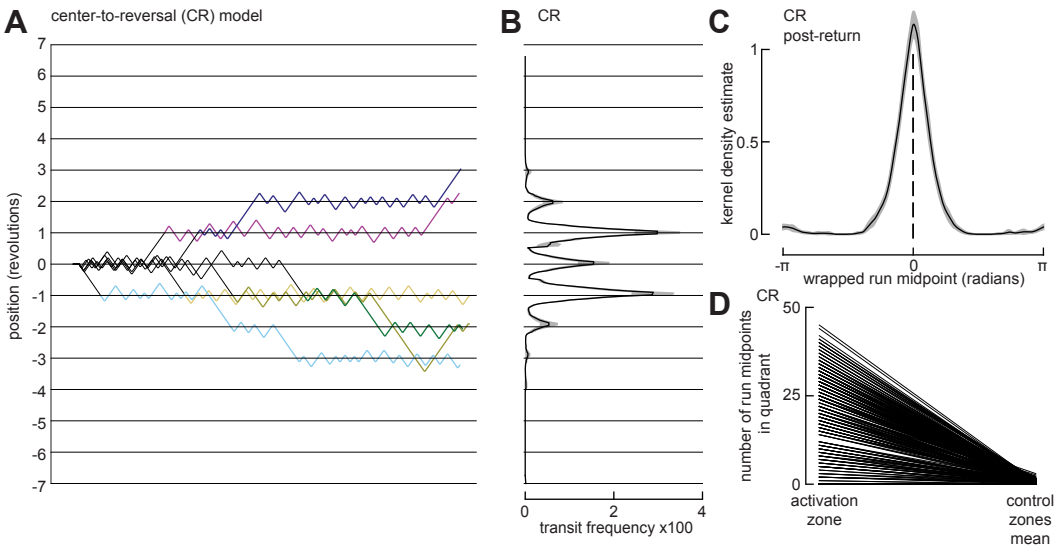

Figure 2.15: The CR model recapitulates fly re-initiation of local search at a former fictive food site after circling the arena.
(A) As in Figure 2.5B, for simulations using the CR model (n = 300).
(B) As in Figure 2.5E, for simulations using the CR model (n = 300).
(C) As in Figure 2.5F, for simulations using the CR model (n = 300).
(D) As in Figure 2.5G, for simulations using the CR model (n = 300).

2.4 Discussion

In this chapter, we developed a novel assay to study path integration during foraging in *Drosophila*, which provides quantitative insight into a behavior that is more difficult to analyze in a simple open field arena. We induced local search in a ring-shaped channel by optogenetically stimulating sugar receptors whenever the fly occupied one or more arbitrarily defined food zones. Local searches in this arena manifested as a persistent zig-zag pattern in which flies iteratively walked away from and back to the food zone (Figures 2.1B and 2.1C)—a pattern that persisted even after the optogenetic stimulation was no longer provided. After the optogenetic activation was disabled, the flies continued to walk back and forth around the site where they had experienced food. Although we cannot directly measure what is going on in the brain of a freely walking animal, we derived a convenient proxy for the flies' spatial memory by constructing a KDE based on the midpoints of the back and forth runs. An examination of the KDE in any given period provides a clear measure of where in the arena a fly was centering its search. In experiments in which the flies were presented with just one food site, this KDE function remained centered at the single food location after the activation protocol was switched off (Figure 2.4D). In experiments in which we presented the fly with two food sites, the peak of the KDE moved to a point midway between two food locations (Figure 2.9B). These data suggest that the flies adjust their integrator such that the zero location is

midway between two food sites, even though there is no sensory stimulus associated with that location. This interpretation is consistent with the agent-based modeling we performed, in that only the CR model, which maintains the zero location of both of the path integrators used to keep track of the simulated fly's position at a location in between food sites, could recapitulate the behaviors we observed (Figures 2.11 and 2.14). This apparent ability to center the idiothetic integrator at a location not directly linked to a sensory stimulus identifies a hitherto unknown capability of the navigation system in Drosophila.

In nearly every fly we examined, individuals did not give up local search gradually, but rather executed what we termed a departure run, which was substantially longer than all previous runs in the post-AP (Figures 2.4A-2.4C). This suggests that the behavioral state of the fly may change over the time course of several minutes after it stops receiving a food stimulus. Nevertheless, in a smaller circular arena, we found that some flies reinitiated a local search at the food site after traveling one or more times around the circumference of the chamber (Figure 2.5), indicating that they retained a spatial memory of the food location and presumably had not changed in physiological state to the point that they had given up their search for the food. Whereas the short back-and-forth motions of the fly around the food site during the AP and post-AP might be explained by simple one-dimensional odometry, the flies' ability to recognize the food site after circling the arena cannot. Such a feat instead requires that flies integrate azimuthal heading information with odometry to perform true two-dimensional path integration. Because our experiments were conducted in the absence of visual or chemical cues, and the results were robust to manipulations such as switching the location of the food stimulus on a trial by trial basis (Figure 2.5), we presume flies measure their translation in the arena via idiothetic self-motion cues, such as proprioception or efference copy of motor commands [17]. The obvious candidate locus for the computations associated with our hypotheses is the central complex (CX), a set of unpaired neuropils in the core of the insect brain [9, 17, 33]. Recently, work on CX neuroanatomy [14, 18] and physiology [15, 20, 36] has characterized a network of neurons that encode compass-heading, leading to models wherein these circuits provide the angular heading information required for path integration. Although mechanisms by which odometric information is encoded and read out by the CX have been proposed [1, 21, 22, 33], none have yet been explicitly tested via genetic or physiological manipulation of behavior.

Our experimental setup in which the flies are restricted to a narrow, dark channel is similar in some regard to the heat box paradigm developed by Wustmann and

colleagues [47]. In that apparatus, flies avoid one half of the chamber that is heated to an aversive temperature and retain the avoidance after the temperature stimulus has been removed. This avoidance has been interpreted to depend on path integration, and clever use of this assay in combination with genetic tools has implicated populations of serotonin cells in the central brain as being critical for place memory [48]. Ofstad and coworkers [26] presented another aversive spatial memory paradigm, based on prior work in cockroaches [24], in which flies learn the position of a cool patch within a hot circular arena using visual cues. Genetic silencing experiments using that paradigm implicated the ellipsoid body (EB) as being critical for place memory. The implication of the EB in this place memory paradigm makes sense in light of more recent work demonstrating the existence of a compass cell network within that structure. The paradigm described in this chapter is different in that the stimulus (optogenetic activation of sugar receptors) that drives the formation of spatial memory is attractive and relies on the behavioral modules employed during foraging behavior rather than those associated with heat avoidance. However, the difference in the representation of attraction and aversion in the CX remains unclear, as does the driving force for resetting the path integrator to a target location. Our assay also provides precise control over the presentation of such stimuli, enabling for the interrogation of the time course of the formation of spatial memory. To systematically test the time course, one might dynamically control the two food sites to see, for example, how many experiences with a second food site are required for the fly to exhibit a two-food search modality in the post-AP. Anecdotally, we observed two-food searches in the post-AP after very few experiences with the second food site or after periods in which the fly has reverted to a one-food search in the AP (Figure 2.10), but a formal analysis of these temporal dynamics was beyond the scope of the current study.

Unlike a prior computational model of path integration by Stone and coworkers [33], our agent-based, state-transition models are not constrained by neural architecture and physiology. However, their output may be directly compared to those of actual experiments, allowing us to probe whether the flies' behavior might require certain cognitive capabilities. Further, the models were not only testable but endowed with predictive power, such that the generation of models satisfying the one food dataset inspired experiments to distinguish between these models. With much effort, we tried to build a model (i.e., our FR' model) that could explain a fly's ability to center its search around a location in the middle of two food sites based only on path integrators that re-zero at the location of food. However, the FR' model

unambiguously failed to predict the results of our three food experiments, which instead indicate that the flies' spatial memory is not determined by the location of the last active food site it encountered (Figures 2.11C and 2.14). As suggested by the success of the CR model, flies appear to accumulate experience while foraging to develop some internal sense of the food patch's center.

Although the CR model successfully recapitulates all aspects of the flies' behavior, its neural implementation is not clear. Performing a search around a central location in a cluster of food sites, as in the two- and three-food experiments, can be explained by at least two mechanisms. First, given the ability of honeybees to count landmarks [13] and trapline across multiple food sites [34], the flies could be treating multiple food sites as individual loci within a larger food patch and adapting their search to cover the entire patch. This mechanism could require that flies have memory of multiple food locations, but a more parsimonious explanation may be that only the central place is stored and each food experience reinforces or updates the place memory of the central location. Alternatively, the food sites could be interpreted as a single food source with high uncertainty in its location; in accordance with optimal foraging strategies, the maximal search radius of the fly would increase with uncertainty as the square root of the time since the last food encounter [6, 23, 38]. This hypothesis is consistent with our observation for the increase in run lengths at the beginning of the post-AP, but not with the plateau seen later in the post-AP (Figure 2.3E). Furthermore, whereas zeroing the path integrators in the models refers to resetting the integrated value to zero, the corresponding biological mechanism is likely more complex. The second mechanism suggested here—that the food sites are interpreted as a single location with high uncertainty—could be explained by an incomplete zeroing of the path integrators upon discovery of the second food site. If memory decay is mediated by, for example, time spent feeding, then residual memory might decay insufficiently to center the search at the new food site and instead cause the fly to search over a central location. Modeling the possibilities separately (as opposed to a general central place model presented here) combined with experiments (e.g., presenting stimuli of differing reward strengths or durations) could help distinguish between these possibilities.

In all the experiments reported in this chapter, we constrained flies to an annular arena, simplifying the complex, tortuous paths of flies performing local search in an unconstrained environment to sequences of runs separated by changes in direction (i.e., reversals). The convenient linearization of the behavior allowed us to focus much of our analyses and modeling on the reversals, events for which there is

no direct equivalent in open field arenas. Even so, reversals likely correspond to behaviors seen in the local searches of unconstrained flies. For example, in an open arena, flies typically walk in straight lines interspersed with discrete changes in direction, which can be as small as a few degrees or as large as 360° [10, 19]. Reversals in the annular arena could correspond to the fly attempting to turn by an angle above a certain threshold. Another possible explanation is that the flies accumulate their changes in direction and reverse course when the accumulated attempted turn angle reaches a threshold. A third possibility is that the reversals are, in fact, unrelated to turn angles in open arenas; rather, the fly executes a reversal when it has reached the maximal distance away from the food site it is willing to venture within the channel.

In sum, we have developed high-throughput assays to quantitatively measure path integration in *Drosophila*, with the ability to quantify spatial memory by measuring the midpoint locations of the runs executed by the animals. The results support the hypothesis that flies employ path integration during foraging behavior, and that they can use this system to center their search at a featureless location situated in between food sites. Future studies might employ these assays, in combination with genetic manipulation of neural activity, to further unravel the neural mechanisms of path integration.

2.5 Methods and materials

Experimental model and subject details

We conducted all experiments using 3-to-6-day-old female *Drosophila melanogaster* reared in darkness at 22°C. We reared the flies on standard cornmeal fly food containing 0.2 mM all trans-Retinal (ATR) (Sigma-Aldrich) and transferred flies 0-2 days after eclosion onto standard cornmeal fly food with 0.4 mM ATR. We supplemented the standard cornmeal food with additional yeast. We obtained the flies by crossing Gr5a-Gal4 male flies with UAS-CsChrimson female virgin flies. Prior to experiments, we wet-starved flies by housing them for 24-40 hours in a vial supplied with a tissue (KimTech, Kimberly-Clark) containing 1 mL of distilled water with 800mM ATR, and dry-starved flies for up to 150 minutes, including a 45-to-90-minute acclimation period in the experimental arena.

Behavioral experiments with walking flies

We conducted all experiments in a 40 mm-diameter annular arena, except for experiments in Figure 2.5, where we used a 20 mm-diameter annular arena to increase the likelihood that flies would complete full revolutions during the post-return period. We constructed the arenas from layers of acrylic with insertable acrylic discs to create the annular channel (4 mm wide and 1.5 mm high). The width of the channel provided sufficient space for flies to walk forward, backward, or turn around at any point in the arena. The channel's low height encouraged the fly to walk either on the floor or the ceiling, rather than the walls of the channel. An upward-directed, custom-made array of 850 nm LEDs, covered by a translucent acrylic panel, was situated 12 cm beneath the arena to provide backlighting for a top-mounted camera (blackfly, FLIR) recording at 30 frames per second. For optogenetic stimulation, we positioned upward directed, 628 nm LEDs (CP41B-RHS, Cree) at the center of each food zone, 8.5 mm beneath the arena floor. We covered the chamber lid with a 3 mm thick long-pass acrylic filter (color 3143, ePlastics). The chamber floor was transparent to allow for optogenetic stimulation, and a filter (#3000 Tough Rolux, Rosco Cinegel) was situated beneath the chamber to diffuse the red light used for stimulation, resulting in $300 W of illumination at the arena floor. The camera, fly chamber, optogenetic lighting panel, and background lighting panel was held within a rigid aluminum frame (80/20) covered with black acrylic to block any external light. We tracked the 2D position of the fly in real time using a python-based machine vision system built on the Robot Operating System (http://florisvb.github.io/multi_tracker). We customized the tracking software to implement closed-loop control of optogenetic

REAGENT or RESOURCE	SOURCE	IDENTIFIER
Chemicals, peptides, and recombinant proteins		
All-trans-retinal	Sigma-Aldrich	CAS: 116-31-4
Deposited data		
Raw and analyzed data	This chapter	https://dx.doi.org/10.17632/tn2fb6hwmp.1
Experimental models: Organisms/strains		
D. melanogaster: Gr5a-GAL4	Gift from J. Carlson [40]	N/A
D. melanogaster: UAS-CsChrimson	Bloomington Drosophila Stock Center	RRID: BDSC_55135
Software and algorithms		
Machine vision tracking software		http://florisvb.github.io/multi_tracker
Data analysis software	This chapter	https://dx.doi.org/10.17632/tn2fb6hwmp.1
Other		
Blackfly camera	FLIR	Part #: BFLY-U3-05S2M-CS
KimTech tissue	Kimberly-Clark	SKU 34155
Cree CP41B-RHS 628 nm LEDs	DigiKey Electronics	Part #: CP41B-RHS-CL0Q0EE4-ND
1/16" Clear acrylic sheet	McMaster-Carr	Part #: 8560K174
1/8" Clear acrylic sheet	McMaster-Carr	Part #: 8560K259
1/8" Black acrylic sheet	McMaster-Carr	Part #: 8505K744
3143 Infrared transmitting acrylic sheet	ePlastics	SKU: ACRY31430.125PM24X48
Rosco Cinegel #3000 Filter	B&H Photo	Part #: RO3000R48
LED controller	Arduino	Nano, Product Code: A000005
850 nm LED strip (infrared lighting)	LED Lights World	Part #: 5M-HK-8MM-F3528-850-30-NW-IR-12
SRI6PF Incubator	Shellab	Part #: SR16PF
Aluminum for construction	80/20	Part #: 25-2525

Table 2.1: Key Resources Table for Chapter II

stimulation via an LED controller (Arduino Nano). During our initial experiments, we cleaned the behavioral chamber with 100% ethanol after each trial and allowed it to dry before reuse. However, because ethanol causes cracks in the acrylic parts, we stopped using ethanol and instead cleaned the chambers with compressed air. We did not observe any difference in fly behavior between the two cleaning methods (data not shown).

For each experiment, we aspirated a single fly into the behavioral chamber, allowing it to acclimate for 45-90 minutes. The final minutes of this acclimation period correspond to the baseline period in our analyses. Following acclimation, experiments consisted of a specified time-course of activation periods (APs) and post activation-periods (post-APs). During APs, the LED beneath each food zone was turned on for 1 s whenever the centroid of the fly occupied its virtual perimeter (= 2.6 BL or 1.3 BL for the small arena experiment in Figure 2.5). Because optogenetic activation of sugar sensors inhibits locomotion [10], each 1 s pulse was followed by a 15 s refractory period during which the LED remained off, regardless of the fly's position. During the baseline period and post-APs, food zones were not operational, such that flies could not receive optogenetic activation.

For experiments with multiple APs (as in Figure 2.1C), each AP and subsequent post-AP was treated as a single trial. For all experiments with a 40-min AP (e.g., 2.1B), data were discarded if the fly moved less than 10 cumulative body lengths during the first 20 minutes of the AP (n = 3 flies discarded). For all trial-based experiments (e.g., 2.1C), trials were discarded if the fly moved less than 10 cumulative body lengths during the AP (n = 22 trials discarded).

For experiments in Figure 2.5, to discard the possibility that flies were able to find food zones by sensing temperature gradients generated by the LEDs, one of the control zones was outfitted with an LED. When food stimuli were presented, the LEDs at both food zones as well as this control zone were turned on.

During experiments in Figure 2.14, we encouraged flies to expand their search to span all three food zones by using an altered protocol during the AP in which we disabled each food zone after it was encountered by the fly for the first time; after the fly had encountered all three food zones, all the food zones became operational and remained operational for the remainder of the AP.

Agent-based models without odometric integration

The random sampling and Lévy flight models simulated post-AP search by drawing from natural statistics derived from fly search trajectories. For the random sampling

model, run lengths were randomly sampled with replacement from the fly post-AP run lengths in Figure 2.4A (excluding the departure run). For the Lévy flight model, a Lévy distribution was fit to the same data using the function stats.levy.fit() from SciPy, and run lengths were drawn randomly from the resulting distribution.

Agent-based models featuring odometric integration

The food-to-reversal (FR), food-to-reversal' (FR'), and center-to-reversal (CR) integration models are graphically described by the state transition diagrams in Figures 2.8, 2.12, and 2.13. The fly is simulated as a point-mass within a virtual environment (Figure 2.8A) consisting of an annular channel, 52 body lengths (BL) in circumference. The environment includes one or more food zones (1 BL in length) at specified locations along the linear channel. Similar to our experiments with real flies, whenever the simulated fly enters a food zone in the simulated environment, it receives a 1 s food stimulus, followed by an 8 s refractory period during which the simulated fly cannot receive a food stimulus; whereas the refractory period is briefer in the simulations than in experiments with real flies, comparisons of temporal aspects of the two systems are somewhat arbitrary because the walking speed of simulated flies is defined artificially. When walking, the fly moves 1 BL per time step, corresponding to 0.5 s (i.e., the simulated fly walks at 2 BL s^{-1}).

The fly is initialized at the 0 BL position, in the counterclockwise orientation, and the simulated environment (Figure 2.8A) is initialized in the food-off state. The fly's integrators are initialized with a value of 0 and the fly's target run length value, r_t, is initialized to 0. When the environment is in the food-off state, at each time step, the system checks whether the current time is during the AP, whether the current time is not during a refractory period (i.e., whether the time since the last food stimulus exceeds the duration of the refractory period), and whether the fly occupies a food zone; if all of these conditions are satisfied, the food stimulus is turned on and the environment enters the food-on state. When the environment is in the food-on state, at each time step, if the food stimulus has been on for the duration of the specified stimulus duration (1 time step), the food stimulus is turned off and the environment returns to the food-off state. The state transition diagram described in Figure 2.8A—with varying food zone positions as well as varying baseline, AP, and post-AP durations—is used to simulate the environment in all the models (FR, FR', and CR).

Food-to-reversal integration model

In the food-to-reversal (FR) model (Figure 2.8B), the simulated fly is able to measure walking distance using two integrators—one integrator measuring displacement along the North-South axis, I_{NS}, and a second measuring displacement along the East-West axis, I_{EW}. These directions are defined within the simulated fly's reference frame, rather than a global reference frame in the simulated environment; that is, while the environment imposes a global reference frame, the simulated fly constructs its own map of space agnostic to the absolute directions an observer may impose (e.g., the simulated fly may assign North to the direction an observer would call West). The simulated fly is able to store and retrieve its previous action—either a reversal or an eating event. The simulated fly is initialized in the global search mode in the walking state, where it moves forward 1 BL at every time step. When the fly receives a food stimulus, it transitions to the eating state in the local search mode. The fly remains in the local search mode for the remainder of the simulation. While the fly continues to receive the food stimulus, it remains in the eating state. Upon delivery of a food stimulus, the simulation is advanced 10 time steps, during which the fly remains stationary, which mimics the locomotory pause induced by activation of sugar-sensing neurons in *Drosophila*. While flies exhibit more complex behaviors when walking in the absence of food stimuli (e.g., pausing, changes in walking speed) and in response to food stimuli (e.g., proboscis extension), the models aimed to reduce the behavior to its simplest form to exclusively interrogate the bounds of integration, so these more complex modalities were ignored.

Upon the termination of the food stimulus in the FR model, the fly selects a new target run length, r_t, by drawing a value from C_f, the distribution of food-induced run lengths. As described in a subsequent section, it is not possible to directly observe C_f in data from real flies, and we therefore derived this distribution via an optimization procedure that fits our model to data. Upon termination of the food stimulus in the FR model, the integrators are both set to zero, such that the food site serves as the origin of the fly's search. This behavior is in accordance with traditional PI models, wherein the integrators are zeroed at the origin of search and a maximal excursion distance is selected.

Having responded to the food stimulus, the simulated fly sets its previous action to an eating event and transitions to a walking state. At each time step while in the walking state, the fly moves forward 1 BL and the integrators are incremented by decomposing the step into orthogonal components along the North-South and East-West axes using trigonometric functions of the fly's heading direction, θ_h. The

fly receives its heading direction from the environment at every time step rather than including a mechanism in the model for the fly to determine its heading based on idiothetic or allothetic cues.

The fly recalls whether a full revolution has been made since last passing the food site to reinitiate the search after full revolutions. In these cases, a run length has been selected which exceeds the maximum possible integrator value when the fly is constrained to the circle, so the fly will never perform a reversal and, in the post-AP, never select a new run length. When the absolute value of the heading angle exceeds 3 rad (172°), the fly recognizes that a full revolution has occurred. Alternatively, if the absolute value of the heading angle falls below 0.15 rad (8.6°) and a full revolution has occurred, the fly has returned to the food site and, accordingly, chooses a new run length, zeroes its integrators, and sets the full revolutions variable to False. In essence, this feature of the model enables the simulated fly to recognize its return to the food site despite not having made a reversal, choose a new run length, and resume search accordingly.

The fly continues walking until the Euclidean norm of the integrators equals or exceeds its current target run length, r_t. At this point, a new target run length is selected based on the fly's previous action. If the previous action was an eating event, r_t is defined to be the sum of the value of the Euclidean norm of the integrators and a value drawn from C_f; this ensures that the search stays centered over the food zone. On the other hand, if the previous action was a reversal, r_t is defined to be the sum of the Euclidean norm of the integrators and a value drawn from C_Δ, the distribution of the differences in lengths between consecutive runs. As described in a subsequent section, we determine C_Δ via an optimization procedure that fits our model to data from real flies. After the selection of a new target run length, walking direction is reversed and the integrators are zeroed. The fly remains in the walking state and returns to the eating state if it receives a food stimulus. This is in accordance with traditional path integration models, wherein the agent only searches within a certain distance from the origin; constrained to a one-dimensional environment, the agent executes a reversal when this limit is reached.

Food-to-reversal' integration model

In the food-to-reversal' (FR') model (Figure 2.12), the simulated fly measures walking distance using four integrators—one integrator for displacement in each direction: North, South, East, and West (I_N, I_S, I_E, and I_W, respectively). The FR' model would not function with only two orthogonal integrators because the

simulated fly must keep track of two distances to accomplish local search during the post-AP in environments with multiple foods: the distance between the foods and the distance walked since the last reversal. In a two-food configuration, for example, immediately preceding a reversal, the integrators in the previous direction of travel will store the distance to the further food site and the opposing integrators will both be zero. After the reversal, the integrators storing the distance to food will begin to decrement and the others will increment. Upon encountering the closest food site, the first set of integrators will then exactly equal the distance between the food sites, whereas the second set of integrators will recall the distance from the reversal to the current location. Thus, the model measures the distance from the reversal, as did the FR model, while still recalling the distance between food sites in multiple food configurations. Like the FR model, however, feeding sites remain the locations where all integrators re-zero, but with differences described more fully below.

Upon the termination of the food stimulus in the FR' model, the fly selects a new target run length, r_t, based on the fly's most recent previous action. If the fly's most recent action was a reversal, then r_t is defined to be the sum of I_o, a value computed as the Euclidean norm of the two integrators opposing the current direction of travel, and a value drawn from C_f, all integrators are set to zero, and θ_h^*, the food site heading angle, is set to the current heading angle. This course of action represents the fly responding to having received its first food stimulus since performing a reversal; in the FR' model, the first food stimulus after a reversal is treated as the origin of search, so the integrators are zeroed and a run length is selected accordingly. Similarly, if the most recent action was a full revolution, r_t is a value drawn from C_f, the integrators are zeroed, and the food site heading angle is set to the current heading angle; this course of action represents the fly encountering a food site after performing a full revolution around the circle. On the other hand, if the fly's most recent action was an eating event (the only possible action other than a reversal or a full revolution) and the difference between the current target run length and the value of I_d, a value computed as the Euclidean norm of the two integrators aligned with the current direction of travel, is below 1 BL, then the new target run length, r_t, is defined to be the sum of the value of whichever integrator is highest and a value drawn from C_f; this course of action represents the simulated fly interpreting the food stimulus as a new food location and extending its run length to expand its local search to encompass the new food in addition to the prior food(s). Finally, if none of the conditions holds, the fly does not select a new target run length; this course of action represents the fly encountering a food site that has been previously

experienced and which the search has already been expanded to encompass. In sum, the fly sets the first food site after a reversal as the origin of its search, does not change the origin in response to additional food sites on that run, and only extends the run length if a previously unexperienced food site is encountered.

Having responded to the food stimulus, the simulated fly sets its previous action to an eating event and transitions to a walking state. At each time step while in the walking state, the fly moves forward 1 BL and the integrators are incremented accordingly with a minimum value of zero. The mechanism for identifying and responding to full revolutions is similar to that of the FR model; here, however, the fly uses the difference between the heading angle and the food site heading angle such that a full revolution is only identified when the fly's position diametrically opposes the position of the food site.

As in the FR model, the fly executes a reversal when it reaches the target run length, the maximal distance from the origin of search it is willing to venture. Algorithmically, this distance is identified as I_d equaling or exceeding r_t. At this point, a new target run length, r_t, is selected based on the fly's previous action. If the previous action was an eating event, r_t is defined to be the sum of the value of I_d and a value drawn from C_f; this ensures that the search stays centered over the food zone(s). On the other hand, if the previous action was a reversal, r_t is defined to be the sum of I_d and a value drawn from C_Δ. After the selection of a new target run length, walking direction is reversed. As the integrators are strictly positive, the integrators in the direction of travel following a reversal are always zero, so a formal zeroing step is not required. The fly remains in the walking state and returns to the eating state if it receives a food stimulus.

Center-to-reversal integration model

In the center-to-reversal (CR) model (Figure 2.12), the simulated fly is able to measure walking distance using just two integrators, I_{NS} and I_{EW}. Furthermore, the simulated fly is able to store and retrieve its previous action—either a reversal or an eating event. As in the FR and FR' models, the fly is initialized in the global search mode in the walking state and transitions to the local search mode, eating state upon receiving a food stimulus. The fly remains in the local search mode for the remainder of the simulation.

After receiving a food stimulus, the fly stays in the eating state until the termination of the food stimulus, at which time it transitions to the walking state. If the fly's previous action was eating, a new run length is selected as the sum of a value drawn

from C_f and ϵ, a term that represents its rough estimate of the expanse of the food region encompassing multiple food sites. If the Euclidean norm of the integrators exceeds ϵ, the fly recognizes that it has encountered a new food site and adjusts its integrators such that the origin of its search is at the center of mass of the food sites. Additionally, ϵ is adjusted to exceed the distance from the center of mass to the outermost food site. To accomplish this, it increments N, the total number of food sites present, by one, and updates the integrators and origin heading angle by multiplying them by a factor of $1 - \frac{1}{N}$. This effectively shifts the center of mass by the current integrator value along its axis divided by the number of food sites, such that the center location is always the average location of all known food sites. The expanse, ϵ, is also updated by multiplication of the Euclidean norm of the integrators by the same factor, and a further multiplication by 1.5 to ensure the expanse encompasses all food sites regardless of numerical errors.

Having responded to the food stimulus, the simulated fly sets its previous action to an eating event and transitions to the walking state. While walking, the integrators are incremented via orthogonal components of the step length as in the FR model. When the Euclidean norm of the integrators falls below one, a new target run length is selected such that if the fly performs a full revolution, it reinitiates the search at the center of the food site.

As in the previous models, when the Euclidean norm of the integrators exceeds the target run length, the fly performs a reversal. The new target run length is defined to be the sum of the expanse and a value drawn from C_f, the direction is reversed, and the fly returns to the walking state. The fly remains in the walking state and returns to the eating state if it receives a food stimulus.

Run length distributions for odometric integration models

In all three models, the simulated fly selects a new target run length following a food stimulus by sampling from the food-induced run length distribution $C_f \sim \mathcal{N}(\mu_f, \sigma_f$. To select a new target run length following a reversal, the FR and FR' models sample from $C_\Delta \sim \mathcal{N}(\mu_\Delta, \sigma_\Delta$—the distribution of the difference in length between consecutive runs—whereas the CR model always draws from C_f when selecting a new run length, regardless of previous actions. Whereas the sampled distributions are analogous to the observable statistics of *Drosophila* local search, they cannot be derived from fly data, because we cannot directly measure target run length in a real fly. For example, when a fly encounters a new food location and continues walking several body lengths before performing a reversal, the resulting total run length

might be the sum of the original target run length (selected prior to encountering the new food) and an additional run length induced by the new food stimulus; therefore, we cannot directly measure the true value of either component of the fly's algorithm. Instead, we determined the distribution parameters by performing a grid search over the parameter space to minimize a cost function (Equation 2.1). At each point in the grid search, the model was run 250 times in the one food configuration. The cost function was designed to minimize the differences between the statistics of *Drosophila* local search and those of the given model. Given N parameters we sought to match between the data and simulations, we fit an appropriate distribution (e.g., inverse Gaussian) to the i^{th} parameter to get the distribution $p_i \sim X_i(x_{i,1}, x_{i,2}, \ldots, x_{i_M})$, such that the distribution is governed by M_i values. We fit the distribution to both the data and the simulations, yielding $p_i^d \sim X_i(x_{i,1}^d, x_{i,2}^d, \ldots, x_{i_M}^d)$ for the data and $p_i^s \sim X_i(x_{i,1}^s, x_{i,2}^s, \ldots, x_{i_M}^s)$ for the simulations (where d and s denote 'desired' and 'simulated', respectively). We then calculated the total cost across all parameters, normalizing for the number of values governing each distribution:

$$\text{Cost} = \sum_{i=1}^{N} \frac{1}{M_i} \sum_{j=1}^{M_i} \left(\frac{x_j^s}{x_j^d} - 1 \right)^2. \tag{2.1}$$

The relevant parameters we sought to match between the data and simulations were the excursion distances ($D_O^d \sim \text{IG}(\mu = 0.282, \text{loc} = -0.675, \text{scale} = 21.9)$), the run lengths in the post-AP ($r_{N,\text{post-AP}}^d \sim \text{IG}(\mu = 0.543, \text{loc} = -0.672, \text{scale} = 33.5)$), and the location of run midpoints ($M_{\text{ap}}^d \sim \text{IG}(\mu = 0.910, \text{loc} = -0.211, \text{scale} = 1.79)$ and $M_{\text{post-AP}}^d \sim \text{IG}(\mu = 1.32, \text{loc} = -0.368, \text{scale} = 2.98)$). These values were derived using SciPy's stats.invgauss.fit() function. The distributions used in the FR model were $C_f \sim \mathcal{N}(\mu_f = 4.125, \sigma_f = 2.626)$ and $C_\Delta \sim \mathcal{N}(\mu_\Delta = 0.03125, \sigma_\Delta = 1.875)$. The distributions used in the FR' model were $C_f \sim \mathcal{N}(\mu_f = 2., \sigma_f = 2.25)$ and $C_\Delta \sim \mathcal{N}(\mu_\Delta = -0.1875, \sigma_\Delta = 2.5)$. The distributions used in the CR model were $C_f \sim \mathcal{N}(\mu_f = 1.75, \sigma_f = 3.)$. The final cost for the FR model was ~ 76.1, the final cost for the FR' model was 2.14, and the final cost for the CR model was 3.06.

Behavioral analysis of walking flies

The dataset for each experiment consisted of an array of X and Y coordinates representing the 2D positions of the fly, as well as an array of LED states (on or off) for each food zone. Data were sampled at ~30 Hz. We converted the positional coordinate of the fly to an angular position in the ring-shaped arena and treated the fly as a point mass along the circumference of the arena. The beginning of

each AP was defined as the first food stimulus, and the end of each AP (and the beginning of the subsequent post-AP) was defined as the final food stimulus. To process data, we discarded occasional frames where the fly was either not tracked, where a second object was tracked in addition to the fly (e.g., fly poop), or where the tracked position jumped more than 3 mm within two consecutive frames (e.g., due to sporadic tracking of another object). Because the position of food zones varied slightly due to variations in the fabrication and assembly of arenas, we defined the center of each food zone for each experiment as the midpoint between the extrema of fly locations at food stimulus events associated with the food zone.

Quantification and statistical analysis

We generated all figures using the python library matplotlib. Throughout the chapter, we calculated the 95% confidence intervals using built-in SciPy statistical functions to compute the standard error of the mean and the Student's t-distribution. For the statistical significance analysis, we used distributions of mean values generated by 2000 bootstrap iterations.

Bibliography

[1] Andrea Adden, Terrence C. Stewart, Barbara Webb, and Stanley Heinze. A neural model for insect steering applied to olfaction and path integration. *Neural Computation*, 34(11):2205–2231, 2022.

[2] Gal Aharon, Meshi Sadot, and Yossi Yovel. Bats use path integration rather than acoustic flow to assess flight distance along flyways. *Current Biology*, 27 (23):3650–3657, 2017.

[3] Claudine Badue, Rânik Guidolini, Raphael Vivacqua Carneiro, Pedro Azevedo, Vinicius B. Cardoso, Avelino Forechi, Luan Jesus, Rodrigo Berriel, Thiago M. Paixao, Filipe Mutz, et al. Self-driving cars: A survey. *Expert Systems with Applications*, 165:113816, 2021.

[4] William J. Bell, Tortorici Cathy, Ricardo J. Roggero, Larry R. Kipp, and Thomas R. Tobin. Sucrose-stimulated searching behaviour of Drosophila melanogaster in a uniform habitat: Modulation by period of deprivation. *Animal Behaviour*, 33(2):436–448, 1985.

[5] Cornelia Bühlmann, Ken Cheng, and Rüdiger Wehner. Vector-based and landmark-guided navigation in desert ants inhabiting landmark-free and landmark-rich environments. *Journal of Experimental Biology*, 214(17):2845–2853, 2011.

[6] A. Cheung. Animal path integration: A model of positional uncertainty along tortuous paths. *Journal of Theoretical Biology*, 341:17–33, 2014.

[7] Matthew Collett and Thomas S. Collett. How do insects use path integration for their navigation? *Biological cybernetics*, 83(3):245–259, 2000.

[8] Matthew Collett, Thomas S. Collett, and Rüdiger Wehner. Calibration of vector navigation in desert ants. *Current Biology*, 9(18):1031–S1, 1999.

[9] Thomas S. Collett. Path integration: How details of the honeybee waggle dance and the foraging strategies of desert ants might help in understanding its mechanisms. *Journal of Experimental Biology*, 222(11):jeb205187, 2019.

[10] Román A. Corfas, Tarun Sharma, and Michael H. Dickinson. Diverse food-sensing neurons trigger idiothetic local search in Drosophila. *Current Biology*, 29(10):1660–1668, 2019.

[11] Charles Darwin. Origin of certain instincts. *Nature*, 7:417–418, 1873.

[12] Vincent G. Dethier. Communication by insects: physiology of dancing. *Science*, 125(3243):331–336, 1957.

[13] C. Evangelista, P. Kraft, Marie Dacke, T. Labhart, and M.V. Srinivasan. Honeybee navigation: Critically examining the role of the polarization compass. *Philosophical Transactions of the Royal Society B: Biological Sciences*, 369 (1636):20130037, 2014.

[14] Romain Franconville, Celia Beron, and Vivek Jayaraman. Building a functional connectome of the Drosophila central complex. *Elife*, 7, 2018.

[15] Jonathan Green, Atsuko Adachi, Kunal K. Shah, Jonathan D. Hirokawa, Pablo S. Magani, and Gaby Maimon. A neural circuit architecture for angular integration in Drosophila. *Nature*, 546(7656):101–106, 2017.

[16] Rânik Guidolini, Lucas G. Scart, Luan F.R. Jesus, Vinicius B. Cardoso, Claudine Badue, and Thiago Oliveira-Santos. Handling pedestrians in crosswalks using deep neural networks in the IARA autonomous car. In *2018 International Joint Conference on Neural Networks (IJCNN)*, pages 1–8. IEEE, 2018.

[17] Stanley Heinze, Ajay Narendra, and Allen Cheung. Principles of insect path integration. *Current Biology*, 28(17):R1043–R1058, 2018.

[18] Brad K. Hulse, Hannah Haberkern, Romain Franconville, Daniel B. Turner-Evans, Shinya Takemura, Tanya Wolff, Marcella Noorman, Marisa Dreher, Chuntao Dan, Ruchi Parekh, et al. A connectome of the Drosophila central complex reveals network motifs suitable for flexible navigation and context-dependent action selection. *Biorxiv*, pages 2020–12, 2021.

[19] Irene S. Kim and Michael H. Dickinson. Idiothetic path integration in the fruit fly Drosophila melanogaster. *Current Biology*, 27(15):2227–2238, 2017.

[20] Sung Soo Kim, Hervé Rouault, Shaul Druckmann, and Vivek Jayaraman. Ring attractor dynamics in the Drosophila central brain. *Science*, 356(6340): 849–853, 2017.

[21] Jenny Lu, Amir H. Behbahani, Lydia Hamburg, Elena A. Westeinde, Paul M. Dawson, Cheng Lyu, Gaby Maimon, Michael H. Dickinson, Shaul Druckmann, and Rachel I. Wilson. Transforming representations of movement from body-to-world-centric space. *Nature*, 601(7891):98–104, 2022.

[22] C. Lyu, L.F. Abbott, and G. Maimon. A neuronal circuit for vector computation builds an allocentric traveling-direction signal in the *Drosophila* fan-shaped body. *bioRxiv*, 2020.

[23] Tobias Merkle, Markus Knaden, and Rüdiger Wehner. Uncertainty about nest position influences systematic search strategies in desert ants. *Journal of Experimental Biology*, 209(18):3545–3549, 2006.

[24] Makoto Mizunami, Josette M. Weibrecht, and Nicholas J. Strausfeld. Mushroom bodies of the cockroach: their participation in place memory. *Journal of Comparative Neurology*, 402(4):520–537, 1998.

[25] Martin Müller and Rüdiger Wehner. Path integration in desert ants, Cataglyphis fortis. *Proceedings of the National Academy of Sciences*, 85(14):5287–5290, 1988.

[26] Tyler A. Ofstad, Charles S. Zuker, and Michael B. Reiser. Visual place learning in Drosophila melanogaster. *Nature*, 474(7350):204–207, 2011.

[27] Rickesh N. Patel and Thomas W. Cronin. Mantis shrimp navigate home using celestial and idiothetic path integration. *Current Biology*, 30(11):1981–1987, 2020.

[28] Lucas C. Possatti, Rânik Guidolini, Vinicius B. Cardoso, Rodrigo F. Berriel, Thiago M. Paixão, Claudine Badue, Alberto F. De Souza, and Thiago Oliveira-Santos. Traffic light recognition using deep learning and prior maps for autonomous cars. In *2019 international Joint Conference on Neural Networks (IJCNN)*, pages 1–8. IEEE, 2019.

[29] G.H. Pyke. Optimal foraging theory. *Annual Review of Ecology and Systematics*, 15:523–575, 1984.

[30] Bernhard Ronacher. Path integration as the basic navigation mechanism of the desert ant Cataglyphis fortis (Forel, 1902) (Hymenoptera: Formicidae). *Myrmecological News*, 11:53–62, 2008.

[31] Paul Schmid-Hempel. Individually different foraging methods in the desert ant Cataglyphis bicolor (hymenoptera, formicidae). *Behavioral Ecology and Sociobiology*, 14(4):263–271, 1984.

[32] Valerie Séguinot, Jennifer Cattet, and Simon Benhamou. Path integration in dogs. *Animal Behaviour*, 55(4):787–797, 1998.

[33] Thomas Stone, Barbara Webb, Andrea Adden, Nicolai Ben Weddig, Anna Honkanen, Rachel Templin, William Wcislo, Luca Scimeca, Eric Warrant, and Stanley Heinze. An anatomically constrained model for path integration in the bee brain. *Current Biology*, 27(20):3069–3085, 2017.

[34] J.D. Thomson, S.C. Peterson, and L.D. Harder. Response of traplining bumble bees to competition experiments: Shifts in feeding location and efficiency. *Oecologia*, 71(2):295–300, 1987.

[35] Charles Henry Turner. *The homing of ants: An experimental study of ant behavior*. University of Chicago., 1907.

[36] Daniel Turner-Evans, Stephanie Wegener, Herve Rouault, Romain Franconville, Tanya Wolff, Johannes D. Seelig, Shaul Druckmann, and Vivek Jayaraman. Angular velocity integration in a fly heading circuit. *Elife*, 6: e23496, 2017.

[37] R. Wehner and M. Müller. The significance of direct sunlight and polarized skylight in the ant's celestial system of navigation. *Proceedings of the National Academy of Sciences*, 103:12575–12579, 2006.

[38] Rüdiger Wehner and Mandyam V. Srinivasan. Searching behaviour of desert ants, genus Cataglyphis (Formicidae, Hymenoptera). *Journal of Comparative Physiology*, 142(3):315–338, 1981.

[39] Rüdiger Wehner and Sibylle Wehner. Path integration in desert ants. Approaching a long-standing puzzle in insect navigation. *Monitore Zoologico Italiano-Italian Journal of Zoology*, 20(3):309–331, 1986.

[40] L.A. Weiss, A. Dahanukar, J.Y. Kwon, D. Banerjee, and J.R. Carlson. The molecular and cellular basis of bitter taste in *Drosophila*. *Neuron*, 69:258–272, 2011.

[41] Ian Q. Whishaw. Place learning in hippocampal rats and the path integration hypothesis. *Neuroscience & Biobehavioral Reviews*, 22(2):209–220, 1998.

[42] I.Q. Whishaw and B.L. Brooks. Calibrating space: Exploration is important for allothetic and idiothetic navigation. *Hippocampus*, 9:659—-667, 1999.

[43] Matthias Wittlinger, Rüdiger Wehner, and Harald Wolf. The ant odometer: Stepping on stilts and stumps. *Science*, 312(5782):1965–1967, 2006.

[44] Matthias Wittlinger, Rudiger Wehner, and Harald Wolf. The desert ant odometer: A stride integrator that accounts for stride length and walking speed. *Journal of Experimental Biology*, 210(2):198–207, 2007.

[45] H. Wolf. Odometry and insect navigation. *Journal of Experimental Biology*, 214:1629–1641, 2011.

[46] Harald Wolf and Rüdiger Wehner. Pinpointing food sources: Olfactory and anemotactic orientation in desert ants, Cataglyphis fortis. *Journal of Experimental Biology*, 203(5):857–868, 2000.

[47] G. Wustmann, K. Rein, R. Wolf, and M. Heisenberg. A new paradigm for operant conditioning of Drosophila melanogaster. *Journal of Comparative Physiology A*, 179(3):429–436, 1996.

[48] Troy Zars. Spatial orientation in Drosophila. *Journal of Neurogenetics*, 23 (1-2):104–110, 2009.

Chapter 3

A POPULATION OF DESCENDING NEURONS REQUIRED FOR THE OPTOMOTOR RESPONSE IN FLYING *DROSOPHILA*

Emily H. Palmer, Jaison J. Omoto, and Michael H. Dickinson. The role of a population of descending neurons in the optomotor response in flying *Drosophila*. *bioRxiv*, 2022. doi: https://doi.org/10.1101/2022.12.05.519224.
E.H.P. and J.J.O performed all experiments under the supervision of M.H.D. E.H.P. developed the computational models. E.H.P. and J.J.O. analyzed data and prepared all figures. E.H.P., J.J.O., and M.H.D. wrote the paper.

3.1 Abstract

To maintain stable flight, animals continuously perform trimming adjustments to compensate for internal and external perturbations. Whereas animals use many different sensory modalities to detect such perturbations, insects rely extensively on optic flow to modify their motor output and remain on course. We studied this behavior in the fruit fly, *Drosophila melanogaster*, by exploiting the optomotor response, a robust reflex in which an animal steers so as to minimize the magnitude of rotatory optic flow it perceives. Whereas the behavioral and algorithmic structure of the optomotor response has been studied in great detail, its neural implementation is not well-understood. In this chapter, we present findings implicating a group of nearly homomorphic descending neurons, the DNg02s, as a core component for the optomotor response in flying *Drosophila*. Prior work on these cells suggested that they regulate the mechanical power to the flight system, presumably via connections to asynchronous flight motor neurons in the ventral nerve cord. When we chronically inactivated these cells, we observed that the magnitude of the optomotor response was diminished in proportion to the number of cells silenced, suggesting that the cells also regulate bilaterally asymmetric steering responses via population coding. During an optomotor response, flies coordinate changes in wing motion with movements of their head, abdomen, and hind legs, which are also diminished when the DNg02 cells are silenced. Using two-photon functional imaging, we show that the DNg02 cells respond most strongly to patterns of horizontal motion and that neuronal activity is closely correlated to motor output.

3.2 Introduction

As flying animals navigate through space, they must constantly integrate sensory information to ensure they maintain stable flight along their desired trajectory. Studies on the behavioral algorithms that flying insects use to adjust for internal and external perturbations have demonstrated their ability to maintain constant groundspeed in the face of variable wind speed [6, 21, 24], reject applied body rotations [2, 33, 40], and sustain flight despite having extensive wing damage [28]. Much recent research on flight control has focused on the fruit fly *Drosophila melanogaster* due to its robust behavior in tethered flight arenas [15] and the vast array of genetic tools available in this species [36]. Collectively, these efforts provide a broad overview on the basic algorithmic structures of insect flight control systems [8].

To study flight stabilization, researchers often exploit the optomotor response, a well-characterized behavior in which a fly reflexively steers so as to minimize the optic flow it perceives. The optomotor response is typically quantified by measuring either the yaw torque generated by the wings [16] or the bilateral difference of the wingbeat amplitude [18], which is strongly correlated with torque [38]. This simple psychophysical paradigm has enabled the investigation of how the fly's motor response varies with a large set of input parameters, including the spatiotemporal structure of the optomotor stimulus [9, 38], mechanosensory cues from wind [4, 14, 26], or imposed body rotations [7, 12]. Studies on the *Drosophila* visual system have provided insight into the computations used to translate information from photoreceptors in the retina to the lobula plate tangential cells (LPTCs), neurons that are likely relevant to flight stabilization because they encode different patterns of wide-field optic flow [13, 19, 22, 35], but the neuronal circuits downstream of the LPTCs to the motor systems have remained largely elusive. A detailed description of the mechanical response and muscle systems underlying the response follow in Chapter 4.

Whereas the optomotor response has been studied in great detail at the behavioral level, the details of the sensory-motor pathways that underlie it remain largely unknown, especially the means by which wide-field visual motion is conducted to the motor centers in the ventral nerve cord (VNC). Recent work morphologically classifying a large fraction of the descending neurons (DNs) provides a useful starting point for investigating how sensory information from the brain is transformed into motor commands in the VNC [29]. Building from this, Namiki and colleagues [30] performed an optogenetic activation screen on a set of driver lines selectively

targeting different DNs and identified a class of nearly homomorphic neurons, the DNg02s, as a candidate for encoding commands relevant to flight control. Unlike many identified DNs, which exist as single bilateral pairs of the cells with stereotyped morphology, the DNg02 cells constitute a large set of nearly homomorphic cells. The potential role of the DNg02 cells in flight control was identified via optogenetic activation of the neurons in tethered flying animals, using a collection of driver lines that targets different numbers of DNg02 cells. The change in bilateral stroke amplitude elicited by the optogenetic stimulus was linearly correlated with the number of cells activated, suggesting that the fly might employ the DNg02s in a population code to regulate wingbeat amplitude and total mechanical power over a large operating range. One hypothesis for the large number of DNg02 cells is that they collectively provide both the dynamic range and the motor precision that is required for flight control. Whereas the ability to fly straight with damaged wings requires that flies maintain large bilateral differences in wing motion [28], these kinematics must be regulated with extreme precision because of the strong nonlinear influence of wing length and speed on aerodynamic forces and moments [11].

In this chapter, we present the results of extensive experiments to further elucidate the role of the DNg02 neurons in flight stabilization. By genetically silencing the DNg02 cells, we show that the magnitude of the optomotor response is diminished in proportion to the number of pairs silenced, providing support for the population coding hypothesis. These results indicate that these neurons are necessary for the optomotor response, insofar as they are required for the response to reach its full magnitude. We employed two-photon functional imaging of DNg02 neurons in an array of different driver lines, confirming that this cell class exhibits bilaterally asymmetric responses to visual yaw stimuli [30]. In Chapter 4, we continue our investigation into the function of the DNg02 neuronal population and its effects on the motor system.

3.3 Results

Coordination of different motor systems during the optomotor response.

To probe the behavioral structure and neuronal implementation of the optomotor response, we tracked the kinematics of tethered flies while presenting open-loop visual stimuli simulating rotation about the yaw axis (Figure 3.1A-B). We aligned flying flies to a machine vision system that measured wingbeat amplitude in real time, whereas head angle, abdomen angle, and leg positions were measured offline from

the recorded image stream using DeepLabCut [27]. An example of a behavioral response to wide field visual motion is plotted in Figure 3.1C. The optomotor response is often quantified in tethered flies using the bilateral difference in wingbeat amplitude of the two wings, ΔWBA. Under the assumption that the flies' behavior is bilaterally symmetric, we normalized these responses such that the angle of the wing on the inside of the induced turn (WBA_i) was subtracted from the angle of the outside wing (WBA_o) (Figure 3.2A), thereby combining yaw responses to the left and right into one data set. Upon presentation of the optomotor stimulus, ΔWBA rapidly increased until it reached a plateau of approximately 20° that was maintained for the duration of the stimulus period. The flies generated this difference in wingbeat amplitude via a decrease in WBA_i of 7°, and an increase in WBA_o of 13° (Figure 3.3A-B). At the offset of the stimulus, ΔWBA decayed slowly as has been noted previously [35].

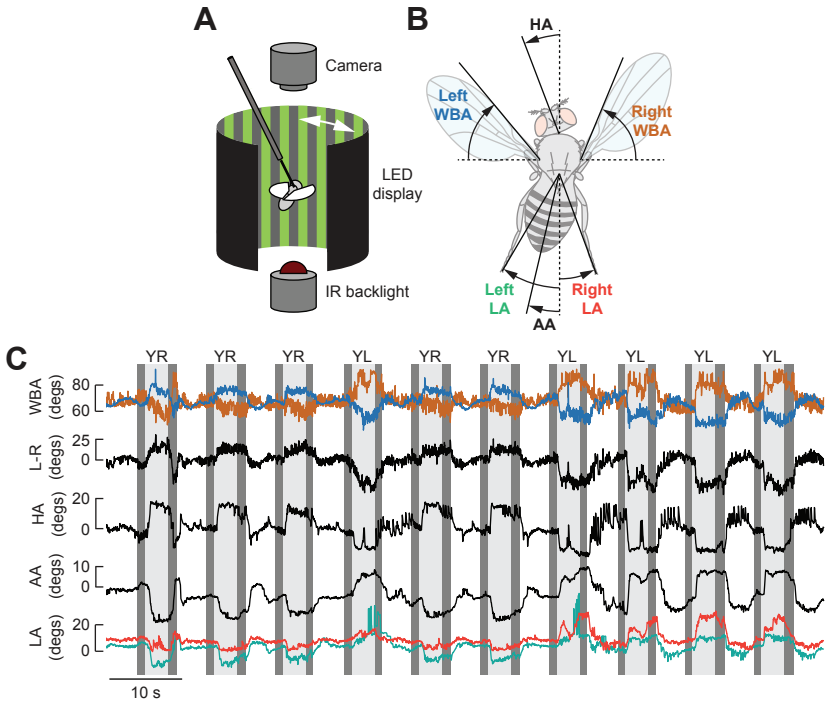

Figure 3.1: Optomotor response experimental apparatus and data collected.
(A) Schematic of the experimental set-up (not drawn to scale). The fly is centered within a curved visual display of green LEDs. An image of the fly is captured on a downward facing camera and analyzed using a real-time machine vision system that measures the wingbeat amplitude of the left and right wing.
(B) Cartoon showing the kinematic parameters recorded during experiments.
(C) Example time traces of left and right wingbeat amplitudes (WBA), left minus right amplitude (L-R), head angle (HA), abdomen angle (AA), and leg angles (LA). Presentations of yaw motion to the left (YL) and right (YR) (light gray) were interspersed with epochs of closed loop stripe fixation (white) and a static striped drum pattern (dark gray). The left leg is shift vertically by 20° for visual clarity.

Whereas the optomotor response is typically quantified by tracking changes in wing motion, flies coordinate their wing responses with adjustments in head position and

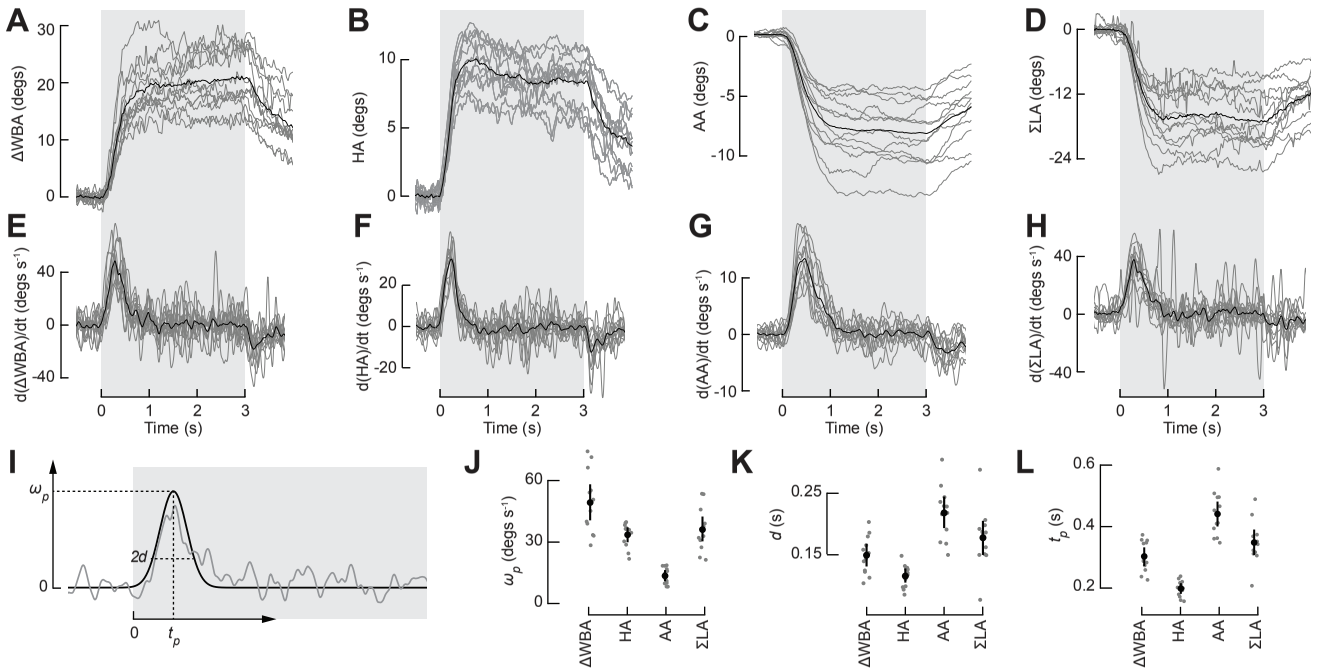

Figure 3.2: The optomotor response consists of coordinated actions of different motor systems.
(A) Averaged wingbeat amplitude differential (ΔWBA) during the presentation of yaw motion (n = 12 flies). ΔWBA is normalized to the direction of the yaw motion, such that the amplitude of the wing decreasing in amplitude (the inside wing relative to the direction of motion, WBA_i) is subtracted from the amplitude of the wing increasing in amplitude (the outside wing, WBA_o). The mean response of individual flies is shown in light gray and the mean across all flies is shown in black. The period of stimulus presentation is shown by the gray patch.
(B-D) As in (A), for HA, AA, and the sum of the leg angles (ΣLA, respectively).
(E) Time derivative of ΔWBA, calculated using a Savitzky-Golay filter (n = 12 flies). Plotting conventions as in Figure 1D.
(F-H) As in (E), for HA, AA, and ΣLA, respectively.
(I) Schematic showing the definitions of the parameters governing the Gaussian functions fit to the time derivative traces in (E-H). See text for details.
(J) Peak angular velocity of ΔWBA, head, abdomen, and leg movements.
(K) Duration of wing, the head, abdomen, and leg movements.
(L) Timing of wing, the head, abdomen, and leg movements.

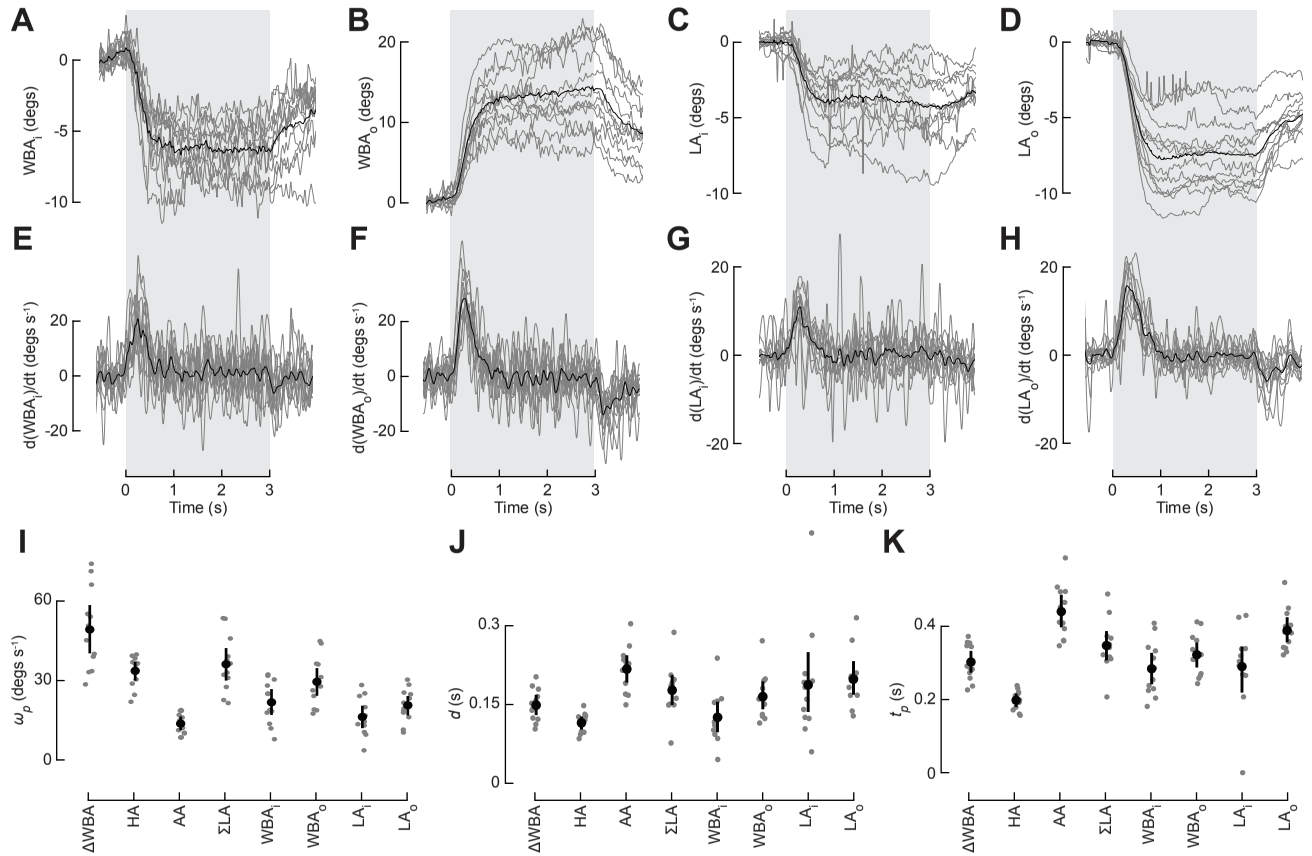

Figure 3.3: Wing and leg optomotor responses.
(A) Averaged inside WBA (WBA_i) during the presentation of yaw motion (n = 12 flies). Plotting conventions as in Figure 1D.
(B-D) As in Figure (A), for outside WBA, WBA_o, inside leg angle, LA_i, and outside leg angle, LA_o, respectively.
(E) Time derivative of WBA_i during the presentation of yaw motion (n = 12 flies). Plotting conventions as in Figure 1D.
(F-H) As in Figure (E), for WBA_o,LA_i, and LA_o, respectively.
(I) Peak angular velocity movements for all tracked kinematic parameters (ΔWBA, head, abdomen, ΣLA, individual wing, and individual leg angles).
(J) As in (K), for duration of the movement.
(K) As in (K), for the timing of the movement.

body posture. The head motion is thought aid in gaze stabilization by minimizing retinal slip [5, 20, 23], while ruddering of the legs and abdomen are thought to contribute torque [3, 18]. The head motion we measured consisted of a quick initial yaw rotation to a plateau value of 10°, followed by a decay at the termination of the optomotor stimulus (Figure 3.2B). Similarly, the flies quickly deflected their abdomen and hind legs at the onset of visual motion (Figure 3.2C-D, Figure 3.3C-D), consistent with prior studies [3, 41]. These deflections of the abdomen and hind legs have been suggested to complement the torque generated by the wings during the optomotor response [18], a hypothesis that is supported by our results that the abdomen and legs deflected toward the side of the inside wing of the fictive turn.

To quantify and compare the dynamics of the different motor reflexes, we calculated the time derivatives of the wing, head, abdomen, and leg responses, and then normalized the sign of the responses such that the peak angular velocity is plotted as positive (Figure 3.2E-H, Figure 3.3E-H). In the case of the wing responses, we wish to make clear that we measured the velocity of the changes in ΔWBA (which is an angle representing the left-right difference in the ventral extent of the stroke envelopes), not the angular velocity of the individual wings as they flapped back in forth, which is of course much faster. As all four reflexes consisted of a quick initial response followed by a plateau or slow movement, the derivatives all exhibit an initial peak in angular velocity that is well approximated by a Gaussian function, which provides a convenient means for quantitative comparison. A Gaussian fit parametrizes the behavioral response as

$$\omega = \omega_p \exp\left(-\frac{(t - t_p)^2}{2d^2}\right) \tag{3.1}$$

where ω is the angular velocity of the given body structure, t is the time in seconds, ω_p is the peak 167 angular velocity, t_p is the time of the peak angular velocity, and d quantifies the width of the curve 168 (Figure 3.2I). We found that ω_p was greatest for the ΔWBA and smallest for the abdomen movement (Figure 3.2J). When the wings and legs are decomposed into the inside and outside appendages individually, we found that the head angle changes with the greatest angular velocity (Figure 3.3I). Our results are consistent with prior work [10, 34] showing that the duration of the head movement in flies is less than that of the wings (Figure 3.2K, Figure 3.3J). The head movement peaks the earliest (Figure 3.2L, Figure 3.3K), suggesting that, as with the optomotor response of walking flies [5], head movement precedes that of the rest of the body. The rapidity of head movement relative that we measured in

these fictive maneuvers is also consistent with studies of spontaneous saccades in free flying flies [34, 39].

Consistent morphological variation among DNg02 cells suggests the existence of distinct sub-classes.

Because DNg02 neurons appear well suited to regulate wing motion over a large dynamic range via a population code and receive input from regions of the brain associated with visual processing [29, 30], we sought to examine their potential role in the optomotor response. To this end, we first set out to conduct a more comprehensive anatomical analysis of the 13 available split-Gal4 driver lines, to better interpret the results of experimental manipulations. High resolution confocal imaging of preparations expressing both membrane-bound GFP and nuclear DsRed enabled us to visualize the fine arbors and more reliably count the number of somata in each line (Figure 3.4A-B, 3.5A). The cell bodies of DNg02 neurons reside at the ventral edge of the gnathal ganglion (GNG), with axons forming a fiber tract that runs ventrally along the GNG before ascending dorsally (Figure 3.4B). To be included in our quantification of cell number, a cell body was required to have a nucleus in the appropriate cluster and an axon following the relevant tract. On average, we found 40% more DNg02 cells in each driver line than reported previously [29, 30], a discrepancy that we attribute primarily to the benefit of marking nuclei with DsRed, which make somata easier to count.

The morphology of DNg02 neurons have been characterized previously and were thought to be nearly homomorphic, possessing arborizations in inferior bridge (IB), inferior clamp (ICL), superior posterior slope (SPS), inferior posterior slope (IPS), as well as the GNG [29, 30]. Smooth processes in the IPS, SPS, and ICL suggest that these regions contain dendrites, whereas the presence of synaptotagmin-positive varicosities suggest that the IB and GNG contain output regions [29]. However, our new analysis identified subtle heterogeneities in the morphology of the cells targeted in the different driver lines. For example, some lines possess arbors that extend dorsally in the ICL, whereas others do not (Figure 3.5A). We observed another notable variation in the neurites within the GNG (arrowheads; Figure 3.6A), which was clearly observed in 4 of the 13 lines. To ascertain whether specific driver lines were enriched for particular DNg02 variants, we determined the morphology of individual cells by stochastically labeling neurons using the multicolor flip-out technique [31] (Figure 3.6B). For this analysis, we selected split-Gal4 drivers representing the variable arborization patterns observed across the lines. As innervation of the

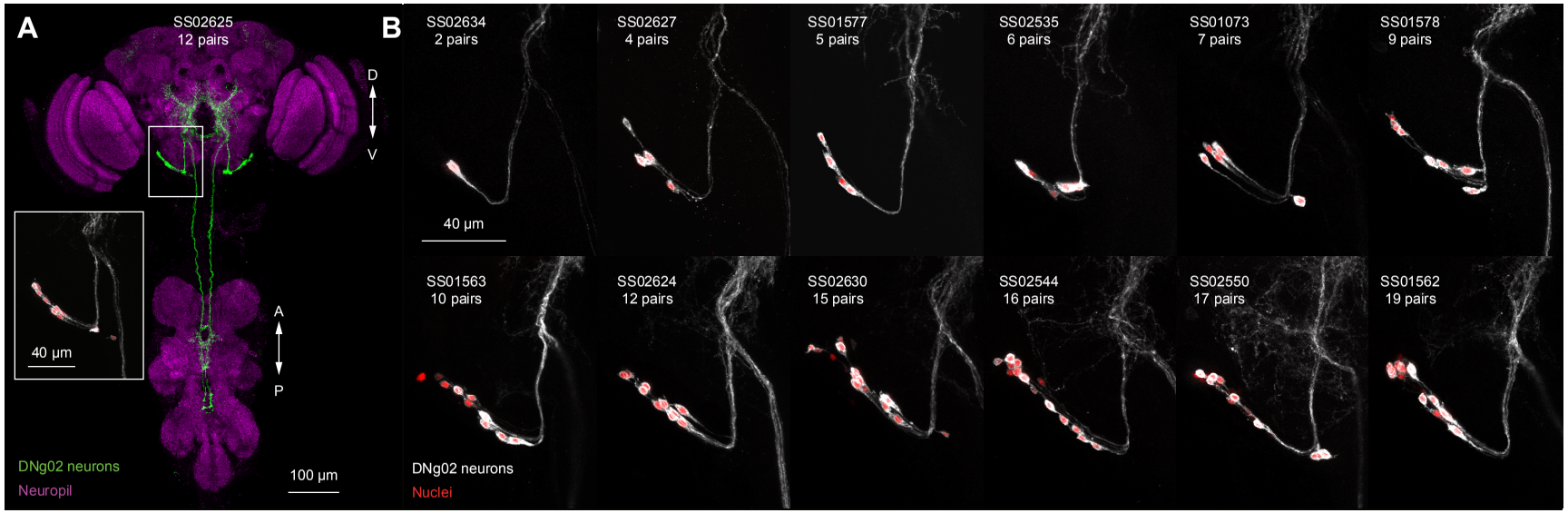

Figure 3.4: Different driver lines label different numbers of DNg02 cells.
(A-B) Confocal z-projections of DNg02 neurons in the fly central nervous system (CNS). Split-Gal4 ID numbers are indicated in each panel.
(A) Expression pattern in an example driver line (SS02625) targeting DNg02 neurons in the full CNS. Green: membrane GFP; magenta: nc82. Inset: High magnification confocal z-projections of DNg02 cell bodies along the ventral ridge of the GNG. White: membrane GFP; red: nuclear localized DsRED.
(B) Expression patterns represented as in (A; inset) across the full set of split-Gal4 lines, sorted in ascending order based on the number of bilateral pairs in each line.

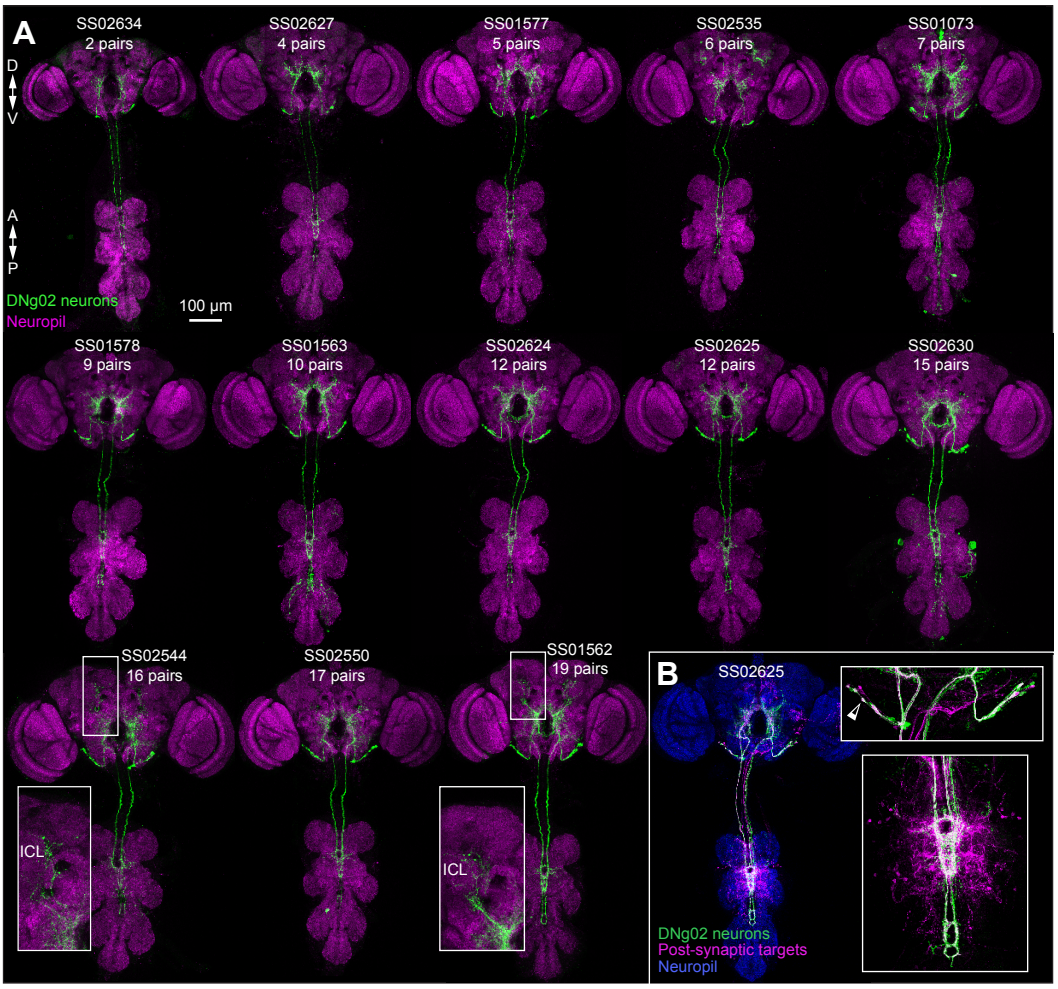

Figure 3.5: Full CNS morphology of DNg02 cells.
(A-B) Confocal z-projections of DNg02 neurons in the fly central nervous system (CNS). Split-Gal4 ID numbers to visualize expression indicated in each panel.
(A) Expression pattern in all driver lines targeting DNg02 neurons in the full CNS. Green: membrane GFP; magenta: nc82. Insets show projections to ICL present in a subset of the driver lines.
(B) Postsynaptic targets of DNg02 neurons as revealed by trans-Tango in the full CNS. Green: membrane GFP in DNg02s; magenta: postsynaptic targets; blue: nc82. Top inset: DNg02 cell bodies. Coexpression of upstream and downstream labeling suggesting reciprocal connectivity (empty arrowhead). Bottom inset: plexus of interneurons revealed in wing neuropil.

posterior slope in the brain, midline-crossing innervation of wing neuropil, and distal arbors in the haltere neuropil in the VNC appear to be the most characteristic DNg02 features, we used these as core criteria and identified two major variants within the set of cells identified as belonging to the DNg02 class (Figure 3.6Bi-ii). The two variants innervate comparable neuropil regions in the brain with similar arborization patterns, but display a minor, but consistent, difference in the VNC. Whereas the DNg02 neurons described previously [29, 30], which we refer to as Type I cells, exhibit a figure-of-eight shape in both the wing tectulum and haltere neuropil (Figure 3.6Bi), a secondary variant, Type II cells, does not exhibit the clear figure-of-eight pattern (Figure 3.6Bii).

Although the 13 drivers lines for DNg02 neurons were initially described as labeling members of a nearly homomorphic population of cells [29, 30], our results indicate that different lines contain neurons that exhibit consistent differences in morphology, implying that there may be potential functional subdivisions within the population.

Indeed, the activation experiments performed by Namiki and colleagues (2022) treated the DNg02 neurons as a single population, receiving input from a shared set of neurons and innervating a shared pool of downstream cells (Figure 3.7A). Alternatively, each neuron may act independently, with a distinct set of neuronal inputs and outputs (Figure 3.7B). The identification of Type I and II neurons may indicate that the underlying connectivity is mixture of these two hypotheses, within the morphological variants corresponding to connectivity subpopulations (Figure 3.7C). It is unclear if the heterogeneity in cell morphology is substantial enough to warrant dividing DNg02 cells into two or more distinct DN types, or whether the variants are better viewed as subclasses of DNg02 cells. Investigations into the connectivity of the DNg02 population using, for example, a full CNS connectome (i.e., a connectome with both the brain and the VNC) could elucidate the underlying connectivity structure.

We did identify two neurons that while superficially resembling DNg02 cells, nevertheless warrant distinct classification (Figure 3.6B). Some lines contain a neuron that projects to the ICL, displays a lateral arbor in the GNG, does not innervate the posterior slope, and does not cross the midline in the VNC; rather, it projects laterally in the wing neuropil (Figure 3.6Biii). We believe this cell to be the previously identified DNg03 neuron [29]. Another cell type distinct from the DNg02s observed in some of the driver lines is a cell that prominently arborizes in the GNG and does not descend to the haltere neuropil (Figure 3.6Biv). Given that lines SS01073, SS02550, SS02544, and SS01562 contain a combination of DNg02 neurons and

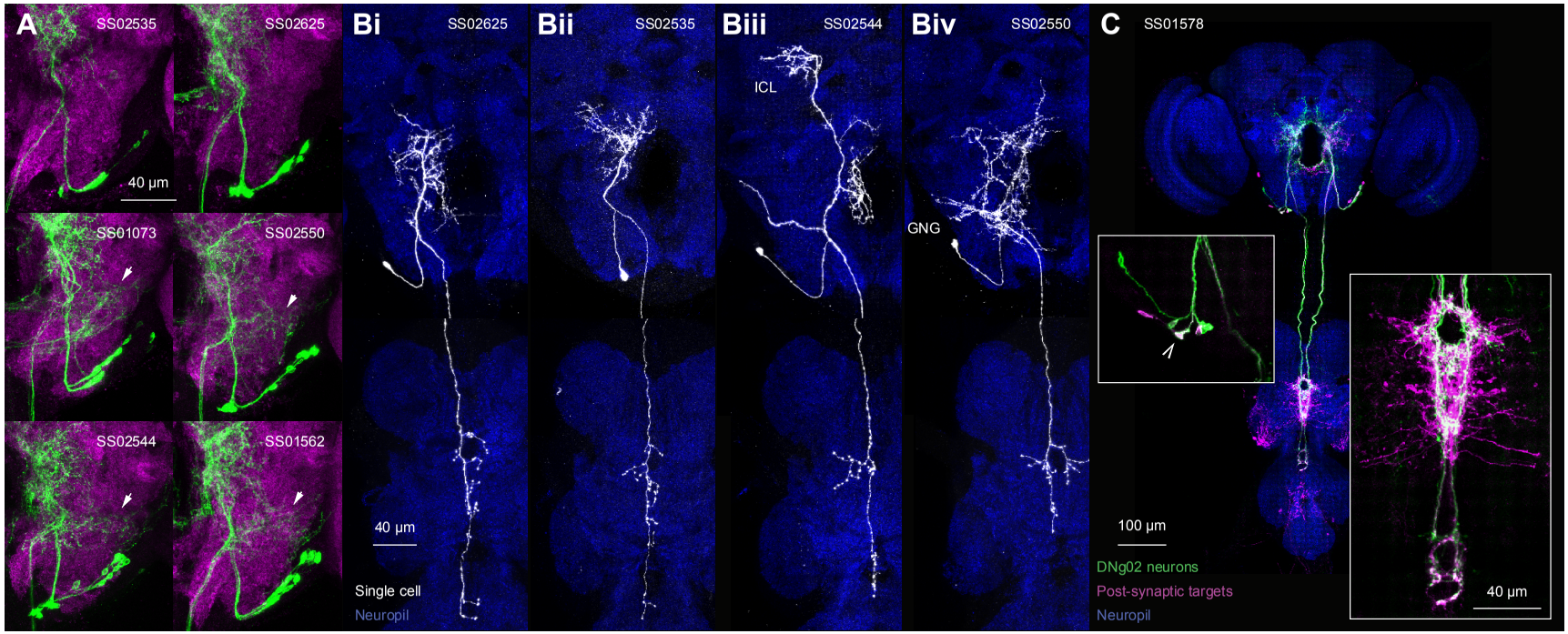

Figure 3.6: Morphology of DNg02 cells.
(A-C) Confocal z-projections of DNg02 neurons in the fly central nervous system (CNS). Split-Gal4 ID numbers are indicated in each panel.
(A) Expression patterns of six representative lines in the GNG. First row and bottom two rows display lines without and with GNG innervation (arrowheads), respectively. Green: membrane GFP; magenta: nc82.
(B) Single cell labeling in the CNS using MCFO across representative split-Gal4 lines with variable innervation patterns: Type I DNg02 (Bi), Type II DNg02 (Bii), DNg03 (Biii), and an unknown descending neuron (Biv). White: MCFO – HA or FLAG; blue: nc82. ICL: inferior clamp; GNG: gnathal ganglion.
(C) Postsynaptic targets of DNg02 neurons as revealed by trans-Tango in the full CNS. Green: membrane GFP in DNg02s; magenta: postsynaptic targets; blue: nc82. Left inset: DNg02 cell bodies. Coexpression of upstream and downstream labeling suggests reciprocal connectivity (empty arrowhead). Right inset: plexus of interneurons revealed in wing neuropil.

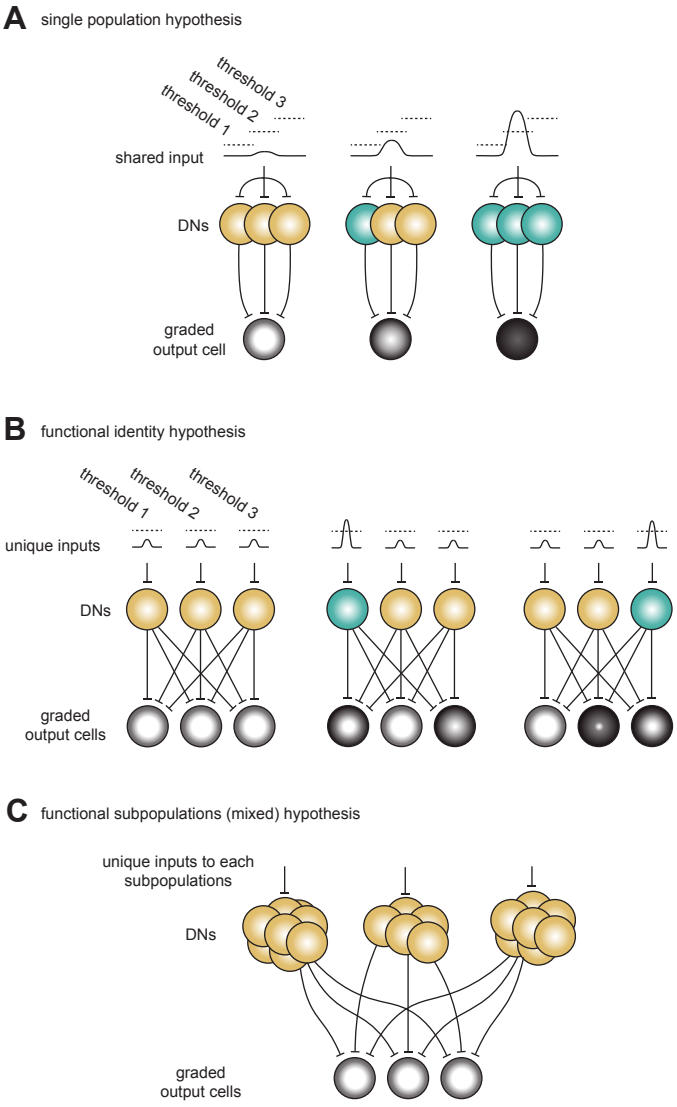

Figure 3.7: Hypothesized population connectivity of DNg02 neurons.
(A) Schematic representation of single population hypothesis. Under this hypothesis, the set of DNg02 neurons act as a single population, all receiving input from the same neurons and sending output to the same neurons with a variable set of weights. Each neuron in the population has a different threshold of activation, such that when the input is more intense, more neurons in the population become active (quiescent neurons in yellow; recruited neurons in teal). The neurons in the population innervate a graded output cell (higher levels of activity indicated by a filled circle).
(B) Schematic representation of functional identity hypothesis. Under this hypothesis, each DNg02 neuron has its own unique set of input and output neurons. Conventions as in (A).
(C) Schematic representation of functional subpopulations hypothesis. This hypothesis combines features from the single population and functional identity hypotheses; here, there are functional subpopulations within the DNg02s which act according to the rules in the single population hypothesis. Conventions as in (A).

other DNs innervating the GNG (Figure 3.6A), we focused subsequent functional analyses on the lines that specifically labeled the DNg02 variants (i.e., Type I and II DNg02 neurons).

To investigate connectivity downstream from the DNg02 population, we used the trans-Tango anterograde transsynaptic labeling system (Figure 3.6C) [37]. Due to the density of staining, it is difficult to cleanly visualize most of the cell types downstream of the DNg02 neurons, but one notable exception is a population of interneurons with cell bodies situated in the ventral cell body rind of the VNC. These neurons project dorsally and splay out in a dense plexus of neurites in the wing neuropil adjacent to, and laterally of, the descending DNg02 fibers. We also found evidence for reciprocal connectivity within the DNg02 population. The trans-Tango preparations showed examples of likely DNg02 cells that exclusively contained a post-synaptic signal, as well as DNg02 neurons that contained both pre- and post-synaptic labels, consistent with monosynaptic connections among cells within the DNg02 population (inset; Figure 3.6C and Figure 3.5B). The presence of DNg02 cells with post-synaptic labeling indicates reciprocal connectivity within the population, although it is not possible to determine whether the connectivity includes connections across the midline from the trans-Tango results alone. We did not observe any motor neurons with post-synaptic labeling, although the possibility of false negatives using the trans-Tango method renders this observation difficult to interpret [32].

Silencing DNg02 cells reduces the magnitude of the optomotor response.

To investigate the role of DNg02 neurons in the optomotor response, we silenced the cells by selectively driving the inwardly rectifying potassium channel Kir2.1 [1] in the set of the nine sparse split-GAL4 driver lines that primarily targeted Type I and II DNg02 neurons. As controls, we also tested wild-type flies and flies in which we crossed UAS-Kir2.1 to a split-GAL4 line carrying empty vectors of the two GAL4 domains (SS03500). Silencing the DNg02 cells reduced the magnitude of the wing optomotor response, with a maximal reduction in ΔWBA from $\sim 20^\circ$ for the wild-type and empty vector control flies to $\sim 10^\circ$ for a driver line labeling 9 pairs of cells (Figure 3.8A). The reduction in ΔWBA during the optomotor response was roughly linear with the number of DNg02 cells silenced (slope = -0.6° cell^{-1}, intercept = 20.6°) (Figure 3.8B). To test whether the observed trend could arise from chance, we performed a bootstrapping analysis in which we randomly sampled wing responses and numbers of cells silenced with 100,000 iterations. We found no

iterations with a more extreme slope than the original dataset, giving a probability of zero that our experimental results arose from chance (Figure 3.8C). In addition, we performed a Wald test on the significance of the slope of the best fit line in Figure 3.8B, and found a p-value of 2×10^{-8} against the null hypothesis of zero slope. When the four driver lines labeling both DNg02 neurons and the neuron with arborization in the GNG were included in the analysis, we still found a statistically significant reduction in the magnitude of the optomotor response in proportion to the number of cell bodies silenced (Figure 3.9A-C). Finally, we tested whether individual split-GAL4 lines resulted in statistically significant reductions in the magnitude of the optomotor response. Using an independent *t* test with Bonferroni correction, we found that only some lines labeling more than five pairs of DNg02s resulted in distributions of responses with nonidentical means, as compared to the empty vector control split. These results support the hypothesis that the DNg02 neurons regulate wingbeat amplitude via population coding. Both the outside wing (which increased in amplitude) and the inside wing (which decreased in amplitude) showed statistically significant reductions in response magnitude with the number of DNg02 neurons silenced, suggesting that DNg02 neurons are involved both in increases and decreases to wingbeat amplitude (Figure 3.10A-F).

To determine how the silencing of cells altered the time course of the changes in ΔWBA, we again fit a Gaussian function to the derivative of the response curves (Figure 3.8D-E). We found a significant reduction in ω_p, the maximum velocity of the change in the ΔWBA angle, a slight but significant increase in t_p, the timing of the peak velocity, but no change in d, the duration of the response. This suggests that the decrease in the magnitude of the optomotor response is due to a reduction in the peak velocity of the change in ΔWBA, not in a decrease in the duration of the visual motion reflex.

As with the wing response, we saw a significant reduction in the head, abdomen, and leg responses upon silencing DNg02 neurons (Figures 3.11, 3.12, 3.13, and 3.10G-L). Again, the head, abdomen, and leg optomotor responses appear to be diminished due to a reduction in the angular velocity of the motor response, not a decrease in its duration. Whereas DNg02 neurons directly innervate regions of the VNC associated with flight and other wing-related behaviors, the cells do not make direct projections to the neck, leg, or abdomen neuropils. While this projection pattern does not preclude the existence of connections to motor circuits via a poly-synaptic pathway, it is also possible that the reduction in head, leg, and abdomen optomotor response is mediated indirectly via a decrease in the strength of mechanosensory

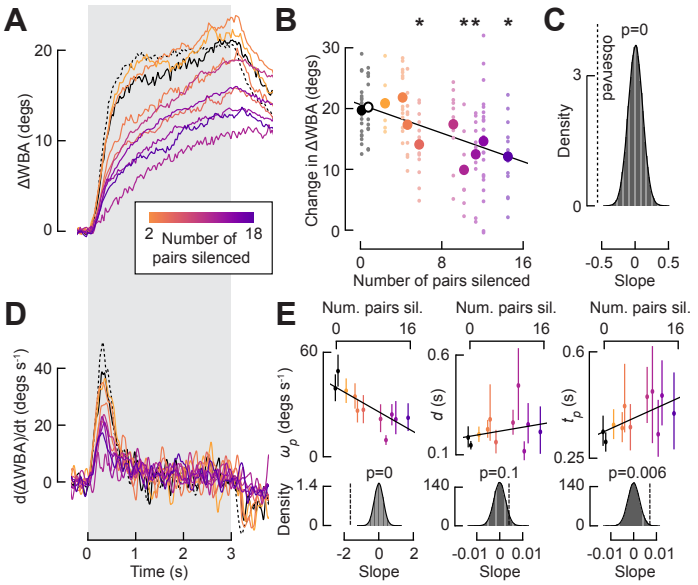

Figure 3.8: Silencing DNg02 neurons diminishes the magnitude of the wing differential optomotor response.
(A) Averaged ΔWBA during the presentation of yaw motion for flies with DNg02 neurons silenced with Kir2.1 (sample sizes throughout figure: empty-split vector control: n = 19; wild-type control: n = 12; SS02634: n = 7; SS02627: n = 14; SS01577: n = 10; SS02535: n = 14; SS01578: n = 14; SS01563: n = 7; SS02625: n = 23; SS02624: n = 10; SS02630: n = 14). The number of pairs of cells silenced is indicated by the color of the trace, with the fewest pairs in yellow and the most in purple. The response of empty-vector control flies (SS03500) is shown with a solid, black line and the response of wild-type control flies is shown with a dotted, black line. The period of stimulus presentation is shown by the gray patch.
(B) ΔWBA plotted against the number of DNg02 pairs silenced. As in (A), the number of pairs silenced is indicated by color. The two controls are offset slightly for visual clarity; the empty vector control is indicated by a solid circle and the wild-type control is indicated by an empty circle. Individual fly means are shown with small circles and grand means for a given driver line is shown with a large circle. Asterisks indicate cases where the mean is statistically different ($p \leq 0.05$, with Bonferroni correction) from the empty-split vector control (independent t test). A line is fit to individual fly means and plotted in black ($r^2 = 0.66$, based on mean values).
(C) Distribution of 100,000 bootstrapped slopes of lines of best fit with responses and numbers of cells silenced randomly sampled with replacement. The dotted, black line indicates the observed slope of the original dataset. The p-value is the proportion of resampled slopes that result in a more extreme slope than observed.
(D) Time derivative of the ΔWBA data shown in (A), calculated using a Savitzky-Golay filter.
(E) Optomotor response is reduced due to a decrease in angular velocity, not a decrease in the duration of movement. Top: As in (B), for the parameters from fitting a Gaussian function to the data in (D) (from left to right, $r^2 = 0.67, 0.08, 0.34$, based on mean values). Bottom: As in (C), for the Gaussian function parameters.

reflexes driven by the changes in wing motion caused by silencing DNg02 cells. When the four driver lines labeling both DNg02 neurons and the neuron with arborization in the GNG were included in the analysis, we still observed significant reductions in the magnitudes of the head and leg responses, although the effect on the abdomen response was not significant (Figure 3.9D-L). The number of DNg02 pairs silenced did not alter the baseline wingbeat amplitude during flight (Figure 3.14); therefore, such an effect could not explain the reduction in any of the visually induced motor responses we observed.

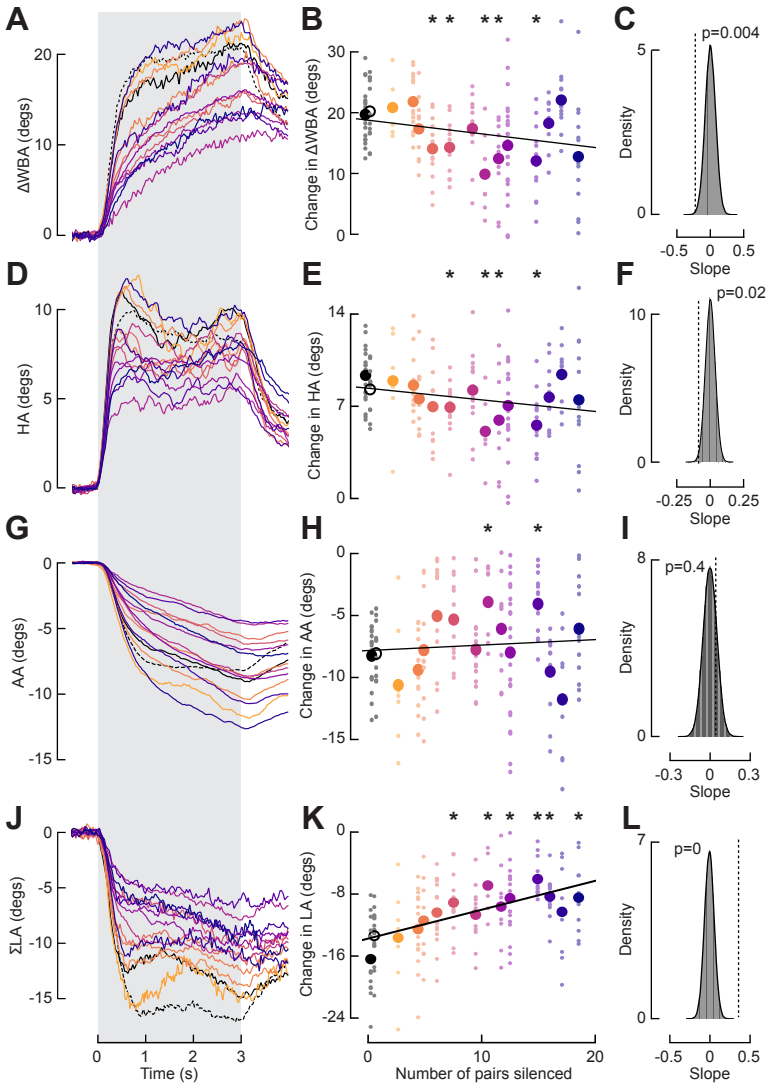

Figure 3.9: Results of silencing DNg02 neurons when lines with GNG projections are included.
(A) Averaged ΔWBA during the presentation of yaw motion for flies with DNg02 neurons silenced with Kir (sample sizes throughout figure: empty-split vector control: n = 19; wild-type control: n = 12; SS02634: n = 7; SS02627: n = 14; SS01577: n = 10; SS02535: n = 14; SS01578: n = 14; SS01563: n = 7; SS02625: n = 23; SS02624: n = 10; SS02630: n = 14; SS01073: n = 13; SS02550: n =17; SS02544: n = 12; SS01562: n = 13). Plotting conventions as in Figure 3A. Driver lines with GNG projections (SS01073, SS02550, SS02544, and SS01562) are included.
(B) Change in ΔWBA plotted against the number of DNg02 pairs silenced. Plotting conventions as in Figure 3.8B (r^2 = 0.17, based on mean values).
(C) Distribution of 100,000 bootstrapped slopes of lines of best fit with responses and numbers of cells silenced randomly sampled with replacement for ΔWBA. Plotting conventions as in Figure 3.8C.
(D) As in (A), for the head optomotor response.
(E) As in (B), for the head optomotor response (r^2 = 0.12, based on mean values).
(F) As in (C), for the head optomotor response.
(G) As in (A), for the abdomen optomotor response.
(H) As in (B), for the abdomen optomotor response (r^2 = 0.01, based on mean values).
(I) As in (C), for the abdomen optomotor response.
(J) As in (A) for the leg optomotor response.
(K) As in (B), for the leg optomotor response (r^2 = 0.63, based on mean values).
(L) As in (C), for the leg optomotor response.

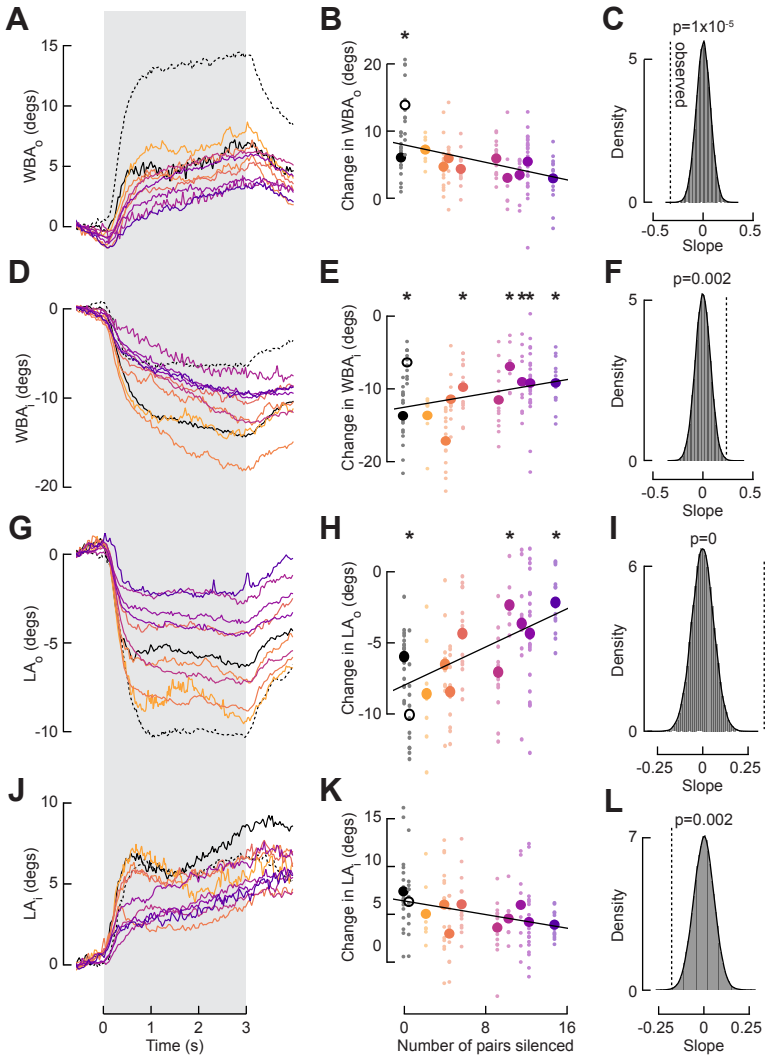

Figure 3.10: Silencing DNg02 neurons diminishes the magnitude of the optomotor response of individual wings and the legs.
(A) Averaged WBA_o during the presentation of yaw motion for flies with DNg02 neurons silenced with Kir2.1 (sample sizes as in Figure 3.8). Plotting conventions as in Figure 3.8A.
(B) Change in WBA_o plotted against the number of DNg02 pairs silenced. Plotting conventions as in Figure 3.8B (r^2 = 0.43, based on mean values).
(C) Distribution of 100,000 bootstrapped slopes of lines of best fit with responses and numbers of cells silenced randomly sampled with replacement for WBA_o. Plotting conventions as in Figure 3.8C.
(D) As in (A), for the WBA_i optomotor response.
(E) As in (B), for the WBA_i optomotor response (r^2 = 0.15, based on mean values).
(F) As in (C), for the WBA_i optomotor response.
(G) As in (A), for the LA_o optomotor response.
(H) As in (B), for the LA_o optomotor response (r^2 = 0.62, based on mean values).
(I) As in (C), for the LA_o optomotor response.
(J) As in (A), for the LA_i optomotor response.
(K) As in (B), for the LA_i optomotor response (r^2 = 0.30, based on mean values).
(L) As in (C), for the LA_i optomotor response.

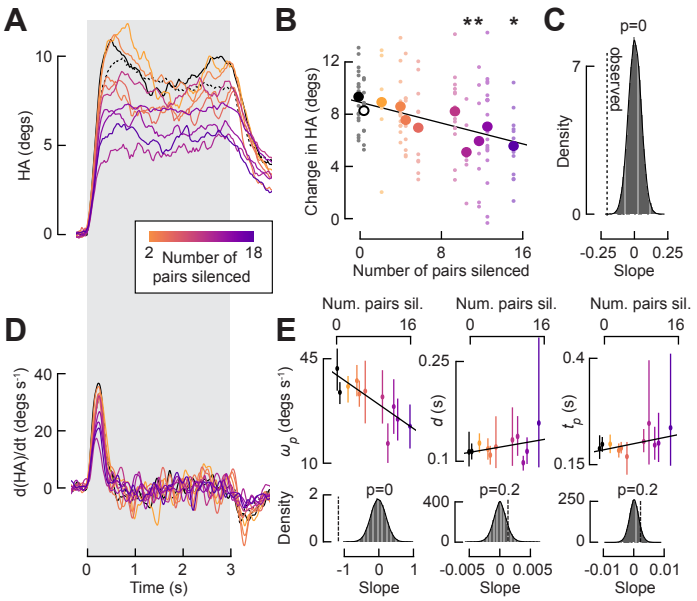

Figure 3.11: Silencing DNg02 neurons diminishes the magnitude of the head optomotor response.
(A) As in Figure 3.8A, for head optomotor response.
(B) As in Figure 3.8B, for head optomotor response (r^2 = 0.66, based on mean values).
(C) As in Figure 3.8C, for head optomotor response.
(D) As in Figure 3.8D, for head optomotor response.
(E) As in Figure 3.8E, for head optomotor response (top row, from left to right, r^2 = 0.65, 0.16, 0.33, based on mean values).

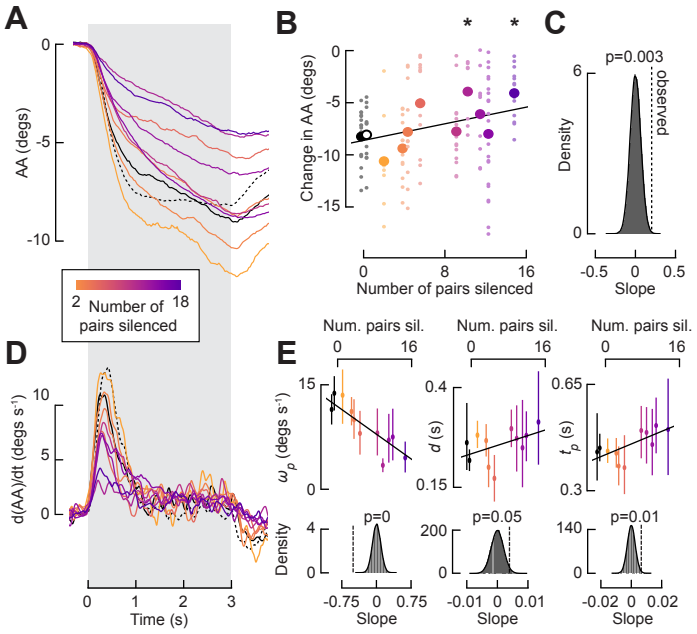

Figure 3.12: Silencing DNg02 neurons diminishes the magnitude of the abdomen optomotor response.
(A) As in Figure 3.8A, for abdomen optomotor response.
(B) As in Figure 3.8B, for abdomen optomotor response (r^2 = 0.41, based on mean values).
(C) As in Figure 3.8C, for abdomen optomotor response.
(D) As in Figure 3.8D, for abdomen optomotor response.
(E) As in Figure 3.8E, for abdomen optomotor response (top row, from left to right, r^2 = 0.78, 0.21, 0.46, based on mean values).

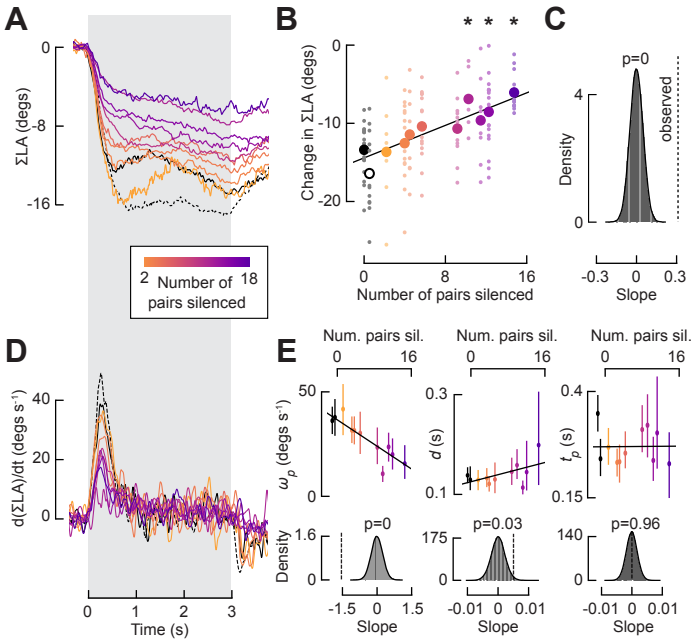

Figure 3.13: Silencing DNg02 neurons diminishes the magnitude of the leg optomotor response.
(A) As in Figure 3.8A, for leg optomotor response.
(B) As in Figure 3.8B, for leg optomotor response (r^2 = 0.85, based on mean values).
(C) As in Figure 3.8C, for leg optomotor response.
(D) As in Figure 3.8D, for leg optomotor response.
(E) As in Figure 3.8E, for leg optomotor response (top row, from left to right, r^2 = 0.79, 0.31, 0.004, based on mean values).

DNg02 activity correlates to motor output and is consistent across morphological variants.

Our silencing experiments indicate that DNg02 neurons are required for the optomotor response to reach its full magnitude. To investigate how the DNg02 cells respond to the visual optomotor stimulus, we performed two-photon functional imaging in tethered flying flies using GCaMP7f and GCaMP8m [42] as an activity indicator (Figure 3.15A-B). We selected driver lines that labeled either only the Type II DNg02 variant (that is, lines without a clear figure-of-eight shape within the haltere neuropil), or lines that likely labeled both Type I and Type II DNg02 neurons (i.e., lines that contained at least some cells with the clear figure-of-eight feature), in order to attempt to identify functional roles of the two variants. During these experiments, flies often stop flying, in which case we would try to re-initiate flight with a puff of air. We made use of these occasional flight stops (and subsequent puff-induced starts) to record the activity of DNg02 neurons during the transitions between flight and quiescence (Figure 3.15C). We found a higher level of activity during flight than quiescence, a trend consistent with other cells in the brain [25].

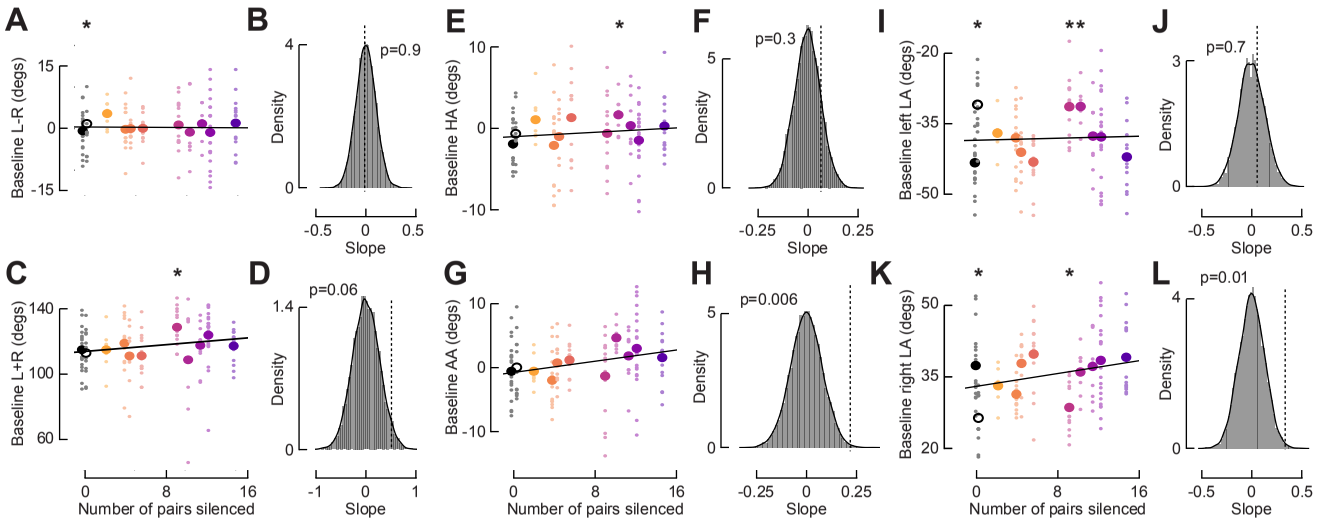

Figure 3.14: Effects of silencing DNg02 neurons on the optomotor response is not due to changes in baseline kinematics.
(A) Baseline left minus right WBA plotted against the number of DNg02 pairs silenced (sample sizes as in Figure 3.8). The 1 s period of static grating preceding presentations of the optomotor stimuli is taken as the baseline period. Plotting conventions as in Figure 3B (r^2 = 0.02, based on mean values).
(B) Distribution of 100,000 bootstrapped slopes of lines of best fit with responses and numbers of cells silenced randomly sampled with replacement for baseline left minus right WBA. Plotting conventions as in Figure 3.8C.
(C) As in (A), for WBA sum (r^2 = 0.13, based on mean values).
(D) As in (B), for WBA sum.
(E) As in (A), for HA (r^2 = 0.08, based on mean values).
(F) As in (B), for HA.
(G) As in (A), for AA (r^2 = 0.34, based on mean values).
(H) As in (B), for AA.
(I) As in (A), for left LA (r^2 = 0.001, based on mean values). (J) As in (B), for left LA.
(K) As in (A), for right LA (r^2 = 0.19, based on mean values).
(L) As in (B), for right LA.

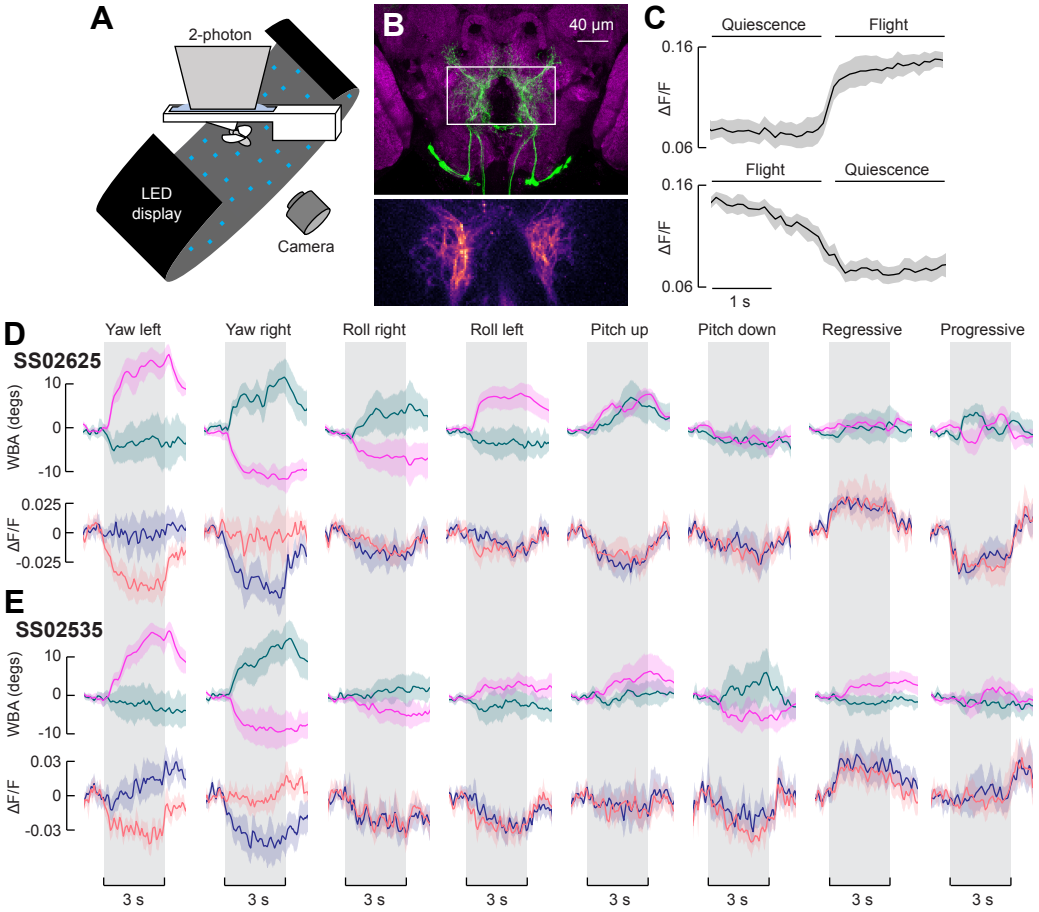

Figure 3.15: DNg02 neurons respond to optomotor stimuli.
(A) Schematic showing the experimental set-up used for two-photon functional imaging. A fly is tethered to a flight stage under the microscope at the center of an array of LEDs. A camera tracks wing position in real-time using a machine vision system.
(B) We imaged a region, outlined in white, capturing DNg02 branches bilaterally. Bottom: standard deviation of GCaMP8m fluorescence over time. The 10% most variable pixels are used to define a region of interest within which we measure changes in fluorescence. See Methods for details.
(C) Average fluorescence as the fly transitions between quiescence and flight, agnostic to visual stimuli (n = 7 flies, 198 transitions from quiescence to flight, 188 transitions from flight to quiescence). Bilateral fluorescence increases at the onset of flight and decreases at the offset.
(D) Averaged wing and fluorescence responses to different patterns of optic flow for SS02625, a driver line labeling both Type I and Type II DNg02 variants (n = 9 flies). Top row shows baseline-subtracted left (teal) and right (pink) wingbeat amplitudes; bottom row shows baseline-subtracted left (blue) and right (salmon) DNg02 activity. Data are presented as mean (solid line) and a bootstrapped 95% CI for the mean (shaded area). The 3 s stimulus period is shown by the gray patch.
(E) As in Figure (D), for SS02535, a driver line labeling exclusively Type II DNg02 neurons (n = 11 flies).

To probe the role of the DNg02 neurons in flight stabilization and any functional variations between the Type I and II variants, we presented wide-field visual stimuli simulating the optic flow flies would experience during pitch, roll, and yaw rotations of the body, as well as progressive and regressive translations (Figure 3.15D-E and 3.16). These stimuli were selected to induce a diverse array of flight behaviors. Whereas roll and yaw stimuli induce asymmetric wingbeat responses, pitch, regressive, and progressive stimuli induce symmetric responses [17]). Presentations of optomotor stimuli were interspersed with epochs of a static starfield to return wing kinematics to baseline. Broadly, our results recapitulate previously reported responses in DNg02 neurons to these visual stimuli in one specific driver line [30], with some notable exceptions (Figure 3.15D-E). Previous work reported robust increases and decreases in DNg02 activity correlated with contralateral wing motion during the presentation of yaw motion (e.g., in response to leftward drifting stimulus, the right wing increased in amplitude as the left DNg02 increased in activity, while the left wing decreased in amplitude as the right DNg02 decreased in activity). In contrast, we observed only weak increases in DNg02 activity during the presentation of yaw motion, although we did observe robust decreases in activity. Furthermore, whereas previous work reported asymmetric neuronal responses without behavioral responses to roll motion, we observed asymmetric behavioral responses, as quantified by changes in wing kinematics, and weak symmetric decreases in neuronal activity. Regardless, the broad results are the same as previously reported; that is, DNg02 activity correlates with contralateral wingbeat amplitude and DNg02 cells can respond independently on the left and right sides of the brain. We further note that the highest magnitude neuronal responses are induced by yaw, regressive, and progressive motion, all of which consist primarily of patterns of horizontal optic flow. We repeated the experiments with driver lines labeling both Type I and Type II DNg02 neurons (Figure 3.15D, 3.16A), exclusively Type II cells (Figure 3.15E, 3.16B), and a line labeling Type II neurons and neurons with GNG innervation (Figure 3.16C) and found that the responses are the same regardless of the driver line imaged.

Because the results of both the silencing screen we present here and the activation screen in a prior study [30] suggest that the DNg02 cells likely operate via population coding, we performed a further set of functional imaging experiments to determine if we could find evidence for stimulus-dependent recruitment, such that the number of cell activated increases with the strength of the visual stimulus. Given that the strongest responses were to yaw motion, we presented these patterns of optic flow

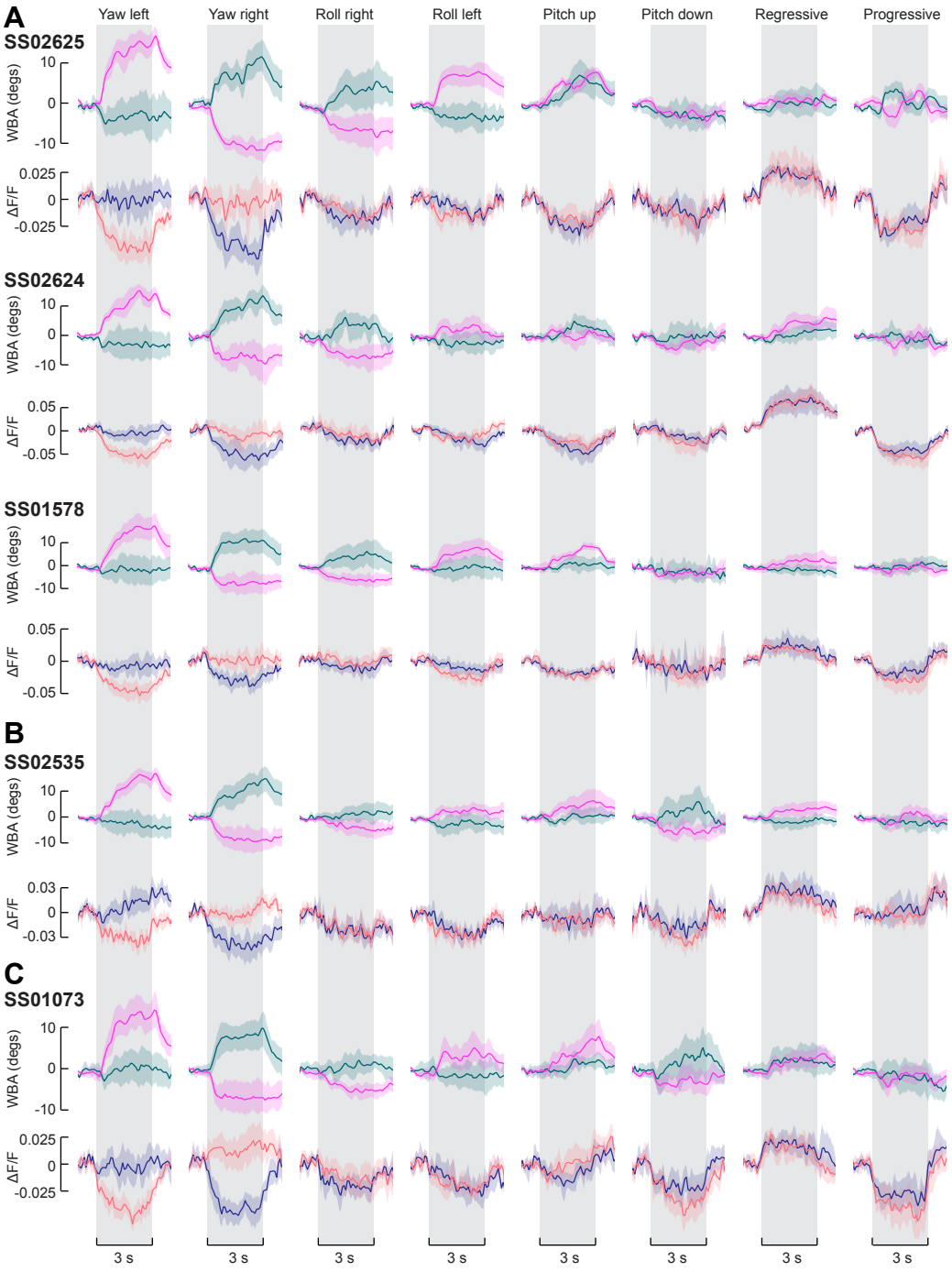

Figure 3.16: DNg02 activity is the same across different driver lines labeling different DNg02 variants.
(A) Averaged wing and fluorescence responses to different patterns of optic flow for three driver line labeling both Type I and Type II DNg02 variants. Plotting conventions as in Figure 3.15D.
(B) As in Figure (A), for a driver line labeling exclusively Type II DNg02 neurons.
(C) As in Figure (A), for a driver line labeling Type II DNg02 neurons and some neurons with arborization in the GNG.

across a range of stimulus angular velocities, in order to induce different magnitude neuronal and behavioral responses. To maximize our ability to resolve individual cells, we only imaged the DNg02 cells on one side of the brain (Figure 3.17A). However, we were not able to resolve individual cells to specifically test whether different neurons became active at different strengths of the visual stimulus or were correlated with different magnitudes of the motor response. The driver line we tested, SS02535, labels 6 pairs of neurons, but it is possible that a line targeting fewer pairs would allow us to distinguish individual cells. We used the calcium indicator GCaMP7f for these experiments. As has been reported previously [30], DNg02 activity appears to be correlated with contralateral wingbeat amplitude and anticorrelated with ipsilateral wingbeat amplitude relative to the side of the brain on which we imaged (Figure 3.17B). Plotting the ΔWBA (here, ipsilateral wingbeat amplitude subtracted from contralateral) and the fluorescence signal within the ROI (ΔF/F) against the angular velocity of the pattern presented (Figure 3.17C) indicates that both responses saturate at velocities of $>15^\circ$ s^{-1}. However, when we directly plotted the ΔWBA in deciles of fluorescence (independent of the angular velocity at which the data were collected), we found a strongly linear relationship (Figure 3.17D), suggesting that DNg02 activity is tightly coupled to the motor response. The coupling was also observed, albeit weakly, when the calcium indicator GCaMP8m and the driver line SS02625, labeling 12 pairs of cells, was used (Figure 3.18). While the silencing experiments and previously reported activation experiments [30] suggest that there is a causal relationship between DNg02 activity and wing motion, this coupling could also arise in part from ascending feedback signals from neurons in the VNC.

We believed that the different responses reported in Figures 3.15D-E and 3.16 and in the previous work [30] may be due, in part, to the different calcium indicator used; the prior work used GCaMP6f while these experiments were performed with GCaMP8m. The differences in our results may also have been due to imaging a slightly different region of the brain, which could result in recording the activity of different DNg02 cells than in the previous study. To disambiguate between these possibilities, the data presented in Figures 3.17 and 3.18 were performed with GCaMP7f and GCaMP8m, respectively. The robust increases in DNg02 fluorescence reported previously in response to optomotor stimuli [30] were observed in the experiments with GCaMP7f but not GCaMP8m, suggesting that the different response patterns observed here are due to the different calcium indicator used, rather than imaging in a different region.

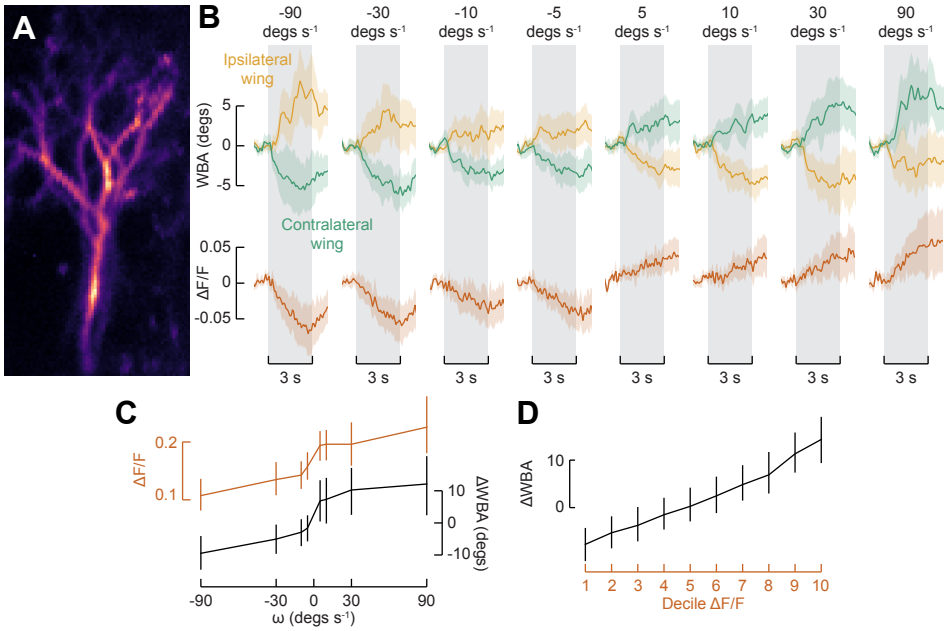

Figure 3.17: DNg02 activity correlates with visually-elicited motor responses.
(A) Standard deviation of GCaMP7f fluorescence for an example of unilateral imaging. Cells on the right side of the brain are shown. The driver line used for these experiments, SS02535, labels DNg02 neurons of both Type I and Type II morphology.
(B) Averaged wing and fluorescence responses to yaw motion at a range of angular velocities (n = 12 flies). Ipsilateral and contralateral wingbeat amplitudes shown on the top row; DNg02 fluorescence shown on the bottom. Plotting conventions as in Figure 3.15D.
(C) Mean fluorescence and ΔWBA (ipsilateral amplitude subtracted from contralateral) across stimulus angular velocities (n = 12 flies). Mean is taken over the final second of stimulus presentation (i.e., from t = 2 to 3 s). Error bars show bootstrapped 95% CI.
(D) Mean ΔWBA, parsed in deciles of fluorescence. The plot incorporates data collected across the full range of visual stimulus conditions. Error bars show bootstrapped 95% CI.

3.4 Discussion

In this chapter, we examined the role of a population of descending neurons in the optomotor response of flying Drosophila. The optomotor response consists of coordinated movements of different appendages, including changes in wing kinematics, head position, and deflections of the abdomen and hind legs. Prior work based on anatomy and optogenetic activation identified the DNg02 neurons as likely candidates for regulating mechanical power and mediating steady-state flight control by transmitting optic flow from the brain to motor centers in the VNC. In this chapter, we further tested this hypothesis through a combination of anatomy, genetic silencing, unilateral optogenetic activation, and functional imaging. When DNg02 neurons were inactivated via chronic expression of the inward-rectifying potassium channel Kir2.1, the magnitude of the optomotor response was diminished in proportion to the numbers of cells silenced, up to a value of 50% compared to the responses of wild-type or empty-vector control flies (Figure 3.8). It is possible that DNg02 neurons provide direct input to flight motor neurons or local pre-motor

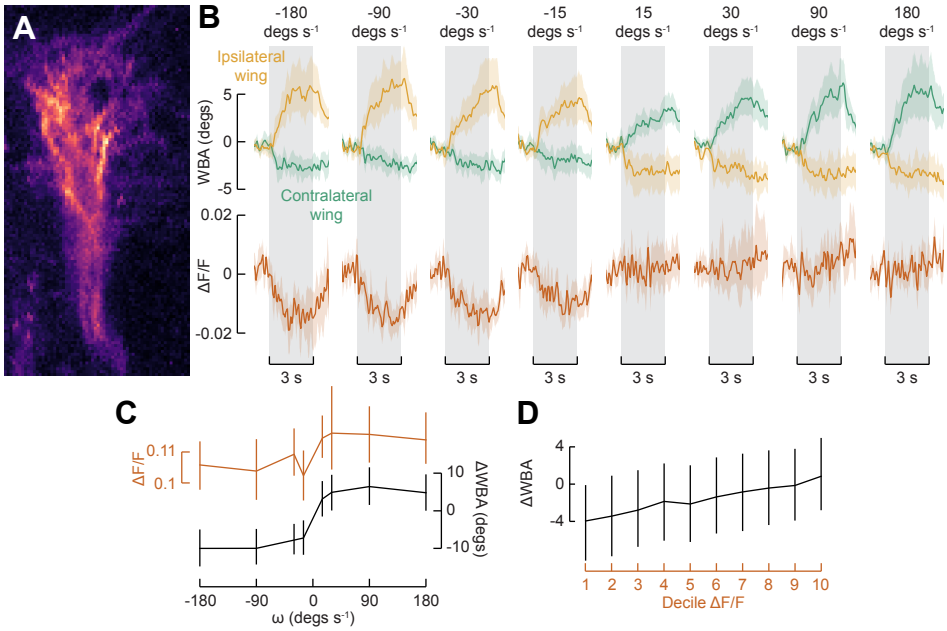

Figure 3.18: DNg02 activity weakly correlates with visually-elicited motor responses when recording with GCaMP8m.
(A-D) As in Figure 3.17 for data collected using GCaMP8m and SS02625, a driver line used for these experiments labeling DNg02 neurons of both Type I and Type II morphology.

interneurons, as the cells project to the wing neuropil. However, we also observed a similar reduction in the optomotor responses of the head (Figure 3.11), abdomen (Figure 3.12), and legs (Figure 3.13), although these reflexes are less likely to be driven directly by DNg02 cells as they do not project to the relevant motor neuropils. It is therefore unclear whether the reductions in these responses are due to polysynaptic connections from the DNg02 cells to neck, leg, and abdomen motor neurons, or alternatively, through changes in reflexive pathways that are reduced by the diminution of the wing response. For example, if mechanosensory feedback from wing mechanoreceptors is partially responsible for eliciting movements of the neck, legs, and abdomen, these reflexes might be attenuated by the reduction in the magnitude of the wing response. Further experiments will be necessary to test between these two alternatives.

There are several non-mutually exclusive explanations for why genetic silencing did not result in complete abolishment of the optomotor response. First, even with the driver line labeling the highest number of cells, we may not have been able to silence the complete set of DNg02 neurons. Second, it is possible that Kir2.1 expression does not completely abolish the ability of these cells to conduct spikes to the VNC. Finally, there may be additional, as of yet unknown, classes of DNs that are involved in the optomotor response besides DNg02.

We conducted additional experiments that sought to illuminate the possible role of different morphological types of DNg02 neurons in the optomotor response. Two-photon imaging experiments suggest that morphological differences within the DNg02 population do not appear to correspond to functional subpopulations, at least with respect to the responses elicited by the set of wide-field patterns of optic flow that we presented (Figures 3.15 and 3.16). It is possible, however, that our stimulus set did not include patterns of visual motion (or other sensory stimuli) that would illuminate functional differences among the different DNg02 types. The cells may also diversify functionally within the VNC, such that all DNg02 cells exhibit the same patterns of activity but have differing effects on the motor system. If that is true, however, we were not able to detect such differences by monitoring wingbeat amplitude, but different DNg02 types might elicit changes in other features of wing motion that are not detected by our machine vision system (e.g., changes in stroke deviation or angle of attack). The DNg02 cells appeared to have the strongest responses to patterns of visual motion in the horizontal plane (i.e., yaw, regressive, and progressive motion) and neurons on the left and right side of the nervous system can be active independently from each other. Responses to yaw motion over a range of rotational velocities suggest that DNg02 activity is tightly coupled to the motor response of the wings. While this coupling could reflect efferent copy or ascending reafferent sensory input to the DNg02 cells, the activation and silencing experiments indicate a causal relationship between DNg02 activity and motor output, although the role of feedforward and feedback mechanisms are not mutually exclusive.

In this chapter, we have demonstrated that the DNg02 neurons are required for the optomotor responses of the wings, head, abdomen, and legs to reach their full magnitude. Identification of the DNg02 neurons as an important component in the optomotor response provides a convenient entry point into a wide array of inquiries regarding the descending control of flight behavior in insects. In Chapter IV, we continue our investigation of the function of the DNg02 neurons in the optomotor response circuit, with particular attention to the downstream effects of these neurons on motor output.

Bibliography

[1] Richard A. Baines, Jay P. Uhler, Annemarie Thompson, Sean T. Sweeney, and Michael Bate. Altered electrical properties in drosophilaneurons developing without synaptic transmission. *Journal of Neuroscience*, 21(5):1523–1531, 2001.

[2] Tsevi Beatus, John M Guckenheimer, and Itai Cohen. Controlling roll perturbations in fruit flies. *Journal of The Royal Society Interface*, 12(105):20150075, 2015.

[3] Ruben Berthé and Fritz-Olaf Lehmann. Body appendages fine-tune posture and moments in freely manoeuvring fruit flies. *Journal of Experimental Biology*, 218(20):3295–3307, 2015.

[4] Seth A. Budick, Michael B. Reiser, and Michael H. Dickinson. The role of visual and mechanosensory cues in structuring forward flight in Drosophila melanogaster. *Journal of Experimental Biology*, 210(23):4092–4103, 2007.

[5] Tomás L. Cruz, Sebastián Malagón Pérez, and M. Eugenia Chiappe. Fast tuning of posture control by visual feedback underlies gaze stabilization in walking Drosophila. *Current Biology*, 31(20):4596–4607, 2021.

[6] Charles T. David. The relationship between body angle and flight speed in free-flying Drosophila. *Physiological Entomology*, 3(3):191–195, 1978.

[7] Bradley H. Dickerson, Alysha M. de Souza, Ainul Huda, and Michael H. Dickinson. Flies regulate wing motion via active control of a dual-function gyroscope. *Current Biology*, 29(20):3517–3524, 2019.

[8] Michael H. Dickinson and Florian T. Muijres. The aerodynamics and control of free flight manoeuvres in Drosophila. *Philosophical Transactions of the Royal Society B: Biological Sciences*, 371(1704):20150388, 2016.

[9] Brian J. Duistermars, Dawnis M. Chow, Michael Condro, and Mark A. Frye. The spatial, temporal and contrast properties of expansion and rotation flight optomotor responses in Drosophila. *Journal of Experimental Biology*, 210 (18):3218–3227, 2007.

[10] Brian J. Duistermars, Rachel A. Care, and Mark A. Frye. Binocular interactions underlying the classic optomotor responses of flying flies. *Frontiers in Behavioral Neuroscience*, 6:6, 2012.

[11] Charles Porter Ellington. The aerodynamics of hovering insect flight. VI. Lift and power requirements. *Philosophical Transactions of the Royal Society of London. B, Biological Sciences*, 305(1122):145–181, 1984.

[12] Michael J. Elzinga, William B. Dickson, and Michael H. Dickinson. The influence of sensory delay on the yaw dynamics of a flapping insect. *Journal of The Royal Society Interface*, 9(72):1685–1696, 2012.

[13] Mert Erginkaya and M. Eugenia Chiappe. Motion vision: Drosophila neural pathways that go with the visual flow. *Current Biology*, 32(16):R881–R883, 2022.

[14] Sawyer Buckminster Fuller, Andrew D. Straw, Martin Y. Peek, Richard M. Murray, and Michael H. Dickinson. Flying Drosophila stabilize their vision-based velocity controller by sensing wind with their antennae. *Proceedings of the National Academy of Sciences*, 111(13):E1182–E1191, 2014.

[15] Karl G. Götz. Course-control, metabolism and wing interference during ultralong tethered flight in Drosophila melanogaster. *Journal of Experimental Biology*, 128(1):35–46, 1987.

[16] Karl Georg Götz. Flight control in drosophila by visual perception of motion. *Kybernetik*, 4:199–208, 1968.

[17] Karl Georg Götz. Bewegungssehen und flugsteuerung bei der fliege drosophila. In *Symposium Physiology and Biophysics of Insect Flight 1982*, pages 21–34. Fischer, 1983.

[18] Karl Georg Götz, Bärbel Hengstenberg, and Roland Biesinger. Optomotor control of wing beat and body posture in Drosophila. *Biological Cybernetics*, 35:101–112, 1979.

[19] Väinö Haikala, Maximilian Joesch, Alexander Borst, and Alex S. Mauss. Optogenetic control of fly optomotor responses. *Journal of Neuroscience*, 33 (34):13927–13934, 2013.

[20] Roland Hengstenberg. Multisensory control in insect oculomotor systems. *Visual Motion and its Role in the Stabilization of Gaze*, pages 285–298, 1993.

[21] John S. Kennedy et al. The visual responses of flying mosquitoes. In *Proceedings of the Zoological Society of London*, volume 109. London, 1940.

[22] Holger G. Krapp, Barbel Hengstenberg, and Roland Hengstenberg. Dendritic structure and receptive-field organization of optic flow processing interneurons in the fly. *Journal of Neurophysiology*, 79(4):1902–1917, 1998.

[23] M.F. Land. Head movement of flies during visually guided flight. *Nature*, 243 (5405):299–300, 1973.

[24] Katherine J. Leitch, Francesca V. Ponce, William B. Dickson, Floris van Breugel, and Michael H. Dickinson. The long-distance flight behavior of Drosophila supports an agent-based model for wind-assisted dispersal in insects. *Proceedings of the National Academy of Sciences*, 118(17): e2013342118, 2021.

[25] Gaby Maimon, Andrew D. Straw, and Michael H. Dickinson. Active flight increases the gain of visual motion processing in Drosophila. *Nature Neuroscience*, 13(3):393–399, 2010.

[26] Akira Mamiya, Andrew D. Straw, Egill Tómasson, and Michael H. Dickinson. Active and passive antennal movements during visually guided steering in flying Drosophila. *Journal of Neuroscience*, 31(18):6900–6914, 2011.

[27] Alexander Mathis, Pranav Mamidanna, Kevin M. Cury, Taiga Abe, Venkatesh N. Murthy, Mackenzie Weygandt Mathis, and Matthias Bethge. Deeplabcut: Markerless pose estimation of user-defined body parts with deep learning. *Nature Neuroscience*, 21(9):1281–1289, 2018.

[28] Florian T. Muijres, Nicole A. Iwasaki, Michael J. Elzinga, Johan M. Melis, and Michael H. Dickinson. Flies compensate for unilateral wing damage through modular adjustments of wing and body kinematics. *Interface Focus*, 7(1): 20160103, 2017.

[29] Shigehiro Namiki, Michael H. Dickinson, Allan M. Wong, Wyatt Korff, and Gwyneth M. Card. The functional organization of descending sensory-motor pathways in Drosophila. *Elife*, 7:e34272, 2018.

[30] Shigehiro Namiki, Ivo G. Ros, Carmen Morrow, William J. Rowell, Gwyneth M. Card, Wyatt Korff, and Michael H. Dickinson. A population of descending neurons that regulates the flight motor of Drosophila. *Current Biology*, 32(5):1189–1196, 2022.

[31] Aljoscha Nern, Barret D. Pfeiffer, and Gerald M. Rubin. Optimized tools for multicolor stochastic labeling reveal diverse stereotyped cell arrangements in the fly visual system. *Proceedings of the National Academy of Sciences*, 112 (22):E2967–E2976, 2015.

[32] Lina Ni. Genetic transsynaptic techniques for mapping neural circuits in Drosophila. *Frontiers in Neural Circuits*, page 104, 2021.

[33] Leif Ristroph, Attila J. Bergou, Gunnar Ristroph, Katherine Coumes, Gordon J. Berman, John Guckenheimer, Z. Jane Wang, and Itai Cohen. Discovering the flight autostabilizer of fruit flies by inducing aerial stumbles. *Proceedings of the National Academy of Sciences*, 107(11):4820–4824, 2010.

[34] C. Schilstra and J.H. Van Hateren. Stabilizing gaze in flying blowflies. *Nature*, 395(6703):654–654, 1998.

[35] Bettina Schnell, Peter T. Weir, Eatai Roth, Adrienne L. Fairhall, and Michael H. Dickinson. Cellular mechanisms for integral feedback in visually guided behavior. *Proceedings of the National Academy of Sciences*, 111(15):5700–5705, 2014.

[36] Julie H. Simpson and Loren L. Looger. Functional imaging and optogenetics in Drosophila. *Genetics*, 208(4):1291–1309, 2018.

[37] Mustafa Talay, Ethan B. Richman, Nathaniel J. Snell, Griffin G. Hartmann, John D. Fisher, Altar Sorkaç, Juan F. Santoyo, Cambria Chou-Freed, Nived Nair, Mark Johnson, et al. Transsynaptic mapping of second-order taste neurons in flies by trans-Tango. *Neuron*, 96(4):783–795, 2017.

[38] Lance F. Tammero, Mark A. Frye, and Michael H. Dickinson. Spatial organization of visuomotor reflexes in Drosophila. *Journal of Experimental Biology*, 207(1):113–122, 2004.

[39] H. Wagner. Flight performance and visual control of flight of the free-flying housefly (Musca domestical L.) III. Interactions between angular movement induced by wide- and smallfield stimuli. *Philosophical Transactions of the Royal Society of London. B, Biological Sciences*, 312(1158):581–595, 1986.

[40] Samuel C. Whitehead, Tsevi Beatus, Luca Canale, and Itai Cohen. Pitch perfect: How fruit flies control their body pitch angle. *Journal of Experimental Biology*, 218(21):3508–3519, 2015.

[41] Johannes M. Zanker. How does lateral abdomen deflection contribute to flight control of Drosophila melanogaster? *Journal of Comparative Physiology A*, 162(5):581–588, 1988.

[42] Yan Zhang, Márton Rózsa, Yajie Liang, Daniel Bushey, Ziqiang Wei, Jihong Zheng, Daniel Reep, Gerard Joey Broussard, Arthur Tsang, Getahun Tsegaye, et al. Fast and sensitive gcamp calcium indicators for imaging neural populations. *Biorxiv*, pages 2021–11, 2021.

Chapter 4

THE FUNCTIONAL ROLE AND DOWNSTREAM CONNECTIVITY OF THE DNG02S

Emily H. Palmer, Jaison J. Omoto, and Michael H. Dickinson. The role of a population of descending neurons in the optomotor response in flying *Drosophila*. *bioRxiv*, 2022. doi: https://doi.org/10.1101/2022.12.05.519224.
E.H.P. and J.J.O performed all experiments under the supervision of M.H.D. E.H.P. developed the computational models. E.H.P. and J.J.O. analyzed data and prepared all figures. E.H.P., J.J.O., and M.H.D. wrote the paper.

4.1 Abstract

In Chapter III, a population of descending neurons, the DNg02s, was shown to be required for the optomotor response to reach its full magnitude, and DNg02 activity was shown to correlate strongly with contralateral wingbeat amplitude. Here, we investigate the downstream effects of the DNg02s on the motor system through a combination of unilateral DNg02 activation and modeling. Whereas the previous work may have implied asymmetric connectivity from the DNg02s to the motor neurons, unilateral optogenetic activation of DNg02 neurons does not elicit the asymmetric changes in wing motion characteristic of the optomotor response to a visual stimulus, but rather generates bilaterally symmetric increases in wingbeat amplitude. We interpret our experiments to suggest that flight maneuvers in flies require a more nuanced coordination of power muscles and steering muscles than previously appreciated, and that the physical flight apparatus of a fly might permit mechanical power to be distributed differentially between the two wings. Thus, whereas our experiments identify the DNg02 cells as a critical component of the optomotor reflex, our results suggest that other classes of descending cells targeting the steering muscle motor neurons are also required for the behavior.

4.2 Introduction

The motor output induced by patterns of wide-field optic flow has been extensively studied, including a detailed description of the responses in flight muscles. The flight muscles of flies are functionally stratified into two systems that collectively power and regulate wing motion [4]. The first system consists of large asynchronous muscles that provide the power to flap the wings at high frequency. These stretch-

activated muscles [12, 24] insert on the walls of the thorax in an approximately orthogonal arrangement, creating a self-oscillatory system that drives the back and forth motion of the wings. Dorsal longitudinal muscles (DLMs) contract to move the wing forward while stretching and activating dorso-ventral muscles (DVMs), which subsequently drive the wings backward while stretching the DLMs to continue the cycle. The oscillations of the power muscles are transmitted to the wings via their action on two critical mechanical inputs to the wing hinge: the scutellar lever arm and the anterior notal wing process [1, 3, 19, 23]. The second system consists of tiny synchronous steering muscles that actuate subtle changes in wing kinematics by directly reconfiguring the wing hinge [6, 9, 10, 15]. Whereas this prior work has highlighted the important role of steering muscles in generating the asymmetries in wing motion necessary for the optomotor response, the power muscles are generally thought to operate in a bilaterally symmetric fashion because the scutellar lever arms are mechanically coupled across the two sides of the fly [1, 3, 23, 30]. However, bilaterally asymmetric Ca^{2+} signals recorded from the power muscles during presentation of visual yaw stimuli suggest that they, too, might play a role in the optomotor response [14]; recent unpublished experiments recording from the muscles electrophysiologically while presenting optomotor stimuli support this result [2]. Thus, the changes in wing motion during optomotor reflexes could involve a coordination of both power and steering muscle activity. Such coordination is not unexpected, given that the power requirements to flap a wing depend on the torque that it generates [7], which must change during the optomotor response. The question remains, however, whether there is enough flexibility in the mechanical structures linking the scutellar level arms and anterior notal wing processes on the two sides of the fly such that asymmetric activity in the power muscles could generate differential drive to the left and right wing hinges.

In Chapter III, we demonstrated that the DNg02 neurons are required for the optomotor response, insofar as silencing subsets of the population reduces the magnitude of the response in proportion to the number of cells silenced. These results, taken with prior work [21] suggesting that the DNg02 neurons increase the total mechanical power output of the flight system, imply that the DNg02 neurons influence the motor output of the fly via their influence over the power muscles; we investigated this hypothesis by estimating the power production during the optomotor response. When DNg02 neurons are silenced, the magnitudes of both the bilaterally asymmetry and the bilateral sum of power production are reduced, supporting the hypothesis that the cells provide input to the power muscles MNs. Further, two-photon func-

tional imaging experiments supported previously reported results [21] indicating a tight correlation between DNg02 activity and contralateral wingbeat amplitude. However, when we performed unilateral activation of the neurons, we found that this manipulation does not elicit turning responses; rather, we observed bilaterally symmetric increases in wingbeat amplitude upon unilateral activation. The results suggest that the DNg02s are necessary but not sufficient for turning responses, indicating that additional pathways are likely involved in the optomotor response, perhaps involving DNs that make strong connections to steering muscle motor neurons. We construct a series of models to test the connectivity of the DNg02 and other potential descending pathways in the optomotor response. Our results thus support the hypothesis that the optomotor response involves a complex coordination of both power and steering muscle activity, underscoring the sophisticated nature of the insect wing hinge and its control.

4.3 Results

Modeling power output during the optomotor response

Namiki and coworkers [21] showed that DNg02 activation increases the total mechanical power output of the flight system, suggesting that these neurons provide a strong drive to the motor neurons of the asynchronous power muscles. To investigate the changes in power production during the optomotor response, we made use of a series of equations derived by Ellington in the early 1980s to estimate power production [7]. The muscle mass specific power (P^*) is estimated from the induced power (P^*_{ind}, the power necessary to maintain enough lift to stay aloft), the profile power (P^*_{pro}, the power necessary to overcome drag on the wing as it beats back and forth), and the inertial power (P^*_{acc}, the power necessary to overcome drag on the wing as it beats back and forth):

$$P^* = \frac{1}{2}[(P^*_{\text{ind}} + P^*_{\text{pro}} + (1-\alpha)P^*_{\text{acc}}) + R(P^*_{\text{ind}} + P^*_{\text{pro}} - (1-\alpha)P^*_{\text{acc}})], \tag{4.1}$$

where R is a rectification function such that $R(x < 0) = 0$. The induced, profile, and inertial powers can be estimated as

$$P^*_{\text{ind}} = \kappa \left(\frac{F_t}{2m_M}\right)\left(\frac{F_t}{2\rho\Phi R^2}\right)^{1/2} \tag{4.2}$$

$$P^*_{\text{pro}} = \frac{\rho S f^3 \Phi^3 R^3 \hat{r}_3^3(S)\overline{|d\hat{\phi}/d\hat{t}|^3}}{32 m_M}\overline{C_{\text{D,pro}}} \tag{4.3}$$

$$P^*_{\text{acc}} = \frac{\rho S f^3 \Phi^2 R^3 (d\hat{\phi}/d\hat{t})^2_{\text{max}}}{4 m_M}\left(\frac{\rho_{\text{W}}}{\rho}\hat{h}\hat{r}_2^2(m) + \frac{\pi S \hat{v}\hat{r}_2^2(v)}{8R^2}\right), \tag{4.4}$$

with the mean profile drag coefficient, $\overline{C_{\mathrm{D,pro}}}$, calculated as

$$\overline{C_{\mathrm{D,pro}}} = \frac{7}{Re^{1/2}} \tag{4.5}$$

$$= \frac{7}{(\frac{S}{\nu} n \Phi)^{1/2}}, \tag{4.6}$$

where Re is the Reynolds number of the flapping wing, Φ is the wingbeat amplitude in radians, and f is the wingbeat frequency in Hz; the other parameters are given in Table 4.1.

Symbol	Parameter	Value	Reference
κ	Rankine-Froude correction factor	1.28	[13]
F_t	Total flight force (N)	11×10^{-6}	[13]
m_M	Muscle mass (kg)	3.15×10^{-7}	[13]
ρ	Density of air (kg/m^3)	1.2	
R	Wing length (m)	2.47×10^{-3}	[13]
S	Wing area (m^2)	3.95×10^{-6}	[13]
$\hat{r}_3^3(S)$	Third moment of wing area	0.242	[13]
$\overline{\lvert d\hat{\phi}/d\hat{t}\rvert^3}$	Mean cube of dimensionless angular velocity	104.5	[13]
$(d\hat{\phi}/d\hat{t})^2_{\mathrm{max}}$	Square of max dimensionless angular velocity	30.3	[13]
ρ_{W}	Wing density (kg/m^3)	1200	[13]
$\hat{h}$	Dimensionless wing thickness	5.4×10^{-4}	[13]
$\hat{r}_2^2(m)$	Second moment of wing mass	0.345	[13]
$\hat{\nu}$	Dimensionless virtual mass	1.146	[13]
$\hat{r}_2^2(\nu)$	Second moment of wing virtual mass	0.342	[13]
α	Elastic storage in the thorax	0.11	[5]

Table 4.1: Parameters used in estimating power of each wing during optomotor response.

We applied these equations to the optomotor response data presented in Figures 3.2 and 3.8. During the optomotor response, the power output of the wing decreasing in amplitude decreases (Figure 4.1A) and the power output of the wing increasing in amplitude increases (Figure 4.1B). While this may seem like an intuitive result, the power production is nonlinearly dependent on frequency; strong changes in wingbeat frequency could cause both wings to increase or decrease in power production, even though one increases in amplitude and the other decreases. Instead, the observed changes in power output during the optomotor response are consistent with both intuition and prior work [14].

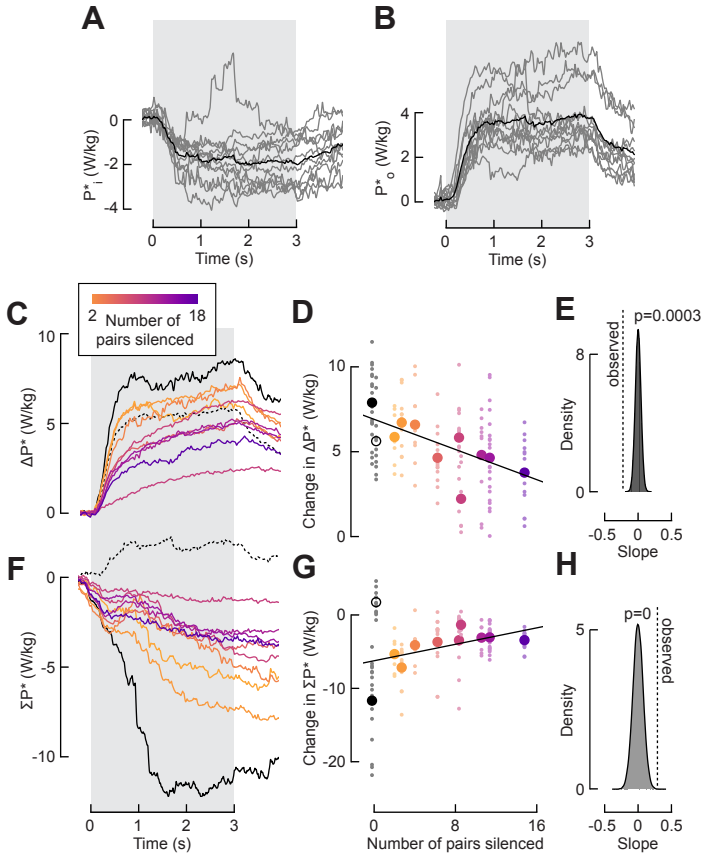

Figure 4.1: Silencing DNg02 neurons alters power production during the optomotor response.
(A) Estimated change in power production of the inside wing relative to the direction of the optomotor stimuli, using data from Figure 3.2.
(B) Estimated change in power production of the outside wing relative to the direction of the optomotor stimuli, using data from Figure 3.2.
(C) Estimated differential in power production between the two wings for flies with DNg02 neurons silenced with Kir2.1 (sample sizes throughout figure: empty-split vector control: n = 19; wild-type control: n = 12; SS02634: n = 7; SS02627: n = 14; SS01577: n = 10; SS02535: n = 14; SS01578: n = 14; SS01563: n = 7; SS02625: n = 23; SS02624: n = 10; SS02630: n = 14). The number of pairs of cells silenced is indicated by the color of the trace, with the fewest pairs in yellow and the most in purple. The response of empty-vector control flies (SS03500) is shown with a solid, black line and the response of wild-type control flies is shown with a dotted, black line. The period of stimulus presentation is shown by the gray patch. Data from Figure 3.8.
(D) Change in ΔP^* plotted against the number of DNg02 pairs silenced. As in (A), the number of pairs silenced is indicated by color. The two controls are offset slightly for visual clarity; the empty vector control is indicated by a solid circle and the wild-type control is indicated by an empty circle. Individual fly means are shown with small circles and grand means for a given driver line is shown with a large circle. A line is fit to individual fly means and plotted in black ($r^2 = 0.49$, based on mean values).
(E) Distribution of 100,000 bootstrapped slopes of lines of best fit with responses and numbers of cells silenced randomly sampled with replacement. The dotted, black line indicates the observed slope of the original dataset. The p-value is the proportion of resampled slopes that result in a more extreme slope than observed.
(F) As in (C), for power sum.
(G) As in (D), for power sum ($r^2 = 0.10$, based on mean values).
(H) As in (E), for power sum.

To test whether the DNg02 population regulates power production, we estimated the power production during the optomotor response when the DNg02 neurons were silenced, drawing from the data presented in Figure 3.8. Much like the magnitude of the wingbeat amplitude response to optomotor stimuli is reduced when DNg02 neurons are silenced, so too was the asymmetry in power production ($\Delta P^* = P^*_o - P^*_i$) diminished (Figure 4.1C-E). During the optomotor response, there tended to be a reduction in the total power output ($\Sigma P^* = P^*_o + P^*_i$); this reduction in total power was also inhibited by silencing the DNg02s (Figure 4.1F-H). This result supports the hypothesis that the DNg02 neurons provide input to the power muscle motor neurons, as silencing the DNg02 neurons inhibits the ability of the motor system to modulate power production during the optomotor response.

Unilateral DNg02 activation induces bilaterally symmetric wing responses.

Both the silencing screen and the two-photon functional imaging results are consistent with the hypothesis that DNg02 neurons regulate contralateral wingbeat amplitude. If so, unilateral DNg02 activation should induce strong steering maneuvers, in which the contralateral wing increases its amplitude upon activation, and the ipsilateral wingbeat amplitude either decreases (in the case in which DNg02 neurons inhibit motor output on the ipsilateral side) or does not change (in the case in which DNg02 neurons have effect on ipsilateral wing motion). To test this hypothesis, we targeted optogenetic stimulation of DNg02 neurons on one side of the central nervous system (CNS) via a genetic strategy used previously for lobula columnar neurons [31]. This approach leverages the modular organization of insect nervous systems; neurons of the CNS descend from individual neural progenitors called neuroblasts, each of which produces a unique lineage of developmentally related cells [27]. Using this technique, we could create animals expressing Chrimson-Venus in DNg02 neurons unilaterally (Figure 4.2A); we also generated animals with bilateral or no labeling (Figure 4.2B-C), providing useful controls with identical genetic backgrounds and experimental rearing conditions. We scored the expression pattern in the brain of each fly after the conclusion of an experiment.

Upon activation, flies with cells labeled bilaterally exhibit strong increases in the bilateral mean of wingbeat amplitude, consistent with previous experiments [21] (Figure 4.2E, G). Control flies in which no cells expressed CsChrimson exhibited no changes in mean WBA, at least for stimulus duration less than 300 ms (Fig 4.2F, G). At longer stimulus durations, control flies did show small increases in mean WBA, which we interpret to be an artifact induced either by a behavioral response to the

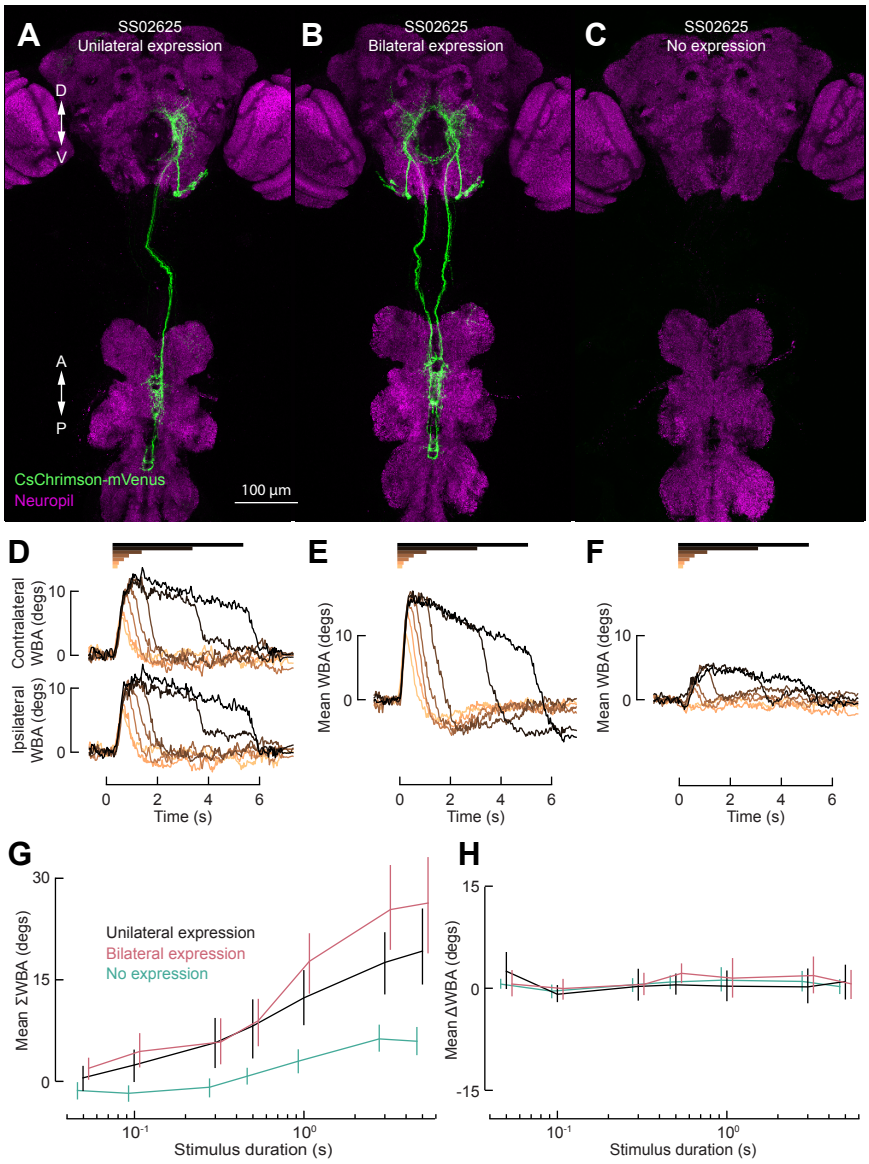

Figure 4.2: Unilateral DNg02 activation induces bilaterally symmetric changes to wing kinematics.
(A-C) Confocal z-projections of the fly central nervous system. Flp-recombinase under heat shock control coupled with 20XUAS-FRT>-dSTOP-FRT>-CsChrimson-mVenus enables temperature dependent, stochastic expression of CsChrimson-Venus (green) in DNg02 neurons unilaterally (A), bilaterally (B), or neither (C). Magenta: nc82.
(D) Baseline-subtracted contralateral and ipsilateral WBA responses of flies with unilateral expression of CsChrimson to a red light stimulus of variable duration (0.05, 0.1, 0.3, 0.5, 1, 3, or 5 s, indicated by the horizontal bars above) (n = 8 flies). Flies are presented with a grating visual pattern in closed loop with their left minus right WBA.
(E) Baseline-subtracted mean WBA responses of flies with bilateral expression of CsChrimson (n = 14 flies). Plotting conventions as in (D).
(F) As in (E), for flies with no expression of CsChrimson (n = 23 flies).
(G) Mean ΣWBA against duration of stimulus. Expression pattern is indicated by color, with unilateral expression in black, bilateral in pink, and no expression in green. Vertical bars indicate a bootstrapped 95% CI. Bilateral and no expression traces are offset slightly for visual clarity.
(H) As in (G), for ΔWBA.

617 nm light or the heat it generated. In the case of unilateral DNg02 activation, we expected to observe a strong decrease in ΔWBA (here, ipsilateral – contralateral WBA) in response due to an increase in wingbeat amplitude on the side contralateral to the stimulated cells. In contrast, however, we observed comparable increases in both contralateral and ipsilateral wingbeat amplitude and thus a large mean WBA response (Figure 4.2D, G). Further, in all three cases (unilateral, bilateral, or no activation), the ΔWBA response was very close to zero in response to activation regardless of stimulus duration (Figure 4.2H); thus, wing kinematics remained bilaterally symmetric regardless of whether the activation was symmetric or asymmetric. The only difference between unilateral and bilateral activation was that the resulting mean WBA response was higher with bilateral activation (Figure 4.2G), which is consistent with more cells being activated under that condition (i.e., the DNg02 neurons on both the left and right sides of the brain are activated). We repeated the experiments at lower stimulus durations and across different driver lines and found the same result: regardless of stimulus duration or number of cells labeled, the resulting behavior was a bilaterally symmetric increase in wingbeat amplitude (Figure 4.3). These results suggest that unilateral optogenetic recruitment of DNg02 activity drives bilaterally symmetric motor output, although the precise mechanism (e.g., reciprocal connectivity within the population, symmetric bilateral downstream connectivity to motor neurons) is unknown.

4.4 Modeling the connectivity of flight control

Given the result of our silencing and functional imaging experiments, it is noteworthy that unilateral optogenetic activation of DNg02 neurons did not elicit bilaterally asymmetric changes in wing motion similar to those elicited by a visual yaws stimulus, but rather evoked symmetric increases in wingbeat amplitude comparable to those elicited by bilateral activation. Whereas the silencing and functional imaging experiments suggest that DNg02 neurons regulate contralateral wingbeat amplitudes via population coding, the unilateral activation results do not support this hypothesis. We sought to resolve this discrepancy by developing models of the connectivity underlying the optomotor response circuit.

There are several possible explanations for the observed discrepancy, which are not mutually exclusive and all of which assume that the DNg02 neurons provide strong input to the power muscle motor neurons. The conflicting models tested whether the structure of the connectivity from the DNg02 neurons to the power muscle motor neurons was symmetric or asymmetric; the silencing and functional imaging exper-

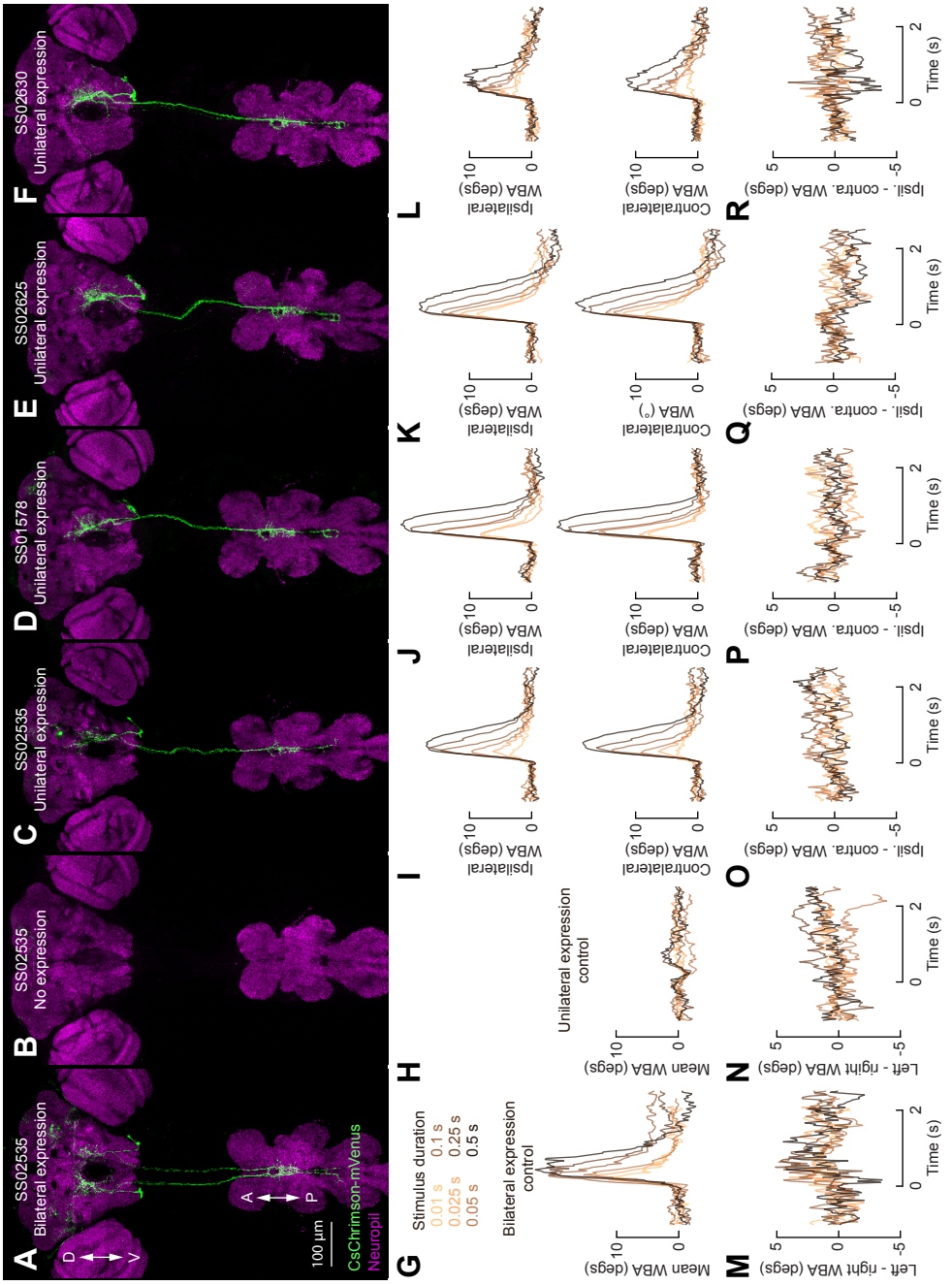

Figure 4.3: Unilateral DNg02 activation induces bilaterally symmetric wing responses at short stimulus durations and across driver lines.
(A-F) As in Figure 4.2A-C for DNg02 neurons bilaterally for SS02535 (A), on neither side for SS02535 (B), or unilaterally for SS02535 (C), SS01578 (D), SS02625 (E), and SS02630 (F).
(G) Baseline-subtracted mean WBA responses of flies (SS02535) with bilateral expression of CsChrimson to a red light stimulus of variable duration (0.01, 0.025, 0.05, 0.1, 0.25, or 0.5 s) (n = 6 flies). Flies were presented with a visual grating pattern in closed loop.
(H) As in Figure (G), for flies (SS02535) with no expression of CsChrimson (n = 16 flies).
(I) Baseline-subtracted contralateral and ipsilateral WBA responses of flies (SS02535) with unilateral expression of CsChrimson (n = 15 flies). Plotting conventions as in Figure (G).
(J-L) As in Figure (I), for SS01578 (n = 12 flies), SS02625 (n = 14 flies), and SS02630 (n = 8 flies), respectively.
(M) Mean WBA differential for the data in (G). Plotting conventions as in Figure S7G.
(N) Mean WBA differential for the data in (H).
(O-R) Ipsilateral minus contralateral differential for the data in (I-R), respectively.

iments would suggest asymmetrical connectivity, whereas the unilateral activation experiments would suggest symmetrical connectivity. The underlying structure of both models is shown in Figure 4.4A. As described in the Introduction, two distinct types of flight muscles regulate wing motion in flies: large asynchronous power muscles, which provide power to the wings indirectly via their action on the scutellar lever arm and the anterior notal wing process [1, 3], and the tiny synchronous steering muscles, which generate subtle changes in wingbeat kinematics via their direct insertions on elements within the wing hinge [6, 14, 15]. It is quite possible that both muscle systems are involved in the optomotor response, because sustained changes in wing motion require regulation both of power output and wing kinematics. We schematize the motor system using the analog of a lever arm with an adjustable fulcrum. The power muscles provide the power to move the lever arm, with the wing on the opposite side of the fulcrum from the power muscles. The steering muscles act by moving the adjustable fulcrum. Each set of muscles receives input from a set of motor neurons (MNs). The power muscles MNs receive input from the DNg02 neurons. Other DNs may also provide input to the power muscle MNs, as well as the steering muscle MNs. The possible influence of the DNg02s over the steering muscle motor neurons has not yet been investigated and is therefore not included in the models. All DNs receive input from visual projection neurons in the brain; other upstream sensory input (e.g., mechanosensory input to the antenna) is not shown, as the behavior of the DNg02 neurons in response to other sensory modalities was not tested. The MNs also receive mechanosensory feedback from the wings and the halteres, a set of biomechanical structures that beat in antiphase to the wings to provide gyroscopic sensory input and regulate the timing of the wingstrokes.

Model I: Asymmetrical connectivity

Our first model posits that the connectivity from the DNg02 neurons to the power muscle MNs is asymmetrical (Figure 4.4B), and that the symmetrical wing kinematics observed during unilateral activation are the result of reciprocal connectivity, biomechanical pairing, and/or sensory feedback within the DNg02 population:

- If the **reciprocal connectivity** within the DNg02 population identified by our trans-Tango experiments includes connections among DNg02 cells on the left and right side of the body, unilateral activation might recruit other members of the population across the midline. Unfortunately, our trans-Tango results do not distinguish between ipsilateral and contralateral connections, so we

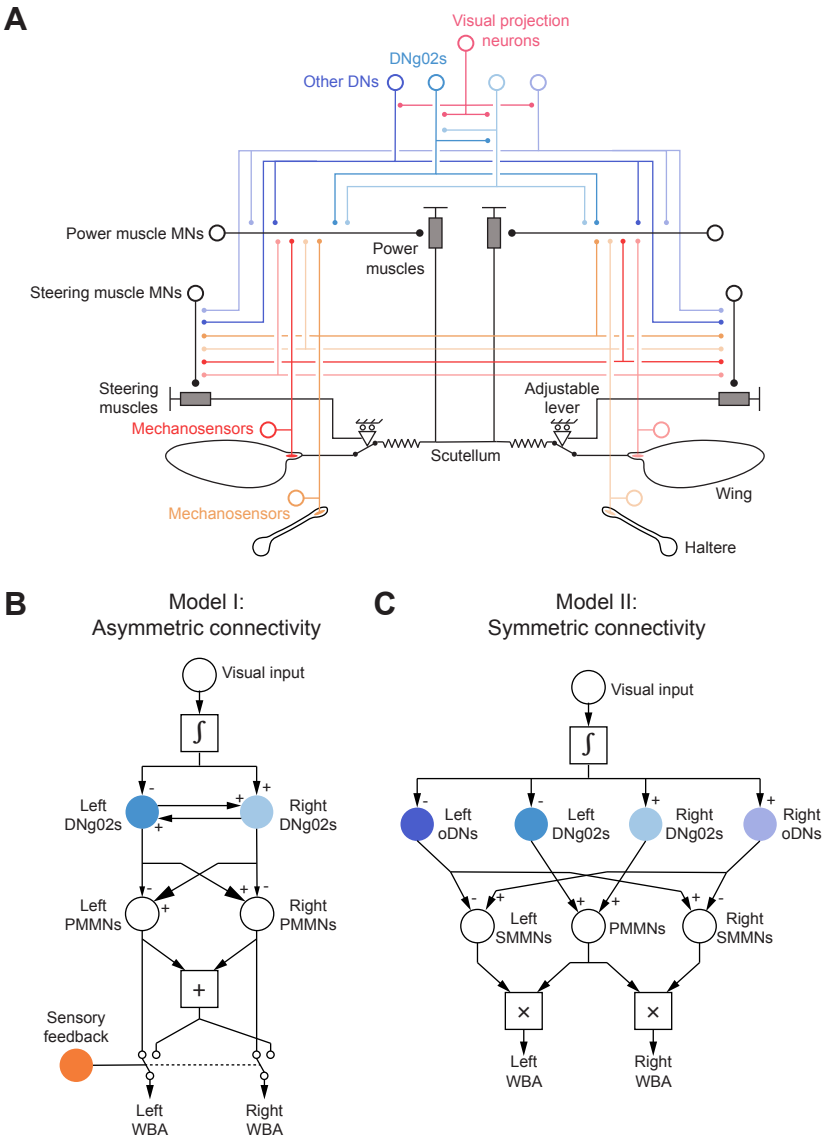

Figure 4.4: Schematic summary of neural connectivity and biomechanical structures underlying flight control. (A) Schematic representation of structure underlying both models. Neurons are indicated by a large open circle (the cell body) connected by a line to a small filled circle (output terminals); mechanosensory neuron inputs are shown by filled ovals. Muscles are shown with gray boxes. Power muscles drive wing motion via the scutellum (black springs). The steering muscles effect small changes in wing kinematics by moving the fulcrum of the lever driving the wing motion. Each set of muscles is driven by motor neurons (MNs, black); the power muscles are driven by the power muscle MNs and the steering muscles by the steering muscle MNs. The DNg02 neurons (light blue) provide input to the power muscles MNs. Other DNs (dark blue) provide input to the steering muscles MNs and, possibly, the power muscle MNs. All DNs receive input from visual projection neurons encoding the patterns of wide-field optic flow observed during the optomotor response (pink). All muscle MNs receive mechanosensory feedback from the wings (red) and halteres (orange).
(B) Diagram representing Model I: Asymmetric connectivity from DNg02 neurons to power muscle motor neurons (PMMNs). DNg02 neurons receive visual information from visual centers in the brain via a leaky integrator and provide asymmetric input to the PMMNs, as indicated by arrow sizes. WBA is the direct output of the corresponding PMMN, given that appropriate sensory input is provided to the system. Otherwise, motor output is forced to be symmetric.
(C) Diagram representing Model II: Symmetric connectivity from DNg02 neurons to PMMNs. DNg02 neurons and other DNs (oDNs) all recieve input from visual centers as in (B). oDNs provide input to steering muscle motor neurons (SMMNs); DNg02s provide symmetric input to PMMNs. WBA is the product of the PMMN activity and the activity of the ipsilateral SMMN.

are not able to further evaluate this possibility. The fact that the DNg02 cells do display bilaterally asymmetric responses when presented with visual yaw motion (Figure 3.15), would suggest that the coupling among the cells is not so strong so as to lock bilateral pairs of neurons within the population to the same level of activity.

- Second, **biomechanical pairing** within the thorax may enforce bilateral symmetry in wing motion. In particular, the forces generated by the power muscles to drive the wing back and forth are transmitted to the wings via the scutellum, a relatively rigid biomechanical structure. Its rigidity has been shown to enforce bilaterally symmetric wing motion; if it is cut, for example, the wings are able to beat out of phase with each other, which is impossible in intact flies [3].

- Finally, mechanosensory and visual **sensory feedback** from the wings, halteres, and eyes may also enforce bilaterally symmetric wing motion. When the fly is not attempting a voluntary turn (i.e., the fly is not attempting to move its wings asymmetrically), symmetric sensory input from these systems may preclude bilaterally asymmetric wing kinematics. That is to say, if the animal is not experiencing the sensory feedback associated with turning and it is not attempting to turn, the control system may act sufficiently strongly in opposition to turning that asymmetrical input from the DNg02 neurons is insufficient to induce asymmetrical wing kinematics.

Under this hypothesis, it is also possible that to induce asymmetric motor output, DNg02 activity must be in opposition across the midline such that cells on one side increase in activity while those on the other side decrease in activity. This is distinct from our unilateral activation experiments, wherein cells on one side where activated and no effect was induced in cells on the other side by experimenters. The large change in the level of activity at the onset of flight (Figure 3.15C) is relevant to this hypothesis, because it indicates that the neurons might encode visual motion via both increases and decreases in changes in the background level of activity. Indeed, the interpretation of unilateral DNg02 activation is unclear given our functional imaging experiments, as we never recorded increases in cell activity on one side with no changes on the other side of the brain during our functional imaging experiments (Figure 3.15D). We did observe decreases in activity on one side and no changes on the other, but we are unable to elicit this pattern of activity via optogenetic methods. Although optogenetic silencing channels are available

[20], preliminary experiments indicated that the strong behavioral artifacts elicited in flying flies by the presentation of the blue light required for GtACR activation render the results uninterpretable.

The model recapitulated the neuronal and behavioral responses elicited by the presentation of optomotor stimuli (Figures 4.5, top left and 4.6). Upon presentation of yaw right stimuli, the left DNg02s decreased in activity and the right DNg02s increased, and vice versa for yaw left stimuli, in accordance with the functional imaging experiments (Figures 3.15 and 3.17). These changes in simulated DNg02 activity elicited changes in power muscle MN activity, with strong positive connections between DNg02s and contralateral MNs. Thus, when yaw right stimuli is presented, DNg02 neurons on the right side of the body and PMMNs on the left side of the body increase in activity, DNg02s and PMMNs on the left and right, respectively, decrease, and vice versa for yaw left. Since the model is receiving sensory feedback, the WBA of each wing is simply the output of the corresponding PMMNs; thus, the model results in same DNg02 neuronal activity and motor output as observed in experiments with real flies.

We further tested whether the model could recapitulate the reduction in the magnitude of the wing optomotor response caused by silencing the DNg02 neurons (Figure 3.8) by varying the degree to which the fictive neurons could be recruited (Figure 4.6). When the simulated DNg02 population was inhibited, the magnitude of the change in ΔWBA during the optomotor response was reduced, as in the experiments with DNg02 neurons silenced (Figure 3.8). The model therefore recapitulated both the neuronal responses observed in the functional imaging experiments and the behavioral responses observed in the silencing experiments.

Finally, we tested whether the model could recapitulate the observation that unilateral DNg02 activation results in bilaterally symmetric wing kinematics by providing elevated input only to DNg02 neurons on one side of the body (Figures 4.5, bottom left and 4.7). Because of the reciprocal connectivity in the model, asymmetrical activation on one side induced weak increases in activity on the other side of the body. These changes induced asymmetric activity in the PMMNs. However, since these changes are induced by optogenetic activation rather than sensory stimuli, the wing control system forced the wing kinematics to be symmetric; as indicated in Figure 4.5, bottom left by the switch mechanism. The modelled wings therefore responded to unilateral activation with bilaterally symmetrical wing motion, with no change to ΔWBA, but a strong increase to ΣWBA (Figure 4.7), in accordance with the observed responses in real flies (Figure 4.2). These result indicates that

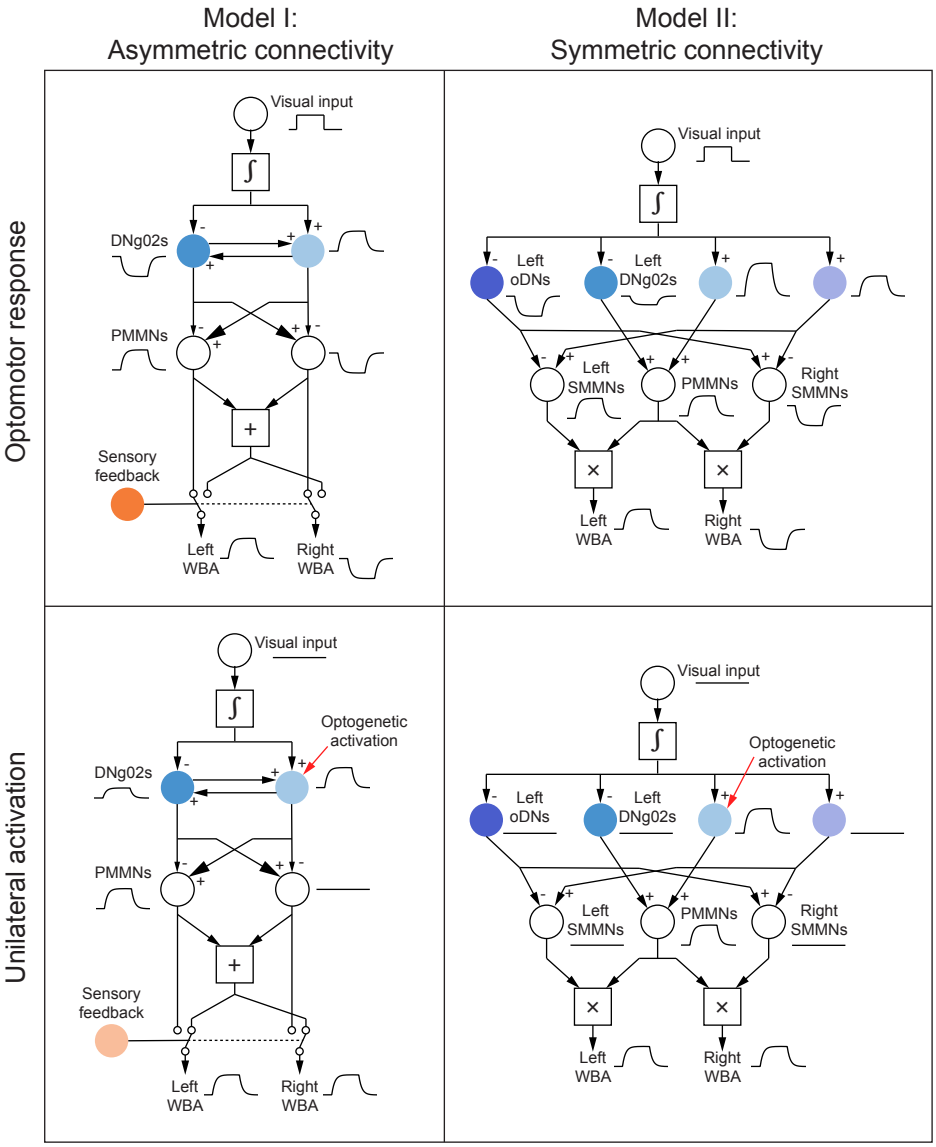

Figure 4.5: Schematic demonstration of responses of Models I and II to optomotor visual stimuli and unilateral optogenetic activation. Hypothesized parameter activity is indicated to the right of the given parameter (e.g., DNg02 activity is indicated next to the schematic DNg02 neuron). See text and methods for details on implementation.

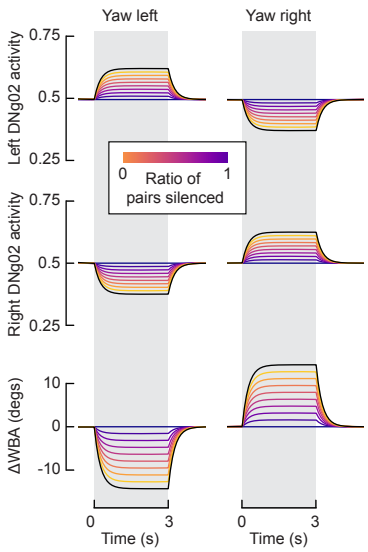

Figure 4.6: Asymmetrical connectivity model recapitulates silencing data. To simulate silencing DNg02 neurons, η, the parameter governing the ratio of DNg02 neurons silenced, is varied from 0 to 1 (indicated by colormap, with no cells silenced shown in black). Top and middle rows show DNg02 activity in response to stimuli; bottom row shows simulated ΔWBA. Plotting conventions as in Figure 3.8A).

Model I, which assumes asymmetric connectivity from the DNg02 neurons to the power muscle MNs, can fully recapitulate the observed data.

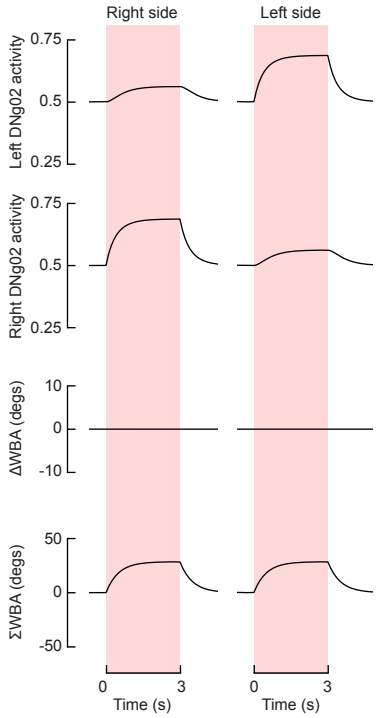

Figure 4.7: Asymmetrical connectivity model recapitulates behavioral responses to unilateral activation.

Model II: Symmetrical connectivity

While the estimated power required to move each wing is asymmetric during the optomotor response (Figure 4.1), the scutellar lever arm and anterior notal wing processes mechanically link the wings. Given this mechanical linkage, is it even possible for the DLMs and DVMs to deliver different amounts of mechanical power to the two wings? With this question in mind, we constructed an alternative hypothesis, in which the DNg02 neurons project symmetrically to the flight motor neurons on the contralateral and ipsilateral side, such that the DNg02 neurons serve to regulate the total power produced by the power muscles. Under this hypothesis, other parallel DN (oDN) pathways are required to generate bilaterally asymmetric wing motions, as DNg02 activity will always result in symmetric wing kinematics (Figure 4.4C).

In this model, when optomotor stimuli were presented to the simulated fly, all DNs on each side of the body respond as observed in the DNg02 during the functional imaging experiments (Figure 3.17). For example, when yaw right motion was presented, DNs (i.e., DNg02s and oDNs) on the right side of the body increase in activity and DNs on the left decrease (Figure 4.5, top right and 4.8A). The DNg02s all synapse onto a single population of PMMNs (thus, the model simulates symmetrical connectivity from DNg02s to the MNs), while the oDNs provided asymmetrical input to steering muscle (SM) MNs. Both PMs and SMs are required for the wing motion observed during the optomotor response. Here, we calculated the wing motion simply as the product of the activities of the PMMNs and SMMNs, and thus recapitulate the wing motion observed in real flies. As in Model I, when the simulated DNg02 neurons were silenced, we observed a reduction in the magnitude of the optomotor response (Figure 4.8A). Model II therefore recapitulates the phenomenology observed in the functional imaging and silencing experiments.

Upon unilateral activation of the DNg02 neurons, we observed increases in PMMN activity and no changes to the activity of all other DNs and SMMNs (Figure 4.5, bottom right and 4.8B). Since the PMMNs increased in activity and there was no asymmetrical activity in the SMMNs, unilateral activation induced symmetrical increases in WBA, as in the unilateral activation experiments. Thus, Model II, much like Model I, can recapitulate all the observed data.

The symmetrical connectivity model (Model II) differs from the asymmetrical connectivity model (Model I) in a number of notable ways:

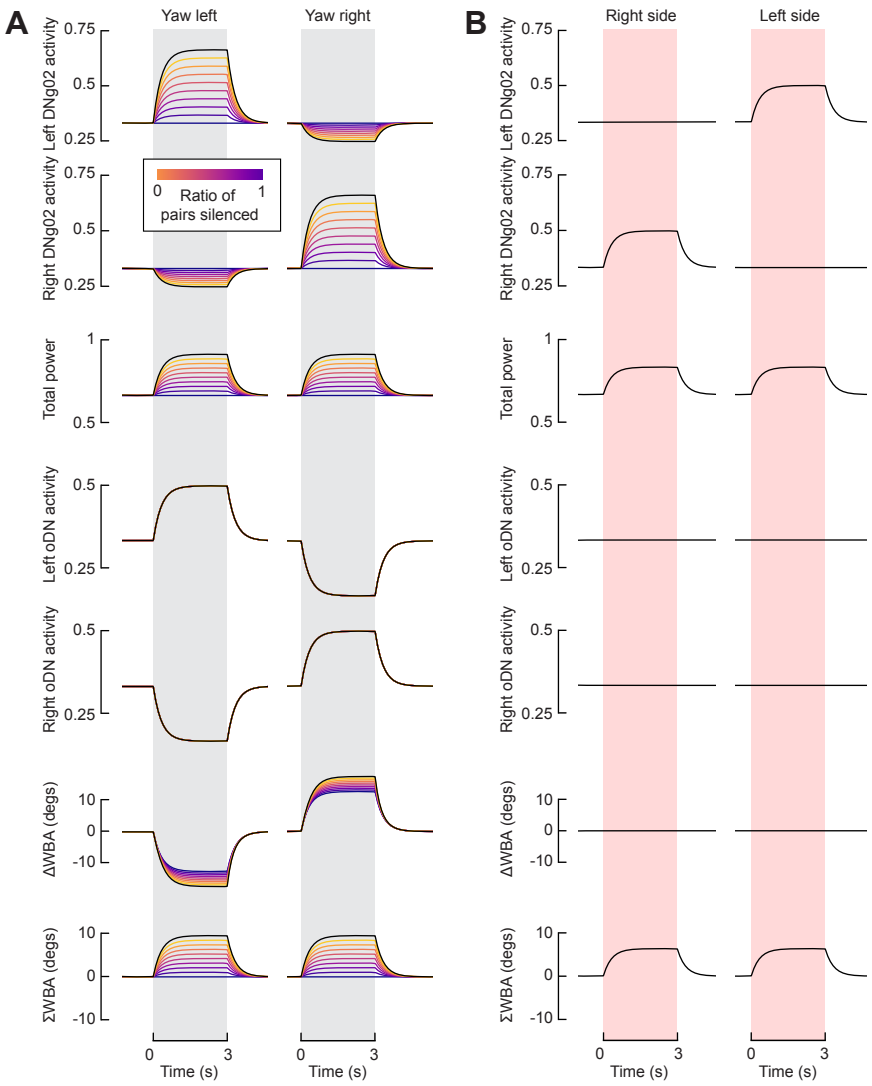

Figure 4.8: Symmetrical connectivity model recapitulates data.
(A) Model II recapitulates silencing data. Plotting conventions as in 4.6.
(B) Model II recapitulates unilateral activation data. Plotting conventions as in 4.7.

- In the symmetrical connectivity model (Model II), there is no imposed constraint to maintain bilateral symmetry in wing motion. In Model I, this imposed constraint simulated the biomechanical coupling of the scutellum and mechanosensory and visual feedback.

- In the asymmetrical connectivity model (Model I), there are no additional DN pathways required to recapitulate the dataset collected.

- In the symmetrical connectivity model (Model II), the magnitude of the changes in DNg02 activity on the left and right sides is asymmetric (e.g., in response to yaw left stimuli, the left DNg02s increase in activity more than

the right DNg02s decrease). This asymmetry is required to recapitulate the silencing results.

- In the symmetrical connectivity model (Model II), there is no reciprocal connectivity across the midline. Because of the asymmetry in DNg02 responses to yaw motion in this model, reciprocal connectivity distorts the shape of the responses such that the modeled responses are inconsistent with the functional imaging results.

4.5 Discussion

In this chapter, we continued our investigation of the role of the DNg02 neurons in the optomotor response. Namiki and colleagues [21] showed that DNg02 activation results in increases in total mechanical power production during flight; we investigated the involvement of the DNg02s in modulating power production during the optomotor response by estimating the power produced by each wing when DNg02 neurons are silenced. Much like the magnitude of the wing optomotor response was reduced by silencing DNg02 neurons (Figure 3.8), so too are the differential in power production (the magnitude of the asymmetry in power) and the bilateral sum of power production (the total power produced) reduced. This result supports the hypothesis that the DNg02s provide input to the power muscle MNs.

Whereas the silencing experiments presented in Chapter 3 indicated that the DNg02s are required for the optomotor response, unilaterally activating across the DNg02 population suggested that the DNg02 neurons are not sufficient to induce a steering behavioral response. The mechanical power required to flap a wing back and forth scales roughly with (stroke amplitude)^3 [7]. Thus, an increase in wing stroke amplitude would require an increase in mechanical power, whereas a decrease in stroke amplitude could still be sustained with decrease in mechanical power, assuming that wingbeat frequency remains constant. The steering muscles are not thought to contribute to the positive power required to flap the wings; rather they perform negative work, but function as controllable dynamic springs to regulate the mechanics of the wing hinge [29]. Given the strong evidence that the DNg02s provide input to the power muscles, it is notable that silencing the DNg02s reduced the motion of both the wing that increases in amplitude and the wing that decreases during the optomotor response (Figure 3.10). This result would support the result in [14] that measured bilateral differences in the Ca^{2+} signals within both the DLMs and DVMs during presentation of optomotor stimuli, strongly suggesting that the left and right sets of muscles can be activated asymmetrically.

We therefore thought it worth considering the possibility that the fly is indeed capable of delivering different amounts of mechanical power to the two wings, despite the fact that the architecture of the thorax, particularly the structure of the scutellum and sculler lever arms, would seem to preclude this. Could the patterns of asymmetrical power muscle activity observed by Lehmann and colleagues (2013) translate into a differential mechanical drive of the left and right wings? While it is true that the scutellar lever arms appear to be rigidly linked across the two side of the thorax [3], this does not entirely exclude the possibility that this mechanical system could exhibit a bilateral 'wobble,' such that the oscillatory trajectory of the posterior notal wing process (the tip of the scutellar lever arm that contacts the second axillary sclerite) might be larger on one side of the fly than the other, thus allowing differential drive to the two wings. According to this hypothesis, this bilateral asymmetry might be regulated via careful coordination of steering and power muscle activity, the latter of which involves the action of the DNg02 cells. Furthermore, whereas the mechanical role of the scutellar lever arms in coordinating the motion of the two wings has been well studied [1, 3], little is known about the anterior notal wing process, which is thought to serve as the other primary means of transmitting the strains of the power muscles to the wing. Due to its more flexible attachment to the notum [1, 19, 23] and the more lateral position of the DVMs, it is possible that this structure more easily permits differential actuation of the two wing hinges than the scutellar lever arms, which are actuated by the more medially positioned DLMs.

To formally consider this hypothesis, we constructed two models of the neural circuits underlying the optomotor response. The first model, Model I, assumes that the asymmetrical power activity in the power muscles does indeed translate to differential mechanical drive in the thorax , and that the asymmetrical power activity arises as a result of asymmetrical connectivity from the DNg02s to the MNs driving the power muscles (Figure 4.4B). In this model, external sensory stimuli are required to induces asymmetrical motor output; the unilateral activation results (Figures 4.2 and 4.3) are explained by the fact that during those experiments, no external stimuli indicated that the fly was turning. Other DNs, then, as well as mechanosensory feedback from the wings and halteres, are required to provide input to the steering muscles and to enable asymmetrical motor outputs.

Alternatively, we constructed a secondary model, Model II, which assumed that the DNg02s provide bilaterally symmetric input to the power muscle MNs (e.g., the left DNg02s provide equal input to both the left and right power muscle MNs; Figure 4.4C). The total power available to each wing was then simulated as the sum of the

activities of the left and right DNg02s; the amount of power drawn by each wing was calculated as the product of the total available power and the activity of other DNs (oDNs) which provided input to either the steering muscle MNs or power muscle MNs.

Both models fully recapitulated the observed data (Figures 4.5-4.8). In both models, the DNg02 neurons are necessary but insufficient to induce turning behaviors, supporting the conclusion that other, as yet unknown, neuronal pathways are also required for these behaviors. Distinguishing between the two models is currently not possible through experimentation. Complete abolishment of the DNg02s in the optomotor response could result in distinguishing between the models; whereas complete abolishment of the DNg02s results in a complete abolishment of the optomotor response in Model I (Figure 4.6), in Model II, the optomotor response is still present, albeit at a lower magnitude, when all the cells are abolished (Figure 4.8A). Experimentally, complete abolishment is challenging; we silenced using the inward-rectifying potassium channel Kir2.1, which reduces but does not completely abolish the ability of cells to fire action potentials and release neurotransmitter, and the driver line labeling the largest number of cells tested (SS01562, 19 cells) does not target the entire population. Other effectors may result in a more complete abolishment (e.g., genes promoting cell death like reaper (rpr), head involution defective (hid), or grim). A driver line labeling more DNg02 pairs is available (R42B02), however, we found that flies from this driver line were prohibitively unhealthy and a cross of this line to Kir2.1 did not result in viable progeny. Alternatively, a full connectome of the VNC, indicating all pathways from the DNg02 neurons to all the MNs, could be an invaluable tool, although the strengths of synaptic connections in a connectome are difficult to deduce without experimental evidence.

In summary, we propose that flies might be able to differentially regulate the mechanical power delivered to the two wings by the DLMs and DVMs. This active process might be mediated by a combination of asymmetrical activation of the power muscles themselves (as observed by Lehmman et al., 2013) and asymmetrical regulation of the left and right hinge mechanics by the steering muscle system, generating a bilateral wobble in the motion of scutellar lever arm system. Silencing the DNg02 cells would then reduce the magnitude of the optomotor response, either because they are directly involved in regulating the bilateral asymmetry in power production (Model I), or because they regulate the total production of power (Model II). Both mechanisms can explain why silencing the DNg02 cells would reduce the magnitude of the optomotor response, and the observation that unilateral activation

of DNg02 neurons is alone insufficient to recapitulate the large bilateral changes in wing motion characteristic of the optomotor response (because regulation of hinge mechanics requires the action of the steering muscles). Under this hypothesis, alternative descending pathways would be responsible for transmitting commands to the steering motor neurons, which are bilaterally uncoupled and can act independently. Hopefully, this somewhat complex hypothesis will eventually be testable, once data from a complete Drosophila nervous system connectome (i.e., brain and VNC) are available. Regardless, identification of the DNg02 neurons as an important component in the optomotor response provides a convenient entry point into a wide array of inquiries regarding the descending control of flight behavior in insects.

4.6 Methods and materials for Chapters III and IV

Experimental model and subject details

All experiments were conducted on 2-to-5 day old female Drosophila melanogaster reared at 25°C on a 12:12 hr light-dark cycle unless otherwise specified. For the optogenetic activation experiments, we reared the flies on standard cornmeal fly food containing 0.2 mM trans-Retinal (ATR) (Sigma-Aldrich) and transferred flies 0-2 days after eclosion onto standard cornmeal fly food with 0.4 mM ATR in dark conditions. For all other experiments, flies were reared on standard cornmeal fly food. All standard cornmeal food was supplemented with additional yeast. For the silencing experiments, we used flies resulting from a cross of each split-GAL4 line with 10XUAS-Kir2.1-EGFP. For functional imaging experiments, we used flies resulting from a cross of the split-GAL4 lines with 20XUAS-jGCaMP8m; 10XUAS-myr::tdtomato. Similarly for expression analysis, we crossed split-Gal4 lines to UAS-mCD8-GFP; UAS-RedStinger. To trace post synaptic partners of DNg02 neurons, specified split-Gal4 lines were cross to trans-Tango; F1 progeny were stored in 18°C for ~3 weeks before dissection and processing.

For unilateral activation experiments, we used a "Flp-out" construct with UAS sequences upstream and Chrimson-Venus as the downstream effector. Flp recombinase expression under heat shock control during development can stochastically elicit temporal excision of transcriptional stop sequences in the parent neuroblast of DNg02 neurons, resulting in the heritable, permissive conformation of Chrimson-Venus under DNg02 split-Gal4 control. For these experiments, we used flies resulting from a cross of pJFRC300-20XUAS-FRT>-dSTOP-FRT>-CsChrimson-mVenus in attP18 on (X) combined with specified split-Gal4 hemidrivers on (II) and (III) chromosomes with hs-FLPG5.PEST in attP3 (X). Temperature-shift de-

REAGENT or RESOURCE	SOURCE	IDENTIFIER
Chemicals, peptides, and recombinant proteins		
EM-Grade Paraformaldehyde 32%	Electron Microscopy Sciences	15714-S
Normal Goat Serum	Sigma-Aldrich	G9023-5ML
Vectashield Plus	Vector Laboratories	H-1900-10
Phosphate Buffered Saline (10x)	Sigma-Aldrich	P5493-1L
Triton-X	Sigma-Aldrich	T8787-100ML
All-trans-retinal	Sigma-Aldrich	CAS: 116-31-4
Antibodies		
Mouse mAb anti-Bruchpilot supernatant	Developmental Studies Hybridoma Bank	nc82; RRID: AB_2314866
Chicken anti-GFP polyclonal	Thermo Fisher Scientific	Cat# A10262,_RRID:AB_2534023
Rabbit mAb anti-HA-Tag	Cell Signaling Technology	Cat# 3724, RRID:AB_1549585
Rat anti-FLAG (DYKDDDDK Epitope Tag Antibody)	Novus Biologicals	Cat# NBP1-06712SS, RRID:AB_1625982
Goat anti-Mouse Cy5	Jackson ImmunoResearch	Cat# 115-175-166, RRID:AB_2338714
Goat anti-Chicken Alexa Fluor Plus 488	Thermo Fisher Scientific	Cat# A32931,_RRID:AB_2762843
Goat anti-Rabbit Alexa Fluor 546	Thermo Fisher Scientific	
Goat anti-Rat Cy3	Jackson ImmunoResearch	Cat# 112-165-003, RRID:AB_2338240
Goat anti-Rabbit Alexa Fluor 488	Thermo Fisher Scientific	Cat# A-11034, RRID:AB_2576217
Software and algorithms		
Realtime machine tracking software	[28]	http://florisvb.github.io/multi_tracker
Python	https://www.python.org	RRID:SCR_008394
Matplotlib	https://matplotliborg	RRID:SCR_008624
Seaborn	https://seaborn.pydata.org	RRID:SCR_018132
Fiji	https://fiji.sc/	RRID:SCR_002285

Table 4.2: Key Resources Table for Chapter III: Chemicals, peptides, & recombinant proteins, antibodies, and software & algorithms.

REAGENT or RESOURCE	SOURCE	IDENTIFIER
Experimental models: Organisms/strains		
D. melanogaster: P{20XUAS- IVS-CsChrimson.mVenus}attP2	Bloomington Drosophila Stock Center	RRID:BDSC 55136
D. melanogaster: 10XUAS- Kir2.1-EGFP	Gift from D. Anderson	N/A
D. melanogaster: 20XUAS- IVS-jGCaMP8m}attP5	Bloomington Drosophila Stock Center	RRID:BDSC 92591
D. melanogaster: 10XUAS- IVS-myr::tdtomato}attP2	Bloomington Drosophila Stock Center	RRID:BDSC 32221
D. melanogaster: 20XUAS- jGCaMP8m; 10XUAS- myr::tdtomato	Constructed from above two lines	N/A
D. melanogaster: pJFRC300-20XUAS-mVenus FRT>-dSTOP-FRT>-CsChrimson- in *attP18* unilaterals	Gift from G. Rubin	N/A
D. melanogaster: 20XUAS-FRT>-dSTOP-FRT>-CsChrimson-mVenus; SS02535	Constructed from above line and indicated split-Gal4 line	N/A
D. melanogaster: 20XUAS-FRT> -dSTOP-FRT>-CsChrimson-mVenus; SS01578	Constructed from above line and indicated split-Gal4 line	N/A
D. melanogaster: 20XUAS-FRT> -dSTOP-FRT>-CsChrimson-mVenus; SS02625	Constructed from above line and indicated split-Gal4 line	N/A
D. melanogaster: hs-FLPG5.PEST in attP3	Bloomington Drosophila Stock Center	RRID:BDSC 62118

Table 4.3: Key Resources Table for Chapter III: Experimental models.

REAGENT or RESOURCE	SOURCE	IDENTIFIER
Experimental models: Organisms/strains (continued)		
D. melanogaster: trans-Tango	Bloomington Drosophila Stock Center	RRID:BDSC 77124
D. melanogaster: MCFO-4 and MCFO-5	Bloomington Drosophila Stock Center	RRID:BDSC 64088 and RRID:BDSC 64089
D. melanogaster: UAS-mCD8-GFP (X); UAS-RedStinger (II) (nuclear DsRED)	N/A	N/A
Heisenberg Lab Canton S	N/A	N/A
D. melanogaster: empty-split vector control	Bloomington Drosophila Stock Center	RRID:BDSC_79603
D. melanogaster: SS02634	Bloomington Drosophila Stock Center	RRID:BDSC_75970
D. melanogaster: SS02627	Namiki et al.	N/A
D. melanogaster: SS01577	Namiki et al.	N/A
D. melanogaster: SS02535	Namiki et al.	N/A
D. melanogaster: SS01073	Bloomington Drosophila Stock Center	RRID:BDSC_75839
D. melanogaster: SS01578	Namiki et al.	N/A
D. melanogaster: SS02550	Namiki et al.	N/A
D. melanogaster: SS01563	Namiki et al.	N/A
D. melanogaster: SS02625	Bloomington Drosophila Stock Center	RRID:BDSC_75974
D. melanogaster: SS02624	Bloomington Drosophila Stock Center	RRID:BDSC_75972
D. melanogaster: SS02544	Namiki et al.	N/A
D. melanogaster: SS02630	Namiki et al.	N/A
D. melanogaster: SS01562	Namiki et al.	N/A

Table 4.4: Key Resources Table for Chapter III: Experimental models (continued).

pendent CsChrimson-Venus-labeled DNg02 clones were induced by heat shocking 0-12 hour old embryos in a bottle for 60-90 min in a 37°C water bath. F1 progeny were returned to standard rearing conditions 617 (25°C) until eclosion; adults were transferred to 0.4mM ATR food for ~3 days in dark conditions until experimentation. For single cell analysis using the multicolor flip out method [22], we used flies resulting from the cross of a specified Gal4 driver to MCFO-4 or MCFO-5 depending on the cell density of the driver (MCFO-4 and MCFO-5 for < 10 and > 10 pairs of neurons, respectively). For bilateral activation experiments, we used flies reared in optogenetic conditions resulting from a cross of male flies from the split-GAL4 line SS02625 with UAS-CsChrimson female virgin flies.

Quantification and statistical analysis

All experiments were analyzed with custom scripts written in Python. Variance across individuals is quantified as the bootstrapped 95% confidence interval using Seaborn statistical functions, with 1,000 bootstrap iterations. We performed a bootstrapping analysis to assess whether the results in Figures 3.8, 3.11, 3.12, 3.13, 3.9, 3.10, and 3.14 were significant. In each iteration, we randomly sampled with replacement from both the behavioral metric dataset (e.g., ΔWBA) and the number of pairs silenced, such that responses were randomly paired to numbers of pairs. Then, we fit a line of best fit to the bootstrapped dataset. The p-value was then calculated as:

$$p = \frac{\#_{i=1}^{r}(|m_i| \geq |m_{\text{observed}}|}{r} \tag{4.7}$$

where $r = 100,000$ is the number of iterations, m_i is the slope of the i^{th} iteration, and m_{observed} is the observed slope. The p-value is therefore the fraction of iterations yielding a more extreme slope than observed [16]. At each iteration, $N = 144$ subsamples were taken, the same number of samples as in the original dataset.

To determine the relative timing of the movement of different body appendages, we fit Gaussian functions to the time derivative of the traces (Figure 3.2I-L, 3.3I-K). Derivatives were calculated using a Savitzky-Golay filter, with a window length of 0.16 s and a polynomial of order 1 (i.e., a straight line fit to the data in a sliding window of length 0.16 s). Gaussians were fit to data placed on the parameters such that $\omega_p \in [0, 100]$, $d \in [0, 1]$, and $t_p \in [0, 1]$.

Methods details

Fly tethering

For optomotor response (Figures 3.1-3.2), silencing (Figure 3.8-3.13), and unilateral activation experiments (Figure 5), female flies were anesthetized on a cold plate at 4°C and tethered to a tungsten wire (0.13 mm diameter) with UV-activated glue (Henkel; Bondic Inc.) at the anterior dorsal portion of the scutum. Flies were allowed to recover for at least 15 minutes prior to testing.

For functional imaging experiments (Figure 4), we tethered each fly to a specially designed physiology stage that permitted access to the posterior side of the fly's head [17]. We filled the holder with saline and removed a section of cuticle dorsal to the esophageal foramen, by first laser-cutting a window in the cuticle dorsal to the esophageal foramen using a custom built laser based on the design of [8, 11], then removing the window and dissected any remaining tissue obscuring the brain's surface manually to improve imaging quality, including adipose bodies and trachea. This dissection protocol allowed us to simultaneously image neurons on the left and right side of the brain with limited damage to the animal.

Flight arenas and visual stimuli

For optomotor response (Figure 3.1-3.2, 3.8-3.13) and unilateral activation experiments (Figure 5), a tethered fly was positioned such that its stroke plane was horizontal and perpendicular to the vertical optical axis of a digital camera (Point Grey USB 3.0 camera equipped with a MLM3X-MP Computar 666 macro lens and Hoya B-46RM72-GB IR-pass filter). An IR light source (driver: LEDD1B, and LED: M850L3; Thorlabs) illuminated the stroke planes of the left and right wing, and we used Kinefly [28] software to track the anterior-most angular excursion of the fly's left and right wingbeats. To track the head, abdomen, and leg angles, we used DeepLabCut [18]. Training was based on the manual annotation of the joints of interest on two frames from each trial; the output of the trained network gave the x and y positions of each joint in pixels as a function of time. Flies were surrounded by a 11 x 3 panel (88 x 24 pixel) LED arena (470 nm) that covered 330° of azimuth with resolution of 3.75° in front of the fly [25]. Digital values for the wingbeat amplitudes were converted into voltages using a PhidgetAnalog 1002 and 1019 (Phidgets) and sent to a LED panel controller (IOrodeo) which was programmed so that flies could regulate the angular velocity of the visual display via the difference in wingbeat amplitude of the two wings for presentations of closed-loop stimuli, with

a gain of 6° s^{-1} for each °ΔWBA. For presentations of closed-loop stripe fixation stimuli, a dark stripe subtending 15° was used. To induce the optomotor response, we rotated a striped drum (spatial frequency = 15°) in yaw at a velocity of 180° s^{-1}. Three second presentations of yaw rotation were preceded and followed by 1 s of static striped drum to mitigate the effects of light artefacts and interspersed with 3 s of closed-loop stripe fixation. The direction of yaw rotation was shuffled pseudo-randomly. Each fly was subjected to up to 20 presentations of rotation in each direction.

Kinefly software was also used to track the wingbeat amplitude of the flies used for functional imaging experiments (Figure 4). We illuminated the wings using four horizontal fiber-optic IR light sources (M850F2, Thorlabs) distributed in a ~ 90° arc behind the fly. In these 687 experiments, visual stimuli were presented using a 12 x 4 panel (96 x 32 pixel) arena that covered 21° of azimuth with a resolution of 2.25°, with a spectral peak of 450 nm to reduce light pollution 689 from to LEDs into the photomultiplier tubes of the 2-photon microscope. We presented an array of visual starfield patterns, each for 3 s, alternated with 2 s static starfield patterns. Visual patterns were presented in pseudo-random order, including pitch, roll, and yaw in both directions and progressive and regressive motion.

Anatomy

All anatomy panels were generated from 2-7 day old female Drosophila melanogaster unless otherwise specified. Full adult central nervous systems were dissected in 1xPBS, pH 7.4. All room temperature (RT) incubations are conducted with gentle agitation. Nervous systems were (1) fixed in 4% RT EM-grade paraformaldehyde for 25 minutes; (2) washed in RT 1XPBS 3X for 15 minutes and stored overnight in 4oC; (3) washed in RT 0.3% PBS-T (PBS containing 0.3% Triton-X) 5X for 15 minutes; (4) incubated in blocking buffer (7.5% normal goat serum in 0.3% PBS-T) for 1 hour at RT and transferred to 4°C overnight; (5) incubated in primary antibody, diluted in blocking buffer, at RT for 4 hours and transferred to 4°C for three nights; (6) washed 5X 15 min at RT in 0.3% PBS-T; (7) incubated with secondary antibody diluted in blocking buffer at RT for 4 hours and transferred to 4°C for an additional three nights; (8) washed 5X 15 min in RT 0.3% PBS-T; (9) mounted on a slide posterior side up with spacers using Vectashield Plus. For nervous systems with neuropil marker along with GFP and DsRED genetic reporters, we used for 1:30 nc82, 1:2000 chicken anti-GFP, and 1:2000 rabbit anti-DsRED primary antibodies. Secondary antibodies were then used at the following concentrations: anti-Mouse Cy5 (1:300), anti-Chicken

Alexa 488 (1:1000), anti-Rabbit Alexa 546 (1:1000). Experiments with neuropil marker and Chrimson-Venus used the same antibody protocol without anti-DsRED primary and anti-Rabbit Alexa 546 secondary. Multicolor flip out experiments were conducted on 2 day old female flies; we used 1:30 nc82, 1:200 Rat anti-FLAG, and 1:300 Rabbit anti-HA primary antibodies, and 1:300 anti-Mouse Cy5, 1:500 anti-Rat Cy3, 1:500 anti-Rabbit Alexa 488 secondary antibodies.

Whole mount nervous systems were imaged using confocal microscopy [Zeiss LSM 880 using Zen Black (Carl Zeiss, Inc.)] Optical sections were imaged using a 40X water lens with 1-μM intervals, and 1024 × 1024 pixel resolution with tile scan. Post processing alignment of tiles was conducted using Zen Blue; anatomy panels were constructed in FIJI [26]. In some panels, signal from off target single cells was digitally removed in FIJI to improve visualization of the neuron in question. Cell body quantification was conducted manually in FIJI. Cells were counted on each side of the brain and then averaged across 3 flies. If more than twice as many cells were counted on one side than the other, the brain was excluded from the count; this occurred twice, once each in the counts for SS02627 and SS01562.

Functional imaging

We imaged at an excitation wavelength of 930 nm using a gavanometric scan mirror-based two-photon microscope (Thorlabs) equipped with a Nikon CFI apochromatic, near-infrared objective water-immersion lens (40x mag., 0.8 N.A., 3.5 mm W.D.). We recorded tdTomato and GCaMP8m fluorescence in the posterior slope arbors of DNg02 neurons bilaterally for data in Figure 4C-E; GcAMP7f was recorded unilaterally for data in Figure 4F-I. For bilateral imaging experiments, we acquired 72 x 29 μm images with 160 x 64 pixel resolution at 11.2 Hz, whereas we acquired 14.5 x 29 μm images with 64 x 128 pixel resolution at 13.1 Hz for unilateral imaging. To correct for motion in the x-y plane, we registered both channels for each frame by finding the peak of the cross correlation between each tdTomato image and the trial-averaged image. A region of interest (ROI) was defined by the 10% most variable GCaMP8m pixels. A centerline was defined manually and used to divide the ROI into left and right halves. Because the esophagus auto-fluoresces and appears in the GCaMP8m channel, we manually defined a mask to exclude it from the analysis. To correct for motion in z, we normalized the GCaMP8m fluorescence to the tdTomato fluorescence for a given frame by multiplying each pixel by the mean GCaMP fluorescence in the defined ROI for that frame and dividing by the mean tdTomato fluorescence in the ROI. For each side of the brain in each frame, we

computed the fluorescence (F_t) of the GCaMP8m signal by subtracting the average of the background from the average of the ROI. The background was defined as the mean fluorescence of the 5% dimmest pixels across the entire image. To standardize the measured neuronal activity across individual preparations, we normalized the baseline-subtracted fluorescence to the maximum observed for each individual fly on each side of the brain as $\Delta F/F = (F_t - F_0)/F_{95}$, where F_0 is the mean of the 5% lowest F_t and F_{95} is the mean of the 95% highest F_t. For experiments in which we varied the rotational velocity of the visual display, we parsed the fluorescence data into bins of WBA, regardless of visual stimulus, by taking the mean WBA across 5 frames (Figure 4I). Data from a given fly was only included in the bin if there were at least 10 data points from that fly (i.e., if there were 10, 5 frame examples for the given fly at the WBA for a given bin). To be included in the dataset upon transition between quiescence and flight, both the quiescent period and the flight period were required to be longer than 1 s in duration, and the fly was required to have executed the transition at least 10 times.

Unilateral activation experiments

We positioned a fiber optic light guide (FT1500EMT; Thorlabs) behind the fly, aimed at the thorax, which conducted the output of a 617 nm LED (M617F1, Thorlabs) at 3.4 mW/mm^2. In each experiment, we elicited 10 responses to each stimulus duration with an interpulse interval of 10 s. For the data in Figure 5, stimulus durations of 0.05, 0.1, 0.3, 0.5, 1, 3, and 5 s were used. For the data in Figure 6, we used stimulus durations of 0.01, 0.025, 0.05, 0.1, 0.25, and 0.5 s. Durations were presented in pseudo-random order. The response to activation (Figure 5G-H) was determined as the average of the relevant quantity for the first 2 s following the onset of the stimulus minus the average for the second preceding the onset of the stimulus.

Model I: Asymmetric connectivity

The simulated fly is initialized with symmetrical wing kinematics. At each time step, the model queries whether the sensory input is symmetric or asymmetric. If the sensory input is symmetric, the symmetric wing kinematics are enforced; if the sensory input is asymmetric, the wings are free to move asymmetrically:

$$\mathrm{WBA_L} = \begin{cases} w_c \lambda_{\mathrm{DNg02,R}} + w_i \lambda_{\mathrm{DNg02,L}} & \text{if sensory input asymmetric} \\ 0.5(w_c + w_i)(\lambda_{\mathrm{DNg02,L}} + \lambda_{\mathrm{DNg02,R}}) & \text{if sensory input symmetric} \end{cases} \tag{4.8}$$

$$\mathrm{WBA_R} = \begin{cases} w_c \lambda_{\mathrm{DNg02,L}} + w_i \lambda_{\mathrm{DNg02,R}} & \text{if sensory input asymmetric} \\ 0.5(w_c + w_i)(\lambda_{\mathrm{DNg02,L}} + \lambda_{\mathrm{DNg02,R}}) & \text{if sensory input symmetric} \end{cases} \tag{4.9}$$

where w_c and w_i are the weights of the connections from the DNg02s to the contralateral and ipsilateral power muscle MNs, respectively ($w_c = 1.1$ and $w_i = 0.9$), and λ is the activity of the DNg02 neuron being modeled. The DNg02 activity calculation is given in Algorithm 1. The activity of the simulated neurons varies depending on the stimulus input to the model, and is defined for no stimulus conditions, yaw visual stimuli, and unilateral DNg02 activation. The DNg02 activity is then calculated using a leaky integrator, with $A = 3$ and $B = 1$ such that feedback from reciprocal connectivity is weaker than self-excitation from timestep $t - 1$ to timestep t. The variable $\eta \in [0, 1]$ represent the ratio of DNg02 neurons that can respond and enables simulations of experiments with silenced neurons; when $\eta = 0$, all of the neurons are fully silenced.

Model II: Symmetric connectivity

We modeled the total power available as

$$P_{\mathrm{total}} = \lambda_{\mathrm{DNg02,L}} + \lambda_{\mathrm{DNg02,R}} \tag{4.10}$$

and the WBA amplitude of each wing as the product of the total power available and the activity of the oDN on the contralateral side:

$$\mathrm{WBA_L} = \lambda_{\mathrm{oDN,R}} P_{\mathrm{total}} \tag{4.11}$$

$$\mathrm{WBA_R} = \lambda_{\mathrm{oDN,L}} P_{\mathrm{total}} \tag{4.12}$$

where the algorithms used to calculate $\lambda_{\mathrm{DNg02,L}}$, $\lambda_{\mathrm{DNg02,R}}$, $\lambda_{\mathrm{oDN,L}}$, and $\lambda_{\mathrm{oDN,R}}$ are shown in Algorithm 2. Testing this model as we tested Model I demonstrates that it, like model I, can fully recapitulate the silencing, functional imaging, and unilateral activation experiments (Figure 4.8).

Algorithm 1 Model I: DNg02 activity

$\text{input}_{\text{DNg02,L}} \leftarrow 1/(A+B)$
$\text{input}_{\text{DNg02,R}} \leftarrow 1/(A+B)$
if stimulus is yaw right motion **then**
  $\text{input}_{\text{DNg02,L}} \leftarrow 1-0.5\eta$
  $\text{input}_{\text{DNg02,R}} \leftarrow 1+0.5\eta$
else if stimulus is yaw left motion **then**
  $\text{input}_{\text{DNg02,L}} \leftarrow 1+0.5\eta$
  $\text{input}_{\text{DNg02,R}} \leftarrow 1-0.5\eta$
else if stimulus is left activation **then**
  $\text{input}_{\text{DNg02,L}} \leftarrow 1.5$
else if stimulus is right activation **then**
  $\text{input}_{\text{DNg02,R}} \leftarrow 1.5$
end if
$\lambda_{\text{DNg02,L}}[t] \leftarrow \lambda_{\text{DNg02,L}}[t-1]$
  $+(-A\lambda_{\text{DNg02,L}}[t-1] + \text{input}_{\text{DNg02,L}} + B\lambda_{\text{DNg02,R}}[t-1])\Delta t$
$\lambda_{\text{DNg02,R}}[t] \leftarrow \lambda_{\text{DNg02,R}}[t-1]$
  $+(-A\lambda_{\text{DNg02,R}}[t-1] + \text{input}_{\text{DNg02,R}} + B\lambda_{\text{DNg02,L}}[t-1])\Delta t$

Algorithm 2 Model II: DNg02 and oDN activity

$\text{input}_{\text{DNg02,L}} \leftarrow 1/A$
$\text{input}_{\text{DNg02,R}} \leftarrow 1/A$
$\text{input}_{\text{oDN,L}} \leftarrow 1/A$
$\text{input}_{\text{oDN,R}} \leftarrow 1/A$
if stimulus is yaw right motion **then**
  $\text{input}_{\text{DNg02,L}} \leftarrow 1-0.25\eta$
  $\text{input}_{\text{DNg02,R}} \leftarrow 1+\eta$
  $\text{input}_{\text{oDN,L}} \leftarrow 0.5$
  $\text{input}_{\text{oDN,R}} \leftarrow 1.5$
else if stimulus is yaw left motion **then**
  $\text{input}_{\text{DNg02,L}} \leftarrow 1+\eta$
  $\text{input}_{\text{DNg02,R}} \leftarrow 1-0.25\eta$
  $\text{input}_{\text{oDN,L}} \leftarrow 1.5$
  $\text{input}_{\text{oDN,R}} \leftarrow 0.5$
else if stimulus is left DNg02 activation **then**
  $\text{input}_{\text{DNg02,L}} \leftarrow 1.5$
else if stimulus is right DNg02 activation **then**
  $\text{input}_{\text{DNg02,R}} \leftarrow 1.5$
end if
$\lambda_{\text{DNg02,L}}[t] \leftarrow \lambda_{\text{DNg02,L}}[t-1] + (-A\lambda_{\text{DNg02,L}}[t-1] + \text{input}_{\text{DNg02,L}})\Delta t$
$\lambda_{\text{DNg02,R}}[t] \leftarrow \lambda_{\text{DNg02,R}}[t-1] + (-A\lambda_{\text{DNg02,R}}[t-1] + \text{input}_{\text{DNg02,R}})\Delta t$
$\lambda_{\text{oDN,L}}[t] \leftarrow \lambda_{\text{oDN,L}}[t-1] + (-A\lambda_{\text{oDN,L}}[t-1] + \text{input}_{\text{oDN,L}})\Delta t$
$\lambda_{\text{oDN,R}}[t] \leftarrow \lambda_{\text{oDN,R}}[t-1] + (-A\lambda_{\text{oDN,R}}[t-1] + \text{input}_{\text{oDN,R}})\Delta t$

Bibliography

[1] Edward G. Boettiger and Edwin Furshpan. The mechanics of flight movements in Diptera. *The Biological Bulletin*, 102(3):200–211, 1952.

[2] Federico Davoine and Kaitlyn Fouke. Unpublished electrophysiological muscle recordings. 2023.

[3] Tanvi Deora, Amit Kumar Singh, and Sanjay P. Sane. Biomechanical basis of wing and haltere coordination in flies. *Proceedings of the National Academy of Sciences*, 112(5):1481–1486, 2015.

[4] Michael Dickinson. Insect flight. *Current Biology*, 16(9):R309–R314, 2006.

[5] Michael H. Dickinson and John R.B. Lighton. Muscle efficiency and elastic storage in the flight motor of drosophila. *Science*, 268(5207):87–90, 1995.

[6] Michael H. Dickinson and Michael S. Tu. The function of dipteran flight muscle. *Comparative Biochemistry and Physiology Part A: Physiology*, 116 (3):223–238, 1997.

[7] Charles Porter Ellington. The aerodynamics of hovering insect flight. VI. Lift and power requirements. *Philosophical Transactions of the Royal Society of London. B, Biological Sciences*, 305(1122):145–181, 1984.

[8] Andres Flores-Valle, Rolf Honnef, and Johannes D. Seelig. Automated long-term two-photon imaging in head-fixed walking Drosophila. *Journal of Neuroscience Methods*, 368:109432, 2022.

[9] Gerhard Heide. Flugsteuerung durch nicht-fibrilläre flugmuskeln bei der schmeißfliege calliphora. *Journal of Comparative Physiology A: Neuroethology, Sensory, Neural, and Behavioral Physiology*, 59(4):456–460, 1968.

[10] Gerhard Heide and Karl G. Götz. Optomotor control of course and altitude in Drosophila melanogaster is correlated with distinct activities of at least three pairs of flight steering muscles. *The Journal of Experimental Biology*, 199(8): 1711–1726, 1996.

[11] Cheng Huang, Jessica R. Maxey, Supriyo Sinha, Joan Savall, Yiyang Gong, and Mark J. Schnitzer. Long-term optical brain imaging in live adult fruit flies. *Nature Communications*, 9(1):872, 2018.

[12] Robert K. Josephson, Jean G. Malamud, and Darrell R. Stokes. Asynchronous muscle: A primer. *Journal of Experimental Biology*, 203(18):2713–2722, 2000.

[13] Fritz-Olaf Lehmann and Michael H. Dickinson. The changes in power requirements and muscle efficiency during elevated force production in the fruit fly Drosophila melanogaster. *The Journal of Experimental Biology*, 200(7): 1133–1143, 1997.

[14] Fritz-Olaf Lehmann, Dimitri A. Skandalis, and Ruben Berthé. Calcium signalling indicates bilateral power balancing in the Drosophila flight muscle during manoeuvring flight. *Journal of The Royal Society Interface*, 10(82): 20121050, 2013.

[15] Theodore Lindsay, Anne Sustar, and Michael Dickinson. The function and organization of the motor system controlling flight maneuvers in flies. *Current Biology*, 27(3):345–358, 2017.

[16] David J.C. MacKay. *Information theory, inference and learning algorithms*. Cambridge University Press, 2003.

[17] Gaby Maimon, Andrew D. Straw, and Michael H. Dickinson. A simple vision-based algorithm for decision making in flying Drosophila. *Current Biology*, 18(6):464–470, 2008.

[18] Alexander Mathis, Pranav Mamidanna, Kevin M. Cury, Taiga Abe, Venkatesh N. Murthy, Mackenzie Weygandt Mathis, and Matthias Bethge. Deeplabcut: Markerless pose estimation of user-defined body parts with deep learning. *Nature Neuroscience*, 21(9):1281–1289, 2018.

[19] Jaleel A. Miyan and Arthur W. Ewing. A wing synchronous receptor for the dipteran flight motor. *Journal of Insect Physiology*, 30(7):567–574, 1984.

[20] Farhan Mohammad, James C. Stewart, Stanislav Ott, Katarina Chlebikova, Jia Yi Chua, Tong-Wey Koh, Joses Ho, and Adam Claridge-Chang. Optogenetic inhibition of behavior with anion channelrhodopsins. *Nature Methods*, 14(3):271–274, 2017.

[21] Shigehiro Namiki, Ivo G. Ros, Carmen Morrow, William J. Rowell, Gwyneth M. Card, Wyatt Korff, and Michael H. Dickinson. A population of descending neurons that regulates the flight motor of Drosophila. *Current Biology*, 32(5):1189–1196, 2022.

[22] Aljoscha Nern, Barret D. Pfeiffer, and Gerald M. Rubin. Optimized tools for multicolor stochastic labeling reveal diverse stereotyped cell arrangements in the fly visual system. *Proceedings of the National Academy of Sciences*, 112 (22):E2967–E2976, 2015.

[23] John William Sutton Pringle. *Insect flight*, volume 9. Cambridge University Press, 1957.

[24] J.W.S. Pringle. The excitation and contraction of the flight muscles of insects. *The Journal of physiology*, 108(2):226, 1949.

[25] Michael B. Reiser and Michael H. Dickinson. A modular display system for insect behavioral neuroscience. *Journal of Neuroscience Methods*, 167(2): 127–139, 2008.

[26] Johannes Schindelin, Ignacio Arganda-Carreras, Erwin Frise, Verena Kaynig, Mark Longair, Tobias Pietzsch, Stephan Preibisch, Curtis Rueden, Stephan Saalfeld, Benjamin Schmid, et al. Fiji: An open-source platform for biological-image analysis. *Nature Methods*, 9(7):676–682, 2012.

[27] Shana R. Spindler and Volker Hartenstein. The Drosophila neural lineages: A model system to study brain development and circuitry. *Development Genes and Evolution*, 220:1–10, 2010.

[28] Marie P. Suver, Ainul Huda, Nicole Iwasaki, Steve Safarik, and Michael H. Dickinson. An array of descending visual interneurons encoding self-motion in Drosophila. *Journal of Neuroscience*, 36(46):11768–11780, 2016.

[29] M. Tu and M. Dickinson. Modulation of negative work output from a steering muscle of the blowfly Calliphora vicina. *The Journal of Experimental Biology*, 192(1):207–224, 1994.

[30] Simon M. Walker, Daniel A. Schwyn, Rajmund Mokso, Martina Wicklein, Tonya Müller, Michael Doube, Marco Stampanoni, Holger G. Krapp, and Graham K. Taylor. In vivo time-resolved microtomography reveals the mechanics of the blowfly flight motor. *PLoS Biology*, 12(3):e1001823, 2014.

[31] Ming Wu, Aljoscha Nern, W. Ryan Williamson, Mai M. Morimoto, Michael B. Reiser, Gwyneth M. Card, and Gerald M. Rubin. Visual projection neurons in the Drosophila lobula link feature detection to distinct behavioral programs. *Elife*, 5:e21022, 2016.

Chapter 5

CONCLUSION

In this thesis, we have explored some of the algorithms and neuronal pathways underlying locomotory behaviors in *Drosophila melanogaster*. These studies are necessarily interdisciplinary; as we endeavor to understand biological flight, for example, we rely upon our knowledge of engineering concepts drawn from fluid dynamics, structural biomechanics, and control theory, as well as neurobiological principles like sensory physiology. For that reason, the research presented in this thesis employs techniques drawn from both engineering and neuroscience; in Chapter II, we combine behavioral experiments with computational modeling to study path integration in *Drosophila*, and in Chapters III and IV we again make use of behavioral experiments and computational modeling, as well as neuronal imaging and manipulation with modern genetic techniques and estimations of flight kinetics to study the neuronal pathways underlying stabilization in flight. In this chapter, we summarize the work presented in this dissertation and discuss future directions for this work.

5.1 Algorithmic basis of local search in *Drosophila melanogaster*

In Chapter II, we performed experiments to study path integration in *Drosophila*. By constraining the animals to an annular arena, we greatly simplified the challenge of studying the behavior quantitatively; whereas prior experiments were limited by the diversity of search geometries observed in unconstrained local searching behavior (e.g., [3, 10]), our experiments were easily quantifiable in one dimension, with a clearly observable reversal point [1]. Similarly, we limited the sensory environment in which the flies performed their searches by conducting the experiments in the dark and with optogenetic activation of sugar-receptors in lieu of real food stimuli. These experimental conditions ensured that flies were not navigating based on visual landmarks or following a trail of, for example, sugar-water that they had tracked around the arena, and therefore allowed us to assume that they were making use of self-motion cues to integrate their outbound trajectory and determine their distance from the fictive food location.

Simplifying the behavior in these way enabled us to probe more specifically the algorithms underlying path integration than was possible in past experiments. By

observing the behavior of the flies after the fictive food stimulus was disabled (i.e., regardless of a fly's location, no optogenetic activation was provided), we demonstrated that flies are able to integrate in two dimensions; after fully circling the annular arena, some flies resumed their search over the former food zone. We then constructed a set of quantitative models of path integration using state transition diagrams. The models were were endowed with the ability to generate hypotheses, which we then tested through our behavioral experiments; the simple food-to-reversal (FR) model, for example, recapitulated the ability of real flies to reinitiate search over the former food location once the food stimulus was disabled, but it failed to recapitulate their ability to expand their search when multiple food sites are present. Given the failure of the FR model, we generated two alternative models to probe the algorithms underlying search when multiple food sites are present, the food-to-reversal' (FR') model, which assumes flies center their search over the first food site encountered after a reversal, and the center-to-reversal (CR) model, which assumes flies search over the center of all known food sites. The models performed differently when three food sites are known depending on the last encountered food site before the food stimulus is disabled; performing the same test with real flies indicated that their behavior is consistent with the CR model. As such, we conclude that flies zero their integrator at the center of a cluster of multiple food sites.

Future directions

Whereas our study focused on the algorithmic basis of path integration in *Drosophila*, other researchers have continued to probe the neuronal mechanisms underlying the behavior. For example, my colleague and coauthor on the paper presented in Chapter II, Amir Behbahani, collaborated on a project looking at the neuronal implementation of one of the computations required for path integration, the transformation of sensory input from egocentric to allocentric reference frames [12]. The sensory signals animals receive are referenced to the body (e.g., translation forward or lateral relative to the orientation of the body), but path integration requires navigation relative to a location in the global reference frame (e.g., North or South relative to a food site). In their paper, Lu and colleagues demonstrated that two cells types (PFNd and PFNn) in the central complex, a highly-conserved brain region associated with navigation in arthropods [20], encode translational velocity and heading in the egocentric reference frame [12]. Furthermore their downstream connectivity to a third class of neurons supports the transformation to the world reference frame [12].

Experiments in the constrained arena introduced in our paper with PFNd neurons silenced with Kir2.1 demonstrated that flies with PFNd neurons inhibited lose the ability to integrate their trajectories in two dimensions; unlike wild-type or control flies, these flies are not able to reinitiate their search at a former fictive food zone after fully circling the annular arena [12]. Further studies may continue to probe the neuronal pathways involved in path integration.

5.2 Neuronal pathways for flight stabilization

In Chapters III and IV, we explored the role of a population of descending neurons, the DNg02s, in flight stabilization. The DNs represent a set of around 400 neurons conveying information from the brain to the VNC; as an intense informational bottleneck, they afforded us a promising opportunity to gain purchase on the neuronal mechanisms underlying biological flight control. Namiki and colleagues [13] identified the DNg02s as a population of homomorphic neurons involved in flight control, with robust increases in wingbeat amplitude upon optogenetic activation in proportion to the number of cells activated. This proportional relationship indicated that the cells may be employing population coding, wherein the motor output is encoded by the number of DNg02 cells active rather than the graded activity of any one cell. Furthermore, the DNg02s were implied as relevant to visually-mediated flight behaviors, as they receive input in regions associated with visual processing in the brain and functional imaging experiments indicated neuronal responses to visual stimuli.

The results from Namiki and colleagues [13] suggested that the cells may be relevant to the optomotor response, a well-characterized behavior in which animals will attempt to steer to compensate for patterns of wide-field optic flow. The large number of cells (around 20 of the total 400 DNs) was relevant to this hypothesis, as flies need to compensate for many different perturbations to stability. Through population coding, the DNg02s were hypothesized to be able to provide the fine resolution over a wide dynamic range of possible motor responses that would be necessary for flight stabilization. We demonstrated that the DNg02s are indeed a required neuronal pathway for the optomotor response; when the DNg02 neurons are silenced, the magnitude of the optomotor response is diminished in proportion to the number of cells perturbed. Again, the proportional relationship is relevant, as it supported the population coding hypothesis. We further note that both the activation and silencing results supported the hypothesis that the DNg02 neurons provide input to the power muscles.

A detailed morphological investigation implied potential morphological variants within the population, with two variants identified: the Type I cells, which exhibit a clear figure-of-eight shape in the wing tectulum and haltere neuropil, and the Type II cells, which do not exhibit the clear figure-of-eight patterns. However, these morphological variants did not correspond to functional variants with respect to the patterns of wide-field optic flow presented in functional imaging experiments. This does not preclude functional variation with respect to other sensory stimuli, visual or otherwise. We further noted reciprocal connectivity within the population, though it was not clear whether the reciprocal connectivity was limited by side (e.g., DNg02 cells on the left side of the body only provide input to DNg02 cells on the left) or whether DNg02 neurons make connections across the midline (e.g., DNg02 cells on the left provide input to DNg02 cells on the left and right sides of the body).

Our functional imaging experiments indicated close correlations between DNg02 activity and contralateral wingbeat amplitude and asymmetries in DNg02 activity across the midline during the yaw optomotor response. For example, in response to yaw right visual motion, the left wing increases its amplitude and the right decreases, while the left DNg02s decrease their activity and the right cells increase their activity.

The functional imaging results, in tandem with the silencing experiments, may have implied a simple connectivity scheme in which the DNg02 neurons provide input to motor neurons on the contralateral side of the body to encode, for example, contralateral wingbeat amplitude. However, unilateral activation experiments probing this hypothesis demonstrated that unilateral DNg02 activation results in bilaterally symmetric wingbeat responses. This result implies that the DNg02 neurons are necessary, but insufficient for the optomotor response—they are required for the behavior, but they cannot alone induce it. Their insufficiency implies that there are other, as yet unknown, neuronal pathways that are also involved in the optomotor response.

We concluded by developing a set of models with respect to the downstream connectivity from the DNg02 neurons to the flight muscles that could fully explain our dataset. The models were designed to recapitulate the dataset under two connectivity schemes. Model I posited that the DNg02s connect asymmetrically to the flight muscles and that unilateral activation resulted in bilaterally symmetric wing motions because alternative biomechanical, sensory pathways, and, potentially, reciprocal connectivity within the population enforce bilaterally symmetry when the sensory input is symmetric. That is to say, if the fly receives no rotational stimuli, the

most parsimonious explanation is that it is not rotating, and the motor system may in this case reject descending input to rotate. Alternatively, Model II posited that the DNg02s connect symmetrically to the motor system to control the total power produced by the power muscles, and that alternative descending pathways provide the commands to generate asymmetrical maneuvers.

Future directions

Given that both models fully recapitulate the dataset, future experimenters may seek to disentangle the connectivity underlying the input from the DNg02s to the flight muscles. This would be aided by a full CNS connectome, in which the connections from the DNg02s to the flight muscle motor neurons could be traced and quantitatively analyzed. Furthermore, in these studies we primarily considered the input from the DNg02 neurons to the power muscles, but they may also provide input to the steering muscles. Indeed, in her dissertation work, Alysha de Souza noted that DNg02 activation modulates the b1 motor neuron firing phase and recruits the b2 motor neuron, two of the twelve steering muscle motor neurons [4]. Further experiments could continue to probe the nature of the connectivity, either through a connectome or through experimental work. Similarly, while we did not observe functional variation between the morphological variants, future work could continue to probe these variants. It is possible that they respond differently to sensory stimuli we did not test in the present work, or that they functionally diverge in the VNC and have different effects on the motor system. The former theory could be tested through additional functional imaging experiments with a more diverse array of sensory stimuli; the latter could be tested through additional optogenetic activation experiments, with either bilateral or unilateral activation, and high-speed imaging to resolve fine-scale kinematic variation.

The experiments presented here provide opportunities for studies on topics that may interest the neuroscience community more generally. For example, the optomotor response has been shown to be roughly modelled using a PI controller in fruit flies [5], implying that neurons can perform both proportional and integral control. However, the neuronal implementation of integration in particular remains elusive (although past work on the lobula plate tangential cells (LPTCs), which are generally though to encode patterns of wide-field optic flow, has suggested cellular mechanisms for integral feedback [14]). Our functional imaging results, which imply a close correlation between DNg02 activity and motor output, suggest that the integration likely occurs in the brain, upstream of the DNg02s; researchers interested in the

neuronal mechanisms for the sort of computation may be interested in considering the neuronal circuitry in the brain from the LPTCs to the DNg02s.

Similarly, the effects of multimodal sensory integration on motor responses during flight have been studied in many species, including bees [17], moths [9], and mosquitoes [18]. The DNg02 neurons provide good experimental access to the mechanisms of sensory integration. We interpret the optomotor response as the behavioral mechanism through which flies minimize rotations which cause optic flow on the retina, but these rotations would typically also involve sensory feedback from the antennae and halteres, as well as the eyes. The information from these different sensory structures is integrated to regulate motor output [7]. In all our experiments, however, flies are tethered and therefore irrotational, and they do not experience incident airflow. Studies have suggested that wind-sensing may mediate translational flight which would otherwise be inhibited by visual responses [1, 8]; further experiments could investigate whether this inhibition is upstream of the DNg02 neurons such that their response to progressive motion is diminished when wind stimuli are presented. Similarly, the interactions between olfactory and visual cues during flight have been the subject of many studies and could be considered in the context of the DNg02s [6, 19]. Furthermore, haltere control muscle activity is modified by vision via descending input [2, 15]; DNg02 neurons are a candidate class for providing this input. Investigations on their downstream connectivity in the haltere neuropil could illuminate this mode of sensory integration.

Finally, population coding has been observed across species as a mechanism for the specification of a motor output [11, 16]. Given the close correlations observed between wingbeat amplitude and DNg02 activity, we posit that DNg02 cells become active at thresholds of motor output. The large number of cells could provide the fine resolution over a large dynamic range necessary to correct for deviations from the desired flight path. The experiments presented here provide a paradigm and a neuronal locus for detailed studies on the dynamics underlying population coding with range fractionation.

5.3 Concluding remarks

Its relatively lightweight control system makes the fruit fly a promising target for interdisciplinary studies focused on the algorithms and neuronal circuitry underlying biological control of locomotion. This thesis presented two efforts to elucidate these control systems through a combination of systems neuroscience and modern engineering techniques. By necessity, studies of motile biological systems involve

integration of methods from diverse fields; embracing interdisciplinarity throughout training, experimentation, and analysis can result in increasingly novel and impactful work across science and engineering.

Bibliography

[1] Seth A. Budick, Michael B. Reiser, and Michael H. Dickinson. The role of visual and mechanosensory cues in structuring forward flight in Drosophila melanogaster. *Journal of Experimental Biology*, 210(23):4092–4103, 2007.

[2] Wai Pang Chan, Frederick Prete, and Michael H. Dickinson. Visual input to the efferent control system of a fly's "gyroscope". *Science*, 280(5361):289–292, 1998.

[3] Román A. Corfas, Tarun Sharma, and Michael H. Dickinson. Diverse food-sensing neurons trigger idiothetic local search in Drosophila. *Current Biology*, 29(10):1660–1668, 2019.

[4] Alysha M. de Souza. *Sparse neural and motor networks underlying control in the Drosophila Flight System*. PhD thesis, California Institute of Technology, 2022.

[5] Michael H. Dickinson and Florian T. Muijres. The aerodynamics and control of free flight manoeuvres in Drosophila. *Philosophical Transactions of the Royal Society B: Biological Sciences*, 371(1704):20150388, 2016.

[6] Brian J. Duistermars and Mark A. Frye. Crossmodal visual input for odor tracking during fly flight. *Current Biology*, 18(4):270–275, 2008.

[7] Mark A. Frye. Multisensory systems integration for high-performance motor control in flies. *Current Opinion in Neurobiology*, 20(3):347–352, 2010.

[8] Sawyer Buckminster Fuller, Andrew D. Straw, Martin Y. Peek, Richard M. Murray, and Michael H. Dickinson. Flying Drosophila stabilize their vision-based velocity controller by sensing wind with their antennae. *Proceedings of the National Academy of Sciences*, 111(13):E1182–E1191, 2014.

[9] Armin J. Hinterwirth and Thomas L. Daniel. Antennae in the hawkmoth Manduca sexta (Lepidoptera, Sphingidae) mediate abdominal flexion in response to mechanical stimuli. *Journal of Comparative Physiology A*, 196:947–956, 2010.

[10] Irene S. Kim and Michael H. Dickinson. Idiothetic path integration in the fruit fly Drosophila melanogaster. *Current Biology*, 27(15):2227–2238, 2017.

[11] Rafael Levi and Jeffrey M. Camhi. Population vector coding by the giant interneurons of the cockroach. *Journal of Neuroscience*, 20(10):3822–3829, 2000.

[12] Jenny Lu, Amir H. Behbahani, Lydia Hamburg, Elena A. Westeinde, Paul M. Dawson, Cheng Lyu, Gaby Maimon, Michael H. Dickinson, Shaul Druckmann, and Rachel I. Wilson. Transforming representations of movement from body-to-world-centric space. *Nature*, 601(7891):98–104, 2022.

[13] Shigehiro Namiki, Ivo G. Ros, Carmen Morrow, William J. Rowell, Gwyneth M. Card, Wyatt Korff, and Michael H. Dickinson. A population of descending neurons that regulates the flight motor of Drosophila. *Current Biology*, 32(5):1189–1196, 2022.

[14] Bettina Schnell, Peter T. Weir, Eatai Roth, Adrienne L. Fairhall, and Michael H. Dickinson. Cellular mechanisms for integral feedback in visually guided behavior. *Proceedings of the National Academy of Sciences*, 111(15):5700–5705, 2014.

[15] Alana Sherman and Michael H. Dickinson. Summation of visual and mechanosensory feedback in Drosophila flight control. *Journal of Experimental Biology*, 207(1):133–142, 2004.

[16] Tateo Shimozawa and Masamichi Kanou. The aerodynamics and sensory physiology of range fractionation in the cereal filiform sensilla of the cricket Gryllus bimaculatus. *Journal of Comparative Physiology A*, 155:495–505, 1984.

[17] Gavin J. Taylor, Tien Luu, David Ball, and Mandyam V. Srinivasan. Vision and air flow combine to streamline flying honeybees. *Scientific Reports*, 3(1): 1–11, 2013.

[18] Floris Van Breugel, Jeff Riffell, Adrienne Fairhall, and Michael H. Dickinson. Mosquitoes use vision to associate odor plumes with thermal targets. *Current Biology*, 25(16):2123–2129, 2015.

[19] Sara M. Wasserman, Jacob W. Aptekar, Patrick Lu, Jade Nguyen, Austin L. Wang, Mehmet F. Keles, Anna Grygoruk, David E. Krantz, Camilla Larsen, and Mark A. Frye. Olfactory neuromodulation of motion vision circuitry in Drosophila. *Current Biology*, 25(4):467–472, 2015.

[20] Tanya Wolff, Nirmala A. Iyer, and Gerald M. Rubin. Neuroarchitecture and neuroanatomy of the Drosophila central complex: A gal4-based dissection of protocerebral bridge neurons and circuits. *Journal of Comparative Neurology*, 523(7):997–1037, 2015.